Fast Neutrino Flavor Conversions in Core-Collapse Supernova Simulations

Jakob Christoph Ehring

München 2023

Technische Universität München
TUM School of Natural Sciences

Fast Neutrino Flavor Conversions in Core-Collapse Supernova Simulations

Jakob Christoph Ehring

Vollständiger Abdruck der von der TUM School of Natural Sciences der Technischen Universität München zur Erlangung des akademischen Grades eines

Doktors der Naturwissenschaften (Dr. rer. nat.)

genehmigten Dissertation.

Vorsitz:		Prof. Dr. Lothar Oberauer
Prüfer*innen der Dissertation:	1.	apl. Prof. Dr. Hans-Thomas Janka
	2.	Prof. Dr. Andreas Weiler

Die Dissertation wurde am 19.12.2023 bei der Technischen Universität München eingereicht und durch die TUM School of Natural Sciences am 15.02.2024 angenommen.

Contents

1 Introduction

Astro- and particle physics are a perfect match. New insights and progress in one field have always paved the way for new directions in the other field. It is no longer possible to acquire an exhaustive understanding of either subject without knowing at least the foundations of the other.

The connection between core-collapse supernovae (CCSNe) and neutrinos is a paramount example for this. The seemingly rare appearance and following fading away of stars has fascinated people for ages. A commonly given example for this is the supernova of 1054. In 1934, Baade and Zwicky proposed that ordinary stars could transition to extremely compact objects made of neutrons as an explanation for the new phenomenon that they called Super-Novae, extremely bright transients in the sky [1, 2]. At around the same time, new focus on the documentations of the observation of a historical nova from 1054 made by Arabian, Chinese, and Japanese astronomers allowed to connect it with its nowadays observable remnant, the Crab Nebula (Messier 1) [3]. The detection of a radio source at a compatible location, today known as the Crab Pulsar (PSR B0531+21) [4] was further evidence for Baade and Zwicky's idea. A more detailed mechanism to describe the transition was vividly discussed. In 1966, Colgate and White pointed out that neutrinos could be driving the explosion after a stellar core-collapse [5]. In 1985, Bethe and Wilson laid out a sophisticated mechanism, which today is still the paradigm of a successful CCSN. Namely, following the collapse a shock-wave is launched outwards, stalls at a few 100 km, but can be revived within some 100 ms by neutrino heating [6]. Only two years later during the famous supernova of February 23$^{\text{rd}}$, 1987 about two dozen neutrinos were detected giving experimental evidence for a connection between CCSNe and neutrinos [7–9]. For more information on the early days of supernova research, see [10].

Meanwhile, our knowledge of CCSNe and neutrinos has grown and our understanding of both has much increased since then. Unfortunately, SN1987A remains the only supernova that has blessed us with experimental neutrino data to this day. This leaves experimentalists, theorists, and numerical modelers the sometimes dubious pleasure of an interplay in a rather poorly constrained field. In this interplay, experimentalists are expected to build more and ever bigger detectors that should be always running to not miss the next precious event. Theorists come up with new ideas to probe physics at otherwise inaccessible scales. Numerical modelers are the link between both doing their best to filter the relevant aspects, incorporate them into the anyway already complex virtual laboratory and still provide reasonably reliable scenarios and predictions.

An example of a new development in theoretical particle physics that might play an important role for CCSN are fast neutrino flavor conversions. This thesis sheds light on the role that considerable flavor conversions on short time and length scales have on the

evolution of the inner part of a CCSN within the first second.

1.1 A Particle Physicist's View on Stellar Explosions

CCSNe are a complex phenomenon that is still not fully understood today. In this section, I give an overview on the neutrino-driven mechanism, focusing on those aspects that are of relevance in the context of neutrino flavor conversions. For a more comprehensive discussion I refer to the recent reviews [11–21].

CCSNe occur at the transition of an ordinary massive star (possessing a mass $\gtrsim 8\,\mathrm{M}_\odot$, at birth) to a compact object that can be either a neutron star (NS) or a black hole. The origin of the energy powering this violent process is, as so often in astrophysical processes, gravitational potential energy. More specifically, collapse sets in when the iron core, accumulated over the course of successive burning processes, becomes gravitationally unstable. The infalling material builds up kinetic energy. The collapse proceeds until the central density reaches the nuclear saturation density ($\rho \gtrsim 2.7 \times 10^{14}\,\mathrm{g\,cm^{-3}}$) and repulsive forces abruptly stop the contraction. This moment is called core bounce and usually is taken as the zero-point for time measurements in CCSN; referred to as t_{pb} (post-bounce time). During bounce, sound waves steepen, a shock wave forms, and is launched into the still infalling layers. In the central part, the remaining kinetic energy is transformed into internal energy. This region is called proto-neutron star (PNS) as it will become the NS if the explosion is successful.[1] The outer radius of the PNS is usually defined as the iso-density surface where the angle averaged density has a value of $10^{11}\,\mathrm{g\,cm^{-3}}$.

The shock wave does not posses enough energy to gravitationally unbind the remainder of the star. As matter passes through the shock the entropy increases and heavy nuclei are dissociated into neutrons (n) and protons (p), which consumes about 8.8 MeV per nucleon, reducing the pressure behind the shock. At a radius of about 150 km, the shock stalls and does not move outward in radius anymore. In order to regain energy, a heating process is necessary. A few explosion mechanisms have been proposed, including the magneto-rotational mechanism [22, 23]. But fostered by the detection of neutrinos from supernova 1987A and by increasingly more conclusive simulations, over the past decades it has turned out that neutrinos, indeed, are able to do the job. Most of the observed explosions from CCSN can be explained by the neutrino heating mechanism. Their presence in this context is evident and a natural consequence of the extreme environment. Interacting only via the weak force and with an extremely small but non-zero mass, neutrinos are the most elusive stable particles known, which means that once produced they can escape the environment much more easily than any other particle. In fact, already during the late phases of stellar evolution neutrinos are the dominant channel for energy loss in the core region. After collapse, most of them are produced in the PNS, which cools down over the course of a few seconds. In a successful supernova about 99 % of the gravitational binding energy is released in form of neutrinos and only about 1 % goes into the kinetic energy of the explosion and electromagnetic radiation.

[1] If no explosion can be achieved, this region will further collapse and form a black hole.

Neutrinos are uncharged, light-weighted leptons that only interact via the weak force. The eigenstates of the weak force are paired with the 3 generations of charged leptons to weak iso-spin doublets resulting in 3 generations of (active) neutrinos (ν_e, ν_μ, and ν_τ) and anti-neutrinos ($\bar{\nu}_e$, $\bar{\nu}_\mu$, and $\bar{\nu}_\tau$). But not all neutrinos and anti-neutrinos behave equally. When interacting, they need to be distinguished by their flavor. It dictates the kind of charged lepton that needs to be be involved in charged-current interactions. With matter temperatures (T) inside the PNS of a few 10 MeV, neutrinos are created with a typical energy well below 100 MeV. Scattering to lower energies, outside of the PNS mean energies of the neutrinos are in the range of about 10–20 MeV. At these energies charged leptons are almost exclusively electrons (e) or positrons (e^+) and the neutrino production in charged-current interactions is dominated by ν_e and $\bar{\nu}_e$. Due to a large electron chemical potential and since the neutrino spectrum has a high energy tail going beyond 100 MeV, muons (μ) and anti-muons (μ^+) can be produced, but only in relatively small numbers compared to electrons and positrons. For an assessment of their influence see [24, 25].

The overall picture of a CCSN supernova can be relatively well captured and modeled by pooling the neutrinos and anti-neutrinos associated with the heavy leptons (ν_μ, $\bar{\nu}_\mu$, ν_τ, and $\bar{\nu}_\tau$) as one flavor (ν_x) because they effectively behave identically. These neutrinos can be produced only in neutral-current interactions with nucleon-nucleon bremsstrahlung and electron-positron annihilation being the most important [26]. Electron type neutrinos are predominantly produced in charged-current interactions with the absorption of e and e^+ on p and n, respectively, being most important. Similar considerations apply for the interactions of neutrinos with the stellar medium. Absorption via charged-current interactions is only open to ν_e and $\bar{\nu}_e$ so ν_x interact only in neutral-current scattering reactions. Consequently, the interaction cross-sections of ν_e and $\bar{\nu}_e$ are much higher than those of ν_x. For these reasons ν_e and $\bar{\nu}_e$ on the one hand and ν_x on the other hand have different contributions to the heating of matter behind the stalled shock and to the cooling of the PNS as well as its immediate surroundings.

When produced inside the PNS, neutrinos do not escape without further interactions, which is very different from most other conditions that involve neutrinos. In the dense and hot regions, interactions are frequent for all flavors. As the density (ρ) falls below a few $10^{12}\,\mathrm{g\,cm^{-3}}$, ν_x are the first species to decouple from the medium [26]. Their cross-section is considerably lower than the one of ν_e and $\bar{\nu}_e$ because they do not undergo charged-current interactions. Therefore their contribution to the heating behind the shock is subdominant. For ν_e and $\bar{\nu}_e$ on the other hand, up to the shock radius, the interaction cross-section is still high enough that interactions of neutrinos lead to a significant transfer of energy to the matter.[2] This can be illustrated with the concept of neutrinospheres. They indicate the locations where neutrinos, on average, undergo one more interaction. They reside at the radius where the optical depth $\tau(r) = \int_r^\infty \mathrm{d}r' \rho(r') \kappa_{\mathrm{tot}}(r')$, with r the radius and κ_{tot} the total opacity including absorption and scattering (in units

[2] The absorption on free nucleons (downstream of the shock) is higher than on heavy nuclei (upstream of the shock). So outside of the shock radius the interaction rate becomes negligible in terms of heating.

of $\mathrm{cm}^2\,\mathrm{g}^{-1}$), is unity. For ν_x, the neutrinosphere is located well within the PNS. The neutrinosphere of ν_e and $\bar{\nu}_e$ is located at larger distances, roughly at the edge of the PNS. The thermodynamic properties of the neutrino radiation outside of the neutrinospheres depend on the temperature at the neutrinosphere. Therefore, ν_x are on average more energetic than $\bar{\nu}_e$ which are more energetic than ν_e.[3] Within the neutrinospheres the net effect of the production on the one hand and absorption and interaction of a species of neutrinos on the other hand clearly has a cooling effect. The radially decreasing density leads to diffusion that carries away energy. However, outside of the neutrinosphere is a transition to a net heating. As stated above, the interaction rates of ν_x are so low that the thermodynamic evolution of matter is dominated by the contribution of ν_e and $\bar{\nu}_e$ absorption. The temperatures in the atmosphere of the PNS become so low that the heating by the absorption of high-energy ν_e and $\bar{\nu}_e$ is greater than the cooling by the emission of neutrinos. This is because the temperature goes approximately as $T \propto r^{-1}$ and q^-, the specific cooling rate (in units $\mathrm{MeV\,s^{-1}\,baryon^{-1}}$), depends sensitively on the temperature ($q^- \propto T^6$) and therefore $q^- \propto r^{-6}$. On the other hand, once the neutrinos decouple from the medium the properties of the neutrino radiation remain roughly constant and q^+, the specific heating rate, only decreases with the dilution of the neutrino gas, which means $q^+ \propto r^{-2}$. In particular, it decreases slower than the cooling rate [28]. The radius where neutrino cooling and heating balance each other ($q^- + q^+ = 0$) is called gain radius (r_{gain}). The region between the PNS and r_{gain} is called cooling region and the region between r_{gain} and the position of the shock (r_{shock}) is called gain or heating region.

Both regions are connected via mass accretion onto the PNS. A supernova can be successful if the heating in the heating region is strong enough that the amount of transferred energy is sufficient to lead to an expansion preventing matter from streaming into the cooling region from where it will be accreted onto the PNS. In this case the expansion of the shock radius can be revived; usually within about a second after the bounce. Here, neutrino flavor conversions come into play and could have a pivotal role. Numerical simulations, up to now, have treated the flavor of the neutrinos as an unchanged property during their propagation. High matter densities that cause an alignment of the interaction and propagation eigenstates were good reasons to think that this is a good assumption. However, the picture has changed when it was discovered that the neutrinos themselves can constitute a relevant potential that can cause considerable flavor conversion, as laid out in the following Section 1.2. Changing the neutrino flavor alters the neutrino heating and therefore introduces fundamental changes in the dynamics. Specifically, increasing the number of ν_x in the cooling region at the cost of ν_e and $\bar{\nu}_e$ ($\nu_e, \bar{\nu}_e \rightarrow \nu_x, \nu_x$) will result in more efficient cooling, which accelerates the concurrent contraction of this region. In the gain region this reduces the heating. Accordingly, if the opposite process ($\nu_x, \nu_x \rightarrow \nu_e, \bar{\nu}_e$) takes place, heating in the gain region increases and the contraction of the cooling region will decelerate.

[3] The latter is a result of the dominance of neutrons over protons and to a lower degree also of corrections from weak magnetism in neutral-current interactions [27], which both reduce the opacity for $\bar{\nu}_e$ compared to ν_e. Therefore $\bar{\nu}_e$ decouple further out than ν_e.

Another core aspect of CCSN, which could be altered by flavor conversions, is the production of nucleosynthetic yields [17, 19, 20, 29]. The neutrino radiation does not only determine the dynamical and thermodynamic conditions that lead to the ejection of matter. Via β-like absorption reactions, ν_e and $\bar{\nu}_e$ set the relative abundance of protons to neutrons that is decisive for the amount of elements with a high atomic number being produced. Specifically, the electron fraction (Y_e), i.e. number of electrons per baryon, can be used as an indicator for the production of heavy elements. The so called *r-process* is responsible for the creation of elements with a high atomic number $A \gtrsim 90$ and needs $Y_e < 0.5$. On the other hand, $Y_e > 0.5$ can lead to the production of proton-rich elements in the $\nu\,p$-process [30, 31]. Modern simulations indicate that only in explosions of the lowest mass progenitors[4] the early ejecta feature neutron-rich conditions compatible with a moderate r-process [32]. Conversely most ejecta of CCSN are considered to be proton-rich and only moderately neutron-rich, including the so-called neutrino-driven, late time matter flows originating in the surface of the PNS [33]. Flavor conversions can change the ratio between ν_e and $\bar{\nu}_e$ and therefore are expected to influence the nucleosynthesis of elements in a CCSN.

Furthermore, the neutrino signal of a galactic CCSN can be measured on earth and will be different if neutrino flavor conversions are present. In a world without flavor conversions it would be an unambiguous messenger about the circumstances and conditions in the innermost regions. As will be laid out in Section 1.2, the neutrino flavor undergoes a complex evolution. In order to make full use of neutrinos as messengers, the effects of flavor evolution during propagation need to be disentangled from the effects stemming from interaction with matter. Only then can features in the signal be either attributed to (intrinsic) flavor evolution or be used to gain insight into the conditions of ordinary matter inside a supernova.

Before proceeding to a description of the processes that could allow for flavor conversions, I drop a few remarks on other aspects that are of relevance in this thesis. The success of a supernova can also be altered by changing the effectiveness of the heating or cooling. Eventually, the shock needs to be strong enough to overcome the ram pressure of the infalling material. The latter decreases over time because of the decreasing density profile of the progenitor system. This is why, very broadly speaking, progenitors with lower initial masses, which tend to have a steeper density profile, produce explosions more easily than systems from a more heavy progenitor.[5]

Sudden changes in the mass accretion rate are a consequence of a strong density contrast at the interface between stellar shells of different compositions. The shock wave reacts to those with a similarly sudden expansion. This increases the volume of and mass in the gain layer and therefore the total heating rate. It can trigger the onset of explosions [35]. However, the discontinuities are a numerical effect and a consequence of the initial conditions that are usually obtained directly from stellar evolution, which is constrained to spherical symmetry. Lifting this approximation in the progenitor systems

[4] termed electron-capture supernovae

[5] Keep in mind though that this is not a monotonic relation. The density profile can be heavily influenced by the evolution history, for example the existence of shell mergers [34].

reduces the change in ram pressure and introduces more realistic asymmetries. See for example [36, 37].

A contraction of the PNS and the surrounding layers appears to work against a successful explosion because it creates a pull on the gain region. However, the gravitational compression also results in an increase of the temperatures in the region of the neutrinospheres, which raises the neutrino energy. Interestingly, taking into account the effects of muons has just such an effect. It turns out this can facilitate a successful explosion in the long run [24].

Finally, a word about the numerical modeling of CCSNe is in order. Due to the lack of experimental data from the center of a CCSN, radiation hydro-dynamical numerical simulations remain the most reliable source of information. Despite great advances in the available computational tools and resources, simulations that do not impose any spatial symmetries (3D) are not yet the norm. A growing number of such simulations is available [36–44] but using 3D simulations in an explorative study, such as the one conducted in this thesis, is not a well balanced approach. Spherically symmetric (1D) simulations are computationally the cheapest option. Even without a dedicated high performance computing system, simulating 1 s of a CCSN can be done within a day of computation time. But the restriction to 1D comes at a price. As soon as hydrodynamic instabilities develop ($t_{\mathrm{pb}} \gtrsim 5\,\mathrm{ms}$) a 1D treatment fails to capture essential processes. Large-scale multi-dimensional flows have proven to be an indispensable element in CCSNe. Non-radial motions, most notably the standing shock accretion instability (SASI) and convection in the region between the PNS and the stalled shock, facilitate explosions by pushing the shock further outwards and increasing the time matter stays in the gain region [45, 46]. Also within a layer inside the PNS a hydrodynamically unstable stratification develops that leads to convective motions. The convective transport of energy and lepton number is more efficient than the respective transport as a result of the diffusion of radiation. Both phenomena are present in axially symmetric (2D) simulations. But still, motions are only allowed in toroidal structures and the fragmentation to smaller scales is suppressed. Especially the inverse cascade of kinetic energy to large-scale motions [47] and artifacts from the axis of symmetry promote explosions in unrealistic processes [48]. On a small sized high performance system, 2D simulations can be done in a matter of days. Still, 2D simulations feature an essential set of effects and are well suitable to conduct first-of-a-kind simulation studies exploring new physics.

1.2 An Astronomer's View on Neutrino Flavor Conversion

Flavor changes of propagating neutrinos have tricked, puzzled and challenged scientists since they started to consider neutrinos as messengers. In this section, I give an overview on today's understanding of the evolution of the neutrino flavor in a collapsing star, focusing on the inner part where the coherent forward scattering of neutrinos on themselves modifies the flavor evolution without flavor changing point-like interactions. For a more comprehensive discussion, I refer to the recent reviews [49–56].

Neutrinos posses the remarkable property that the eigenstates of the weak force (flavor

eigenstates) do not align with the eigenstates of propagation (mass eigenstates). As a consequence, even in the most simple example of vacuum propagation, the neutrino flavor content is not a conserved quantity. Oscillatory patterns develop that depend on fundamental neutrino properties (masses and mixing angles) and on the specific properties of the neutrino beam (energy, distance traveled) [57].

The flavor changing characteristics are modified in the presence of quantum mechanical potentials. Most well known is the potential that arises from coherent forward scattering on electrons in ordinary matter, the so called Mikheyev, Smirnov, Wolfenstein (MSW) effect [58, 59]. The consequence of the asymmetry between the electron and positron densities is that the cross-section for coherent forward scattering of ν_e is larger than for all other flavors. This is because ν_e also interact via charged-current interactions ($\nu_e(q) + e(k) \rightarrow e(q) + \nu_e(k)$, with q and k denoting 4-momenta). The neutral-current channel for electron scattering ($\nu_\alpha(q) + e(k) \rightarrow \nu_\alpha(q) + e(k)$, with ν_α being a neutrino of arbitrary flavor) is open to all flavors of neutrinos.[6] The strength of the potential is proportional to the net electron density.

The most prominent example is the solution to the solar neutrino problem, explaining why the solar ν_e flux measured on earth is approximately only a third of what is predicted from their production in nuclear fusion reactions and solar properties [60, 61]. The still comparably low matter densities inside the solar core are already high enough so that the effective mixing angle is almost maximal; meaning that the ν_e weak flavor and second propagation mass eigenstate practically overlap. As the density adiabatically decreases in radial direction, the neutrinos remain in the mass eigenstate and pass a resonance where the mixing becomes maximal. Arriving at earth, the vacuum mixing angle gives the survival probability yielding the flux measured at earth. As neutrinos pass the outer layers of a collapsing star—after they have already completely decoupled from the medium—they may actually pass two resonance regions [62]. Like in the case of solar neutrinos, adiabaticity holds except for after a few seconds when the passing of the shock and/or the reverse shock in the resonance region causes non-adiabatic matter profiles. In a neutrino observation of the next galactic supernova this will help to determine the neutrino mass ordering [63]. However, the flavor changes do not have a dynamical impact on the CCSN anymore.

Not only electrons can generate a relevant potential. In 1992 Pantaleone, pointed out that neutrino-neutrino forward scattering can similarly lead to flavor changing effects because it is also flavor dependent [64]. The key difference to MSW-like phenomena is that the arising potential can develop non-vanishing off-diagonal terms, i.e. terms that if subject to an instability lead to large flavor coherence and therefore mixing. A year later, Sigl and Raffelt presented a unified description of the neutrino flavor evolution in the presence of interactions with matter, vacuum oscillations, a matter potential, and such self-interactions [65]. The resulting equation, making use of the mean field approximation, is nowadays known as quantum-kinetic equation (QKE) and the basis

[6] Coherent forward scattering also happens with neutrons and protons but for them the contribution is identical for all neutrino flavors and is therefore irrelevant for the flavor evolution.

of most studies on flavor conversions originating in neutrino self-interactions,

$$(\partial_t + \boldsymbol{v} \cdot \boldsymbol{\nabla}_{\boldsymbol{x}})\ \rho = \mathcal{C}[f] - i[H_{\mathrm{vac}}, \rho] - i[H_{\mathrm{MSW}}, \rho] - i[H_{\nu\nu}, \rho]. \tag{1.1}$$

Here, $\boldsymbol{v}$ is the neutrino velocity and ρ is the density matrix of the neutrino field.[7] It contains the usual occupation numbers on the diagonals and the coherence between the flavors on the off-diagonals. $\mathcal{C}[f]$ is the collisional term containing reactions that are second order in G_{F}, Fermi's constant, like the production, absorption, and pair-annihilation of neutrinos and momentum transferring scattering reactions. The terms containing commutators of a Hamiltonian and ρ are first order in G_{F} and describe the effects of neutrino propagation in a potential. The vacuum Hamiltonian H_{vac} describes the mixing of the eigenstates of weak interaction and propagation in vacuum. H_{MSW} contains the potential from the MSW effect. $H_{\nu\nu}$ contains the contribution from the coherent neutrino-neutrino forward scattering on themselves, which often is called a self-interaction term.

The reactions generating the potential of $H_{\nu\nu}$ are interactions of coherent forward scattering. They do not involve momentum exchange but add a phase. The strength of $H_{\nu\nu}$ depends on the particle density of the generating medium that is the number density of the neutrinos itself,

$$H_{\nu\nu} = \sqrt{2} G_{\mathrm{F}} \int \mathrm{d}\boldsymbol{p}'\ (1 - \boldsymbol{p} \cdot \boldsymbol{p}')[\rho(\boldsymbol{p}) - \bar{\rho}(\boldsymbol{p})], \tag{1.2}$$

where $\boldsymbol{p}$ is the 3-momentum and ρ ($\bar{\rho}$) is the density matrix of the (anti-)neutrinos.

Large-scale (a few thousands of km) numerical simulations of the temporal evolution of CCSNe focus on the contribution of the collisional term and assume that the influence of the Hamiltonians in Equation (1.1) is small. In the absence of $H_{\nu\nu}$, this can be justified because there are two spatially separated regions. In the high-density core of the CCSN neutrinos have an influence on the kinetic evolution (where the contribution of $\mathcal{C}[f]$ is important) and in the outer region flavor conversions happen because of matter effects (where the contribution of H_{vac} and H_{MSW} is important). In this case, for the inner regions, the density matrix approach is no longer needed and the equation simplifies to classical Boltzmann equations. On the other hand, the distant properties of the neutrino radiation can be calculated in detail in post-processing, essentially solving a propagation problem. But as our knowledge about the effects arising from $H_{\nu\nu}$ increased, it has been realized that flavor conversions should be expected to happen in the dynamically relevant regions as I will summarize below.

Before presenting some results on the effects of $H_{\nu\nu}$ a few remarks on properties that can be drawn from its definition are helpful. The dependence on the density matrix makes the problem non-linear and creates off-diagonal potentials. But also by other means it is rather cumbersome to solve. It is an inherently 7-dimensional problem (each 3 dimensions in real and momentum space plus 1 temporal dimension). The integral over neutrino momentum space couples the evolution of neutrinos that travel along entirely

[7] Note that in the other contexts of this thesis ρ denotes the matter density. In this chapter I refer to the density matrix for consistency with the literature.

different paths. Furthermore, it has turned out that non-trivial flavor evolution can happen on scales that are much smaller than the resolution in numerical simulations of CCSNe. Therefore, it is not possible in the near future to solve the equations self-consistently in a straightforward way by numerically integrating the density matrix in time.

With a rather complicated and twisted discovery history, today the effects stemming from $H_{\nu\nu}$ can be divided in two categories of flavor conversion phenomena. They are based on the dominant scales and the asymmetries driving the flavor evolution.

The type, which was discovered first, is nowadays known as *slow modes*. A linear stability analysis reveals that there are flavor instabilities if there is a zero crossing in the *energy* dependence of the lepton number [66–68]. Interpreting anti-neutrinos as particles with negative energy and working in a two flavor scenario the lepton number is defined as

$$g(E,\theta) = \begin{cases} f_{\nu_e}(E,\theta) - f_{\nu_\mu}(E,\theta) & \text{for } E > 0 \\ f_{\bar{\nu}_\mu}(E,\theta) - f_{\bar{\nu}_e}(E,\theta) & \text{for } E < 0, \end{cases} \tag{1.3}$$

with f_{ν_α} the distribution function of a neutrino of flavor α, E the energy, and θ the azimuthal angle relative to the outward pointing direction. In the supernova case where both ν_e and $\bar{\nu}_e$ are present and the densities of the heavy lepton neutrinos and anti-neutrinos are sufficiently similar, a zero crossing at $E = 0$ is guaranteed and therefore, so are slow modes. This being said, the presence of an instability does not guarantee significant flavor conversion because an exponential growth in the linear regime does not need to hold in the non-linear regime. Flavor instabilities arising from energy crossings have a growth rate whose scale is set by the vacuum oscillation frequency $\omega = \Delta m^2/E$, with Δm^2 the difference of the squared masses of the mass eigenstates and E the neutrino energy [69]. In the CCSN case, with 15 MeV being a representative value of the neutrino energy, the scale is $\mathcal{O}(1\,\mathrm{km}^{-1})$. Naturally, the first investigated scenarios looked at simplified problems making assumptions like homogeneity, isotropy, or symmetries to make the equations tractable [70–72]. Though they claimed significant flavor conversions, later it was found that relaxing symmetry assumptions can suppress conversions, because neutrinos traveling along different paths experience different histories (multi-angle or matter suppression) [73–77].

A large-scale simulation also incorporating flavor conversions according to the stationary bulb model [71] was recently conducted [78]. They coupled a 1D radiation-hydrodynamics code with a code that calculates survival properties of neutrino flavors but found little influence in the post shock region. However, this might be a result of not capturing all effects of slow modes. Especially temporal instabilities [79] do not seem to be taken into account. Temporal instabilities are not subject to multi-angle suppression because they do not involve different trajectories, so the results of [78] do not capture all effects.

This leaves the discussion with the question on how the neutrino spectrum changes in the presence of slow modes. A robust feature of slow modes in spherical symmetry is the phenomenon of spectral swaps. They describe that at a given energy the flavor content of ν_e and ν_μ, or $\bar{\nu}_e$ and $\bar{\nu}_\mu$ swaps. This results in discontinuities in the energy spectrum,

called spectral splits. Depending on the details even multiple swaps can occur [67].

Research interest on slow modes came to a sudden decrease when the community realized the potential of another category of conversions nowadays known under the name of *fast modes* or fast flavor conversions (FFC). Their possible occurrence was first pointed out already in 2005 by Raymond Sawyer but initially received no recognition [66, 80]. Only about 10 years later when he considered a (more realistic) case of neutrinospheres with flavor dependent radii, which naturally leads to a non-trivial angular distribution, their potential was realized [81]. In this section I restrict myself to the two-flavor case with the additional assumption of $f_{\nu_x} = f_{\bar{\nu}_x}$, but this can also be generalized for the three flavor case [82–84]. FFC are triggered by *angular* crossings in the (energy integrated) electron lepton number (ELN)

$$G(\theta) = \sqrt{2} G_F \int_0^\infty \frac{E^2 \mathrm{d}E}{(2\pi)^3} (f_{\nu_e}(E,\theta) - f_{\bar{\nu}_e}(E,\theta)). \tag{1.4}$$

Note that here anti-neutrinos have a positive energy. In fact, there is mathematical proof that the instability is solely connected to crossings in the ELN [85].

For fast instabilities the characteristic time scale is set by the strength of the potential $\mu = \sqrt{2} G_\mathrm{F}(n_\nu + n_{\bar{\nu}})$, with n_ν ($n_{\bar{\nu}}$) the number density of the (anti-)neutrinos, and can be as small as $\mathcal{O}(1\,\mathrm{cm}^{-1})$. It is independent of the vacuum frequency ω [69], but note that in the non-linear regime a dependence on the energy was found [86]. Also taking into account the effects of collisions, which are inherently energy dependent, might introduce an energy dependence, too [87]. Instabilities can exist even without flavor mixing, which is an intriguing property from a theorist's perspective[8] [88].

With the claim of flavor instabilities in the decoupling region, where neutrinos do have an influence on the dynamical evolution, the search for unstable regions began. As in the case of slow modes, linear stability analysis can be used for this. A dispersion relation approach can be used to gain insight on further properties of the instability (temporal vs. spatial) [89]. However, in order to just find unstable regions looking for ELN crossings is sufficient. In simulations using a full Boltzmann transport scheme, where the angular distribution is available, this can be done directly. Simulations utilizing a reduced set of angular moments (as explained in Section 2.1) cannot provide direct information and the angular distribution needs to be reconstructed [90–94]. Crossings could exist in all regions of interest where neutrinos have an influence on the dynamical evolution of a CCSN [95]. This includes the convective layer of the PNS [96–98], the decoupling region [99–101], as well as the pre- and postshock region [84, 102]. A very recent development is the evolution of machine learning techniques to accelerate the searches for crossings and to make them available on the fly in large scale numerical simulations [**Abbar2023˙3**, 103].

Concerning the outcome of flavor conversions, the existence of ELN crossings does not guarantee significant flavor changes. So a number of studies investigate different scenarios with reduced complexity like homogeneity, isotropy, or reduced dimensionality

[8] Though from a practical point of view this is not strictly needed, given that flavor mixing is mostly agreed on.

to get information on what can be expected as a final state of flavor conversions. But so far there is no agreement on which assumptions can be used without simplifying the equations too much.

Many groups consider a small box with periodic boundary conditions arguing that this is a reasonable simplification if the growth rate is sufficiently large [104–109]. A recent comparison study found an adequate agreement on the asymptotic state calculated by the different codes, when applied to the same initial conditions [110]. These simulations can be done very efficiently allowing a sampling of a variety of initial angular distributions [111].

In a more complex setting the effect of collisions (scatterings) can be studied. They can create favorable conditions for conversions without damping them [112]. Others found a damping on larger scales because collisions flatten the angular distributions [113]. The authors of [114] on the other hand find an enhancement of flavor conversion that they attribute to collisions, arguing that collisions can mix the neutrinos within the angular distribution. Using a Monte Carlo approach and also including emission and absorption effects the authors of [115] find higher conversion rates compared to scenarios without the effects of collisions.

Studies additionally taking into account advection, in which the transport of neutrinos leads to a solution that is not constant in time, suggest that small scale simulations are not sufficient to tackle the problem [116, 117]. Though still on the level of a toy model and static background, they find that effects of advection increase the relevant scales and inhibit the emergence of small scale structures. They also emphasize that in their approach they see the emergence of slow modes that interplay with fast modes calling for a more holistic treatment.

Another recent proposal to achieve a description for the final state of flavor conversions suggests that it is sufficient to take into account conservation laws and demand that the final state is free of crossings in the angular distribution. They also stress that one has to take into account different angular distributions in the heavy lepton neutrino sector, termed XLN [118]. In addition this has been extended to situations where a Dirichlet boundary condition applies [119].

Some studies try to find a way to solve the QKE on large scales by rescaling oscillation lengths by effectively reducing the number of neutrinos [120]. On a stationary background taken from a large-scale simulation of a supernova they find reduced post-shock neutrino heating [**Nagakura2023˙3**, 121]. Without temporal dependence it unfortunately remains unclear how the supernova reacts to these changes that is if these effects are persistent.

This work does not account for any effect of the recently unearthed phenomenon of collision induced flavor conversions [122–127]. These involve further complications in this context and are beyond the scope of this thesis.

Concluding this section, the in-depth understanding of self-induced flavor conversions has not yet converged. Therefore a self-consistent integration in large scale simulations is currently a futile endeavor (see also [128]). Progress in understanding the ramifications of instabilities surely comes from a better modeling of the detailed processes, but a complementary approach is needed to advance in the broader context of CCSN, which

is the purpose of this thesis.

1.3 Outline of this Thesis

The aim of this thesis is to study the effects of neutrino flavor conversions on the evolution of CCSNe using state-of-the-art, large-scale, neutrino-hydrodynamical numerical simulations. Similar studies have been done before but only in the context of a system consisting of a black hole and an accretion disk, which are formed in binary neutron star mergers. The conditions, which neutrinos experience in these systems are similar to the conditions CCSNe. The studies found that flavor conversions accelerate the cooling of the disc and modify generation of chemical elements in the matter ejected by the evolving disc [129, 130]. Therefore, flavor conversions are expected to also influence the dynamical evolution and nucleosynthesis in supernovae. Specifically, this thesis addresses the important question of how the predictions of numerical simulations of CCSNe change when flavor conversions are taken into account. How do they alter the dynamical evolution of supernovae? What is their influence on the emitted neutrino signal? Does the inclusion of flavor conversions give rise to other effects that could lead to measurable signatures?

I present results from simulations that for the first time incorporate an effective treatment of neutrino flavor conversions. This newly implemented scheme features the pairwise conversion of neutrinos and anti-neutrinos from one flavor to another. Depending on the local flavor distribution, pairs of electron neutrinos and anti-neutrinos are converted to pairs of heavy lepton neutrinos and anti-neutrinos ($\nu_e, \bar{\nu}_e \rightarrow \nu_x, \nu_x$) or the other way round ($\nu_x, \nu_x \rightarrow \nu_e, \bar{\nu}_e$). No generally accepted quantum physical solution will be available in the near future and predictions on a final outcome of flavor conversion effects are limited to special cases. Therfore, this study employs an effective, parameterized treatment, which is vital, because simulations that resolve neutrino propagation to the smallest scale necessary for self-consistency have not converged to a final understanding yet. The strongest constraints for the amount of flavor conversion are set by conservation laws. Because flavor conversions are a phenomenon of coherent forward scattering, an effective treatment must conserve energy, momentum, and lepton number. The employed scheme is constructed such that the final state of flavor conversions maximizes the mixing under these constraints. It is applied instantly on a cell-by-cell basis, and thereby accounts for the fact that flavor conversions take place on spatial and temporal scales orders of magnitude below the numerical discretization of state-of-the-art CCSN simulations. This simple flavor conversion scheme is supplemented by a parameterized criterion for the appearance of flavor conversions. A straightforward density criterion restricts flavor conversions to the regions where matter falls below a critical threshold density. This allows me to pin down emerging effects to the presence of flavor conversions in specific regions of the supernova. The approach of this study does not rely on details of any underlying scenario of flavor conversions. It is valid for every kind of flavor mixing that happen on scales smaller than the numerical resolution and conserve the quantities mentioned above.

Using this novel approach, I compare the consequences of flavor conversions in 1D and 2D simulations and study multiple systems initialized with progenitors of different masses. The study focuses on the accretion phase, which starts after bounce and lasts until either the explosion sets in or the collapse to a black hole is inevitable. The simulations cover the effects of flavor conversions up to roughly the shock radius and therefore, all regions where an accurate treatment of neutrino heating and cooling is crucial. The feedback effects between neutrinos on the one hand and hydrodynamic flows of matter on the other hand are included self-consistently.

Comparing the results of simulations with flavor conversions to simulations without flavor conversions, I infer a range of outcomes of CCSNe that is likely to include also the impact of a more realistic scenario of flavor conversions. This, for the first time, enables an assessment of the maximum impact of flavor conversions in different regions of the supernova.

In Chapter 2, I give an overview of the numerical code used in the generation of data for this thesis. I describe how I extended the code with an effective, parameterized treatment of flavor conversions constrained only by conservation laws in order to explore the maximum effect of flavor conversions. Additionally, I provide test cases to validate the correct implementation. Chapter 3 contains a presentation of the data from the simulations in 1D and 2D. Most aspects of how flavor equilibrated neutrinos influence the dynamical evolution on smaller scales can already be seen in simulations performed in 1D. More realistic predictions of the dynamical evolution are obtained from the simulations in 2D, which allow for non-radial motion of matter. In Chapter 4, I give a short summary of the findings of this thesis. Finally, in Chapter 5, I conclude, put the results into context with other developments, and give suggestions for future work.

2 Numerical Simulations of Core-Collapse Supernovae with the ALCAR Code

In this chapter I introduce the ALCAR code [131] that I used to perform the numerical calculations. It has been developed by Martin Obergaulinger and Oliver Just, and largely modified by Robert Glas. I extended the code with a module implementing a parametric scheme of fast flavor conversions.

In Section 2.1, I give a higher-level description over the evolved equations and their implementation. For a more detailed description I refer to the dedicated literature [131–135]. In Section 2.2, I describe the implementation of the new module for neutrino flavor conversions in the ALCAR code and a few tests. The description of the implementation has already been published in [136] and a similar implementation was used in [129].

2.1 Overview of the ALCAR Code

I used the ALCAR code to perform the simulations analyzed in this thesis. It combines the AENUS module[1] for (magneto-)hydrodynamics with the ALCAR module[2] for neutrino radiation transport. In the following ALCAR always refers to the combined code unless stated otherwise. I stick closely to the notation of [134].

In the absence of magnetic fields and viscosity, the evolution of ordinary stellar matter can be described by the Euler equations, which derive from the conservation equations of mass, momentum, and energy,

$$\partial_t \rho + \nabla_j(\rho v^j) = 0 \tag{2.1a}$$

$$\partial_t(\rho Y_\mathrm{e}) + \nabla_j(\rho Y_\mathrm{e} v^j) = Q_\mathrm{N} \tag{2.1b}$$

$$\partial_t(\rho v^i) + \nabla_j(\rho v^i v^j + P_\mathrm{gas}) = -\rho\nabla^i\Phi + Q^i_\mathrm{M} \tag{2.1c}$$

$$\partial_t e_\mathrm{tot} + \nabla_j(v^j(e_\mathrm{tot} + P_\mathrm{gas})) = -\rho v_j\nabla^j\Phi + Q_\mathrm{E} + v_j Q^j_\mathrm{M}. \tag{2.1d}$$

Here, Einstein summation convention is implied and t and i, j denote temporal and spatial dimensions, respectively. ρ denotes the baryonic density, v^j is the j-th component of the fluid velocity, Y_e is the electron fraction (that is the number density of protons divided by the number density of baryons)[3], P_gas is the gas pressure, and e_tot is the total energy (that is the kinetic plus internal energy). The terms on the right hand side of Equations 2.1 are the source terms. They contain the gravitational potential Φ, and

[1] AENUS is named after the river *Inn* in its Latin version.
[2] ALCAR is an acronym for "**A**lgebraic **L**ocal **C**losure **A**pproach for **R**adiation
[3] ALCAR assumes that no (anti-)muons are created, but see [24, 25]

terms related to neutrino interactions: the source term for the electron fraction Q_{N}, the source term for momentum in i-th direction Q^i_{M}, and the source term for internal energy Q_{E}.

ALCAR solves these equations for the independent variables ρ, ρY_{e}, ρv^i, and e_{tot}. P_{gas} can be obtained from a microphysical equation of state (EoS) from the thermodynamical variables ρ, Y_{e} and e_{tot}. The simulations presented in this thesis employ the "SFHo" EoS of [137]. The gravitational potential is calculated in Newtonian gravity by solving Poisson's equation with a multipole expansion and corrected for effects of general relativity using case A of [138].

ALCAR uses a two moment scheme to evolve the neutrino radiation field in time. This means that the radiation field is described by a truncated series of the in principle linearly independent angular moments of the distribution function $\mathcal{F}(\boldsymbol{x}, \boldsymbol{p}, t)$.

Following [139] let

$$\mathrm{d}N(\boldsymbol{x}, \boldsymbol{p}, t) = \frac{g}{h^3}\,\mathcal{F}(\boldsymbol{x}, \boldsymbol{p}, t)\mathrm{d}x^3\mathrm{d}p^3 \tag{2.2}$$

denote the number of neutrinos in a phase space volume $\mathrm{d}x^3\mathrm{d}p^3$ with g the statistical weight, h Planck's constant, and

$$\mathcal{I}(\boldsymbol{x}, \epsilon, \boldsymbol{n}, t) = g\left(\frac{\epsilon}{hc}\right)^3 c\mathcal{F}(\boldsymbol{x}, \boldsymbol{p}, t) \tag{2.3}$$

denote the specific intensity with c the speed of light and $\epsilon = |\boldsymbol{p}|c$ the energy of a neutrino with momentum $\boldsymbol{p}$ in direction of the unit vector $\boldsymbol{n}$.

The angular moments are obtained by integrating the distribution function over the angular momentum space,

$$E = \frac{1}{c}\int \mathrm{d}\Omega_n \mathcal{I}, \tag{2.4a}$$

$$F^i = \int \mathrm{d}\Omega_n \mathcal{I}\, n^i, \tag{2.4b}$$

$$P^{ij} = \int \mathrm{d}\Omega_n \mathcal{I}\, n^i n^j, \tag{2.4c}$$

$$Q^{ijk} = \int \mathrm{d}\Omega_n \mathcal{I}\, n^i n^j n^k, \tag{2.4d}$$

$$\vdots$$

with the solid angle element in momentum space $\mathrm{d}\Omega_n$. ALCAR evolves the 0th-order angular moment E—the energy specific neutrino energy density—and the 1-st-order angular moment $\mathbf{F}$—the energy specific neutrino energy flux density—(with F^i the i-th component). $\mathbf{P}$, the 2nd-order angular moment pressure tensor (with P^{ij} the ij-th component), and $\mathbf{Q}$, the 3rd-order angular moment (with Q^{ijk} the ijk-th component) are not evolved but appear in the equations for the lower order moments.

Following [140, Section 3] the governing Boltzmann equation for the neutrinos reads

$$\frac{1}{c}\partial_t \mathcal{I} + n^i \nabla_i \mathcal{I} = [\mathcal{I}]_{\mathrm{coll}} \tag{2.5}$$

with $[\mathcal{I}]_{\text{coll}}$ the collisional integral describing the interactions with ordinary matter. To exploit symmetries of the neutrino matter interactions, the coordinate system in momentum space is fixed to the co-moving frame where matter is at rest. The governing equation for E and F^i are obtained analogously to Equations (2.4a) and (2.4b) by integration (applying $\int \mathrm{d}\Omega_n$ and $\int \mathrm{d}\Omega_n\, n^i$, respectively to Equation (2.5)). Finally, ALCAR takes into account general relativistic effects of redshift and time dilation. The following equations are effectively accurate to order $\mathcal{O}(v/c)^2$:

$$\partial_t E + \nabla_j(\alpha F^j + v^j E) + P^{ij}\nabla_i v_j + F^i \nabla_i \alpha - \partial_\epsilon[\epsilon(P^{ij}\nabla_i v_j + F^i \nabla_i \alpha)] = \alpha S^{(0)} \tag{2.6a}$$

$$\partial_t F^i + \nabla_j(\alpha c^2 P^{ij} + v^j F^i) + F^j \nabla_j v_i + c^2 E \nabla^i \alpha - \partial_\epsilon[\epsilon(Q^{ijk}\nabla_j v_k + c^2 P^{ij}\nabla_j \alpha)] = \alpha S^{(1)} \tag{2.6b}$$

Here α is the lapse function (calculated as in [141], Section 3.7.2). The source terms $S^{(0)}$ and $S^{(1)}$ are, respectively, the 0th- and 1st-order angular moments of the collision integral.

As mentioned before, P^{ij} and Q^{ijk} are not evolved quantities but computed from a closure relation which depends on the lower order moments E and F^i. ALCAR uses a so-called *Algebraic Eddington Factor* method (AEF) meaning that the higher moments can be expressed as functions of the lower moments. Assuming that the second and third moments are isotropic tensor functions [142] and following [143] the second moment can be expressed as a linear combination of a tensor proportional to the Kronecker delta δ^{ij} and a tensor proportional to $n_F^i n_F^j$ with n_F^i the normalized flux direction $n_F^i = \frac{F^i}{|\mathbf{F}|}$.

$$P^{ij} = E\left(\frac{1-\chi}{2}\delta^{ij} + \frac{3\chi - 1}{2} n_F^i n_F^j\right), \tag{2.7}$$

with $\chi = \chi(f)$ an algebraic function depending only on the flux factor $f = \frac{|\mathbf{F}|}{cE}$. The third moment reads

$$Q^{ijk} = cE\left[\frac{f-q}{2}(n_F^i\delta^{jk} + n_F^j\delta^{ik} + n_F^k\delta^{ij}) + \frac{5q-3f}{2} n_F^i n_F^j n_F^k\right], \tag{2.8}$$

with $q = q(f)$ another function depending only on the flux factor. The Minerbo closure, used in ALCAR, is obtained from assuming that neutrinos follow a fermionic particle distribution in a state of maximum entropy [144].

$$\chi_{\text{Minerbo}}(f) = \frac{1}{3} + \frac{1}{15}(6f^2 - 2f^3 + 6f^4) \tag{2.9a}$$

$$q_{\text{Minerbo}}(f) = \frac{f}{75}(45 + 10f - 12f^2 - 12f^3 + 38f^4 - 12f^5 + 18f^6) \tag{2.9b}$$

The source terms of the neutrino radiation and the hydrodynamics (in Equations 2.1

and 2.6, respectively) are related as follows:

$$Q_{\mathrm{N}} = -\alpha m_{\mathrm{B}} \int_0^\infty \left(S_{\nu_e}^{(0)} - S_{\bar{\nu}_e}^{(0)} \right) \frac{\mathrm{d}\epsilon}{\epsilon}, \tag{2.10a}$$

$$Q_{\mathrm{M}}^i = -\frac{\alpha}{c^2} \sum_\nu \int_0^\infty S_\nu^{(1),i} \mathrm{d}\epsilon, \tag{2.10b}$$

$$Q_{\mathrm{E}} = -\alpha \sum_\nu \int_0^\infty S_\nu^{(0)} \mathrm{d}\epsilon, \tag{2.10c}$$

where m_{B} is the baryon mass, $S_{\nu_e}^{(0)}$ and $S_{\bar{\nu}_e}^{(0)}$ are the source terms of ν_e and $\bar{\nu}_e$, respectively, and the sum $\sum_\nu$ runs over all neutrino species.

ALCAR solves the radiation transport equation for three species of neutrinos. Electron neutrinos (ν_e) and electron anti-neutrinos ($\bar{\nu}_e$) are treated separately. All other types of neutrinos are pooled into a single species (ν_x) to optimize the computational load. This approximation is justified because the typical temperatures in a supernova environment (a few 10s of MeV) are not high enough to produce a crucial amount of muons (having a rest mass of about 106 MeV) not to speak of tauons (having a rest mass of about 1777 MeV). Therefore the contribution of charged current interactions of muon neutrinos (ν_μ) and tauon neutrinos (ν_τ) and their respective antiparticles is subdominant (but see [24, 25]). This also means that ALCAR does not take into account the difference of the behavior of neutrinos and anti-neutrinos in the heavy lepton neutrino sector because again the contribution is subdominant.

To compute the source terms in Equations 2.9 ALCAR includes the reactions listed in Table 2.1. For more information on the computation of the source terms please refer to [131, 134, 135].

The equations of hydrodynamics and neutrino transport are discretized on a static spatial and energy grid and solved using a 2nd-order time-explicit Runge-Kutta integrator with the time-step being limited by a CFL criterion [153]. ALCAR uses a conservative finite-volume method. That is the quantities are discretized as cell-volume averages. For the evolution, they are interpolated at the cell interfaces and an approximate Riemann solver calculates fluxes via these boundaries.

2.2 Implementation of Neutrino Flavor Conversions in the ALCAR Code

As mentioned in Section 1.2 neutrino flavor conversions are expected to happen in the inner regions of CCSNe but by no means everywhere and at all times. Their occurrence depends on the type of instability that triggers the conversions (most importantly slow modes, fast modes, and collisional instabilities) but the details are still subject to intense investigation (Section 1.2). There is evidence that regions of instability can be robustly detected by looking for crossings of the angular distribution of the electron lepton number [85]. However searches for these have the drawback of being applied to simulations that do not include flavor conversions. If the feedback to the stellar medium

Table 2.1 Neutrino matter interactions included in the simulations.

Type of interaction	reference
Absorption and emission (ν_e and $\bar{\nu}_e$ only)	
$n + \nu_e \rightleftharpoons p + e^-$	[145, 146][a]
$p + \bar{\nu}_e \rightleftharpoons n + e^+$	[145, 146][a]
$(A, Z) + \nu_e \rightleftharpoons (A, Z + 1) + e^-$	[145, 146]
Scattering	
$n + \nu_i \rightleftharpoons n + \nu_i$	[145, 146][a]
$p + \nu_i \rightleftharpoons p + \nu_i$	[145, 146][a]
$(A, Z) + \nu_i \rightleftharpoons (A, Z) + \nu_i$	[145, 146][b]
$e^\pm + \nu_i \rightleftharpoons e^\pm + \nu_i$	[145, 147, 148][c]
Pair processes (ν_x only)	
$e^- + e^+ \rightleftharpoons \nu_x + \nu_x$	[145, 149][d]
Bremsstrahlung (ν_x only)	
$N_1 + N_2 \rightleftharpoons N_1 + N_2 + \nu_x + \nu_x$	[145, 149][d]

[a] Including weak-magnetism and nucleaon recoil crrections [27]

[b] Including ion-screening corrections [150, 151]

[c] Damping the source terms for $\rho > 5 \times 10^{12}\,\mathrm{g\,cm^{-3}}$ [152]

[d] Simplified description as an absorption/emission process as in [152]

is as significant as predicted the medium will adapt to changes of the radiation field. Since a self-consistent implementation will remain computationally unfeasible in the near future, this study takes a more general approach. I implement a prescription that either converts a pair of electron (anti-)neutrinos to a pair of heavy lepton (anti-)neutrinos ($\nu_e, \bar{\nu}_e \rightarrow \nu_x, \nu_x$) or the other way round ($\nu_x, \nu_x \rightarrow \nu_e, \bar{\nu}_e$) to achieve a distribution where the flavors are maximally mixed. The procedure has already been published in [136]. Here I give a summary and show some test cases.

Each simulation is initialized with a critical density ρ_c as a parameter constant for this simulation. In those regions where the matter density ρ falls below ρ_c the flavor conversion prescription is applied. In 1D simulations this usually (but not always) means that the schematic prescription is applied in a region $r > r_\mathrm{c}$ exterior to the radius r_c where $\rho(r_\mathrm{c}) = \rho_\mathrm{c}$. As the matter density evolves with time, so does r_c while ρ_c remains constant. The density is a comparably inert property of matter. Effects of flavor conversions do not have strong direct consequences on the density. Therefore using the matter density prevents a frequent erroneous switching on and off of the criterion. Regions where flavor conversions have taken place can easily be identified just like regions that are unaffected, thus simplifying the analysis. Of course, dynamical changes in regions with flavor conversions can still lead to secondary changes in regions where no flavor conversions take place.

The parametric prescription to describe the amount of flavor conversion needs to follow the restrictions motivated by the nature of neutrino flavor conversions being a result of

coherent forward scattering (Section 1.2), that is

- the conservation of the total neutrino number and neutrino energy,
- the conservation of the neutrino momentum,
- the conservation of the (individual) lepton numbers, and
- satisfying Pauli's exclusion principle.

The last point, strictly speaking, does not follow from the nature of flavor conversions but still is a necessary constraint to be taken into account. In order to rigorously ensure the conservation requirements, the flavor conversion prescription is local in space and in energy. It is applied for each energy bin at each grid cell individually. In the following $E_{\nu_\alpha,q}$ is the energy density of a neutrino of species α in the q-th energy bin at a fixed position in space. Primed ($'$) quantities represent the states after applying the prescription and quantities without a prime represent the states before applying the prescription. The conservation of the total neutrino number at a given energy (energy conservation) translates to

$$\begin{aligned} E_{\nu_e,q} + 2E_{\nu_x,q} &= E'_{\nu_e,q} + 2E'_{\nu_x,q}\,, \\ E_{\bar{\nu}_e,q} + 2E_{\nu_x,q} &= E'_{\bar{\nu}_e,q} + 2E'_{\nu_x,q}. \end{aligned} \tag{2.11}$$

Note that the factor of 2 for ν_x in the conservation equation for neutrinos comes from the fact that ν_x represent both heavy lepton neutrinos. The same is true for the anti-neutrinos. The conservation of the electron lepton number[4] translates to

$$L_{e,q} = E_{\nu_e,q} - E_{\bar{\nu}_e,q} = E'_{\nu_e,q} - E'_{\bar{\nu}_e,q} = L'_{e,q}. \tag{2.12}$$

Under these constraints, a maximum equipartition of the flavors means that the energy density of all neutrino species but one be equal.

$$E_{\mathrm{eq},q} = \begin{cases} E'_{\bar{\nu}_e,q} = E'_{\nu_x,q} = \frac{1}{3}(E_{\bar{\nu}_e,q} + 2E_{\nu_x,q})\,, & \text{if } L_{e,q} > 0, \\ E'_{\nu_e,q} = E'_{\nu_x,q} = \frac{1}{3}(E_{\nu_e,q} + 2E_{\nu_x,q})\,, & \text{if } L_{e,q} \leq 0. \end{cases} \tag{2.13}$$

On top of that either ν_e or $\bar{\nu}_e$ keep the excess over the other that they had before equlibration. So the resulting distribution reads

$$E'_{\nu_e,q} = E_{\mathrm{eq},q} + \max(0, L_{e,q}), \tag{2.14a}$$

$$E'_{\bar{\nu}_e,q} = E_{\mathrm{eq},q} + \max(0, -L_{e,q}), \tag{2.14b}$$

$$E'_{\nu_x,q} = E_{\mathrm{eq},q}. \tag{2.14c}$$

The top row of Figure 2.1 shows a graphical representation of the the prescription

[4] Note that the number density and the energy density in the q-th energy bin of species α are related via $n_{\nu_\alpha,q} = \frac{E_{\nu_\alpha,q}}{\epsilon_q}$, with ϵ_q the central energy of the energy bin. So for individual energy bins number density and energy density can be used interchangeably.

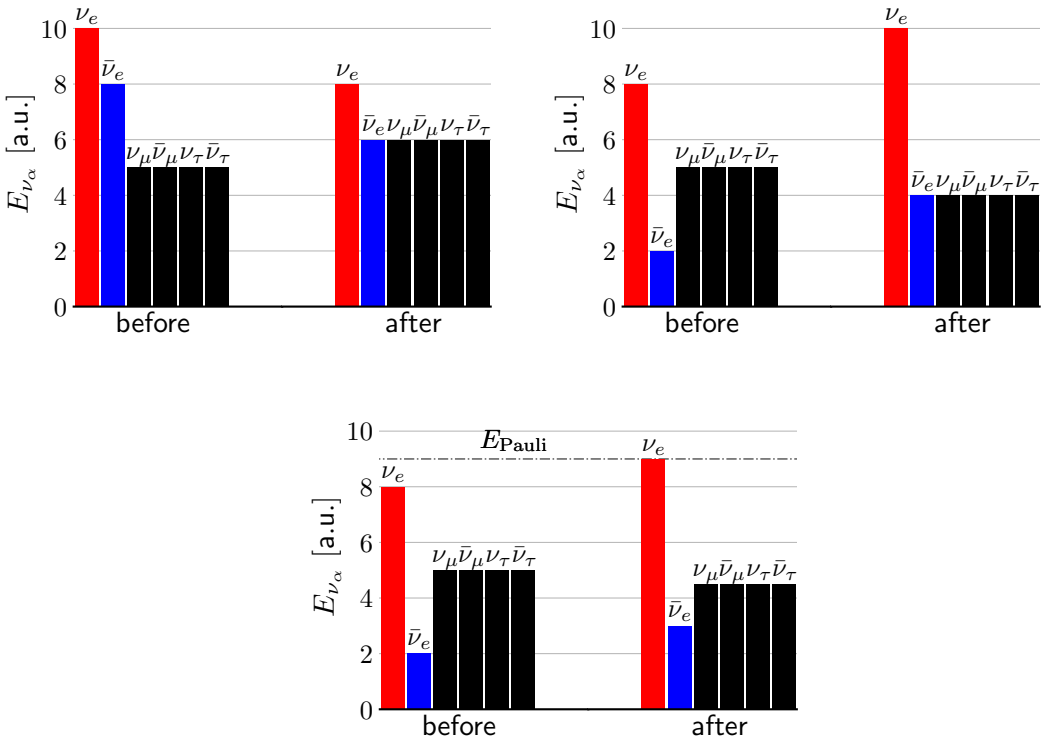

Figure 2.1 Top row: Schematic illustration of the equilibrium prescription introduced in Equations 2.14 for $L_{e,q} > 0$. The neutrino gas reaches an equipartition between ν_x and $\bar{\nu}_e$, which are less abundant than ν_e, with $L_{e,q}$ remaining unchanged. The left panel is for $\nu_e, \bar{\nu}_e \to \nu_x, \nu_x$ conversions, the right panel for $\nu_x, \nu_x \to \nu_e, \bar{\nu}_e$ conversions. Bottom row: Schematic representation of the equilibrium prescription under the constraint of the Pauli exclusion principle introduced in Equations 2.16 and for $L_{e,q} > 0$.

according to Equations 2.14.

In some cases, when either $E_{\text{Pauli}} \lessapprox E_{\nu_e} < E_{\nu_x} < E_{\bar{\nu}_e}$ or $E_{\text{Pauli}} \lessapprox E_{\bar{\nu}_e} < E_{\nu_x} < E_{\nu_e}$, with E_{Pauli} the maximum packing of fermionic particles allowed by Pauli's exclusion principle, the $\nu_x, \nu_x \to \nu_e, \bar{\nu}_e$ conversions as described in Equations 2.14 would result in a violation of the limit set by Pauli's exclusion principle. In ALCAR a the q-th energy bin is allowed to contain an energy density of

$$E_{\text{Pauli},q} = \frac{4\pi}{(2\pi\hbar c)^3}\epsilon_q^2(\epsilon_r - \epsilon_l), \tag{2.15}$$

with $\hbar$ the reduced Planck constant and ϵ_r and ϵ_l the upper and lower boundary of that energy bin. In this case the amount of conversion is restricted to the Pauli limit and

neutrino distribution reads

$$E'_{\nu_e,q} = \min(E_{\mathsf{Pauli},q},\ E_{\mathsf{Pauli},q} + L_{e,q}), \tag{2.16a}$$
$$E'_{\bar{\nu}_e,q} = \min(E_{\mathsf{Pauli},q},\ E_{\mathsf{Pauli},q} - L_{e,q}), \tag{2.16b}$$
$$E'_{\nu_x,q} = \tfrac{1}{2}(E_{\max,q} - E_{\mathsf{Pauli},q}), \tag{2.16c}$$

with

$$E_{\max,q} = \begin{cases} 2E_{\nu_x,q} + E_{\nu_e,q}\,, & \text{if } L_{e,q} > 0\,, \\ 2E_{\nu_x,q} + E_{\bar{\nu}_e,q}\,, & \text{if } L_{e,q} \leq 0 \end{cases} \tag{2.17}$$

the total number density of neutrinos or anti-neutrinos in the q-th energy bin. The bottom row of Figure 2.1 shows a graphical representation of the the prescription according to Equations 2.16.

For the neutrino energy flux density the only requirement is that the total of all flavors, $\boldsymbol{F}_{\mathrm{tot},q}$, must be conserved:

$$\boldsymbol{F}_{\nu_e,q} + \boldsymbol{F}_{\bar{\nu}_e,q} + 4\boldsymbol{F}_{\nu_x,q} = \boldsymbol{F}_{\mathrm{tot},q} = \boldsymbol{F}'_{\nu_e,q} + \boldsymbol{F}'_{\bar{\nu}_e,q} + 4\boldsymbol{F}'_{\nu_x,q}\,. \tag{2.18}$$

Therefore, there is no unique solution. Keeping the individual contributions constant complies with the requested conservation just as assigning $\boldsymbol{F}_{\mathrm{tot},q}/6$ to every species. Yet it is evident that both options are not suitable to describe the considered type of flavor conversions because there is no physical motivation. The 1st-order angular moment is analogous to the momentum of ordinary matter. Flavor conversions are a consequence of coherent forward scattering and no momentum is transferred. Therefore neutrinos that change their flavor will change the energy flux density of the species they convert from and to. However, there should be no additional change of the momentum. Therefore, I choose to implement an option that connects the change of the 1st-order angular moment to the change of the 0th-order angular moment. Let

$$\eta_{\nu_\alpha,q} = \frac{E'_{\nu_\alpha,q}}{E_{\nu_\alpha,q}}, \tag{2.19}$$

be the ratio of neutrino energy densities before and after the conversion. If $\eta_{\nu_\alpha,q} < 1$ then this equals the survival probability of ν_α and $(1 - \eta_{\nu_\alpha,q})$ is the fraction of neutrinos that changes their flavor. In regions where $\nu_e, \bar{\nu}_e \to \nu_x, \nu_x$ (i.e., $\eta_{\nu_e,q}, \eta_{\bar{\nu}_e,q} < 1$) I use

$$\boldsymbol{F}'_{\nu_e,q} = \eta_{\nu_e,q}\boldsymbol{F}_{\nu_e,q}, \tag{2.20a}$$
$$\boldsymbol{F}'_{\bar{\nu}_e,q} = \eta_{\bar{\nu}_e,q}\boldsymbol{F}_{\bar{\nu}_e,q}, \tag{2.20b}$$
$$\boldsymbol{F}'_{\nu_x,q} = \boldsymbol{F}_{\nu_x,q} + \frac{(1-\eta_{\nu_e,q})\boldsymbol{F}_{\nu_e,q} + (1-\eta_{\bar{\nu}_e,q})\boldsymbol{F}_{\bar{\nu}_e,q}}{4}, \tag{2.20c}$$

and in the regions where $\nu_x, \nu_x \to \nu_e, \bar{\nu}_e$(i.e., $\eta_{\nu_x,q} < 1$), I use analogously to Equations 2.20

$$\boldsymbol{F}'_{\nu_e,q} = \boldsymbol{F}_{\nu_e,q} + 2(1-\eta_{\nu_x,q})\boldsymbol{F}_{\nu_x,q}, \tag{2.21a}$$
$$\boldsymbol{F}'_{\bar{\nu}_e,q} = \boldsymbol{F}_{\bar{\nu}_e,q} + 2(1-\eta_{\nu_x,q})\boldsymbol{F}_{\nu_x,q}, \tag{2.21b}$$
$$\boldsymbol{F}'_{\nu_x,q} = \eta_{\nu_x,q}\boldsymbol{F}_{\nu_x,q}\,. \tag{2.21c}$$

This prescription ensures that the flavor conversions also effectively lead to the transfer of momentum from one species to another. For the species that becomes less abundant the flux factor $f = |\boldsymbol{F}|/cE$ remains constant during the flavor conversion in each energy bin q, i.e.,

$$f_{\nu_\alpha,q} = \frac{|\boldsymbol{F}_{\nu_\alpha,q}|}{cE_{\nu_\alpha,q}} = \frac{|\boldsymbol{F}'_{\nu_\alpha,q}|}{cE'_{\nu_\alpha,q}} = f'_{\nu_\alpha,q}. \tag{2.22}$$

This prescription is stable in the sense that applying it a second time does not further change the result because in this case $\eta_{\nu_\alpha,q} = 1$. Nevertheless, I have confirmed that the results are qualitatively unaffected by reasonable alternative prescriptions for the neutrino momentum behavior during flavor conversions.

The flavor conversion routines are applied after each Runge-Kutta (sub-)step of the temporal evolution to be consistent with flavor conversions that happen on time scales below the length of the time-step adapted in the calculations. This ensures that the calculations for the radiation transport and for the "ordinary" neutrino-interactions operate on flavor equilibrated states at all times.

2.2.1 Tests of the Implementation

In this subsection I show the steps I took to ensure the correctness of the implementation of the prescription. During the execution of the simulation program a small routine checks for the consistency with the conservation restrictions to machine precision. In all following figures in this section solid lines are obtained from simulations without flavor conversions as described in the caption. The dashed-dotted lines are the result of the application of a single time step with flavor conversions.

Figure 2.2 shows a case of the application of Equations 2.14 at a distance of 100 km at 70 ms after core bounce where neutrino densities are sufficiently small that Pauli blocking is not an issue. At $\epsilon \lesssim 15\,\mathrm{MeV}$, ν_e are more abundant than $\bar{\nu}_e$ and therefore $E'_{\nu_e} > E'_{\bar{\nu}_e} = E'_{\nu_x}$. At $\epsilon \gtrsim 15\,\mathrm{MeV}$, $\bar{\nu}_e$ are more abundant than ν_e and therefore $E_{\bar{\nu}_e} > E'_{\nu_e} = E'_{\nu_x}$. At $\epsilon \gtrsim 20\,\mathrm{MeV}$, ν_x are not the least abundant species and the type of conversion changes from $\nu_e, \bar{\nu}_e \rightarrow \nu_x, \nu_x$ conversions at lower and $\nu_x, \nu_x \rightarrow \nu_e, \bar{\nu}_e$ conversions at higher energies.

Figure 2.3 shows a case of the application of Equations 2.16 at a distance of 13 km at 50 ms after core bounce. In the lower energy bins ($\epsilon \lesssim 20\,\mathrm{MeV}$), E_{ν_e} is just below the limit of the Pauli exclusion principle (dashed lines) which causes a suppression of the flavor conversions. Note that $\bar{\nu}_e$ are the least abundant species due to the high degeneracy of electrons, which suppresses the production of $\bar{\nu}_e$. Therefore conversions are of type $\nu_x, \nu_x \rightarrow \nu_e, \bar{\nu}_e$ at all energies.

Figure 2.4 shows the radial dependence of the energy-integrated neutrino energy density $\overline{E}_{\nu_\alpha} = \sum_q E_{\nu_\alpha,q}$. In regions where $\rho < \rho_\mathrm{c}$, at $r > 98\,\mathrm{km}$, the flavor conversion prescription is applied. It is noteworthy that despite the aim of the flavor conversion prescription leading to a state of maximal mixing of the flavors, still a distinct ordering is obtained ($\overline{E}_{\nu_e} > \overline{E}_{\bar{\nu}_e} > \overline{E}_{\nu_x}$). This is because $\bar{\nu}_e$ have a higher mean energy than ν_e. Therefore, ν_e are more abundant than $\bar{\nu}_e$ at lower energies while it is the other way round

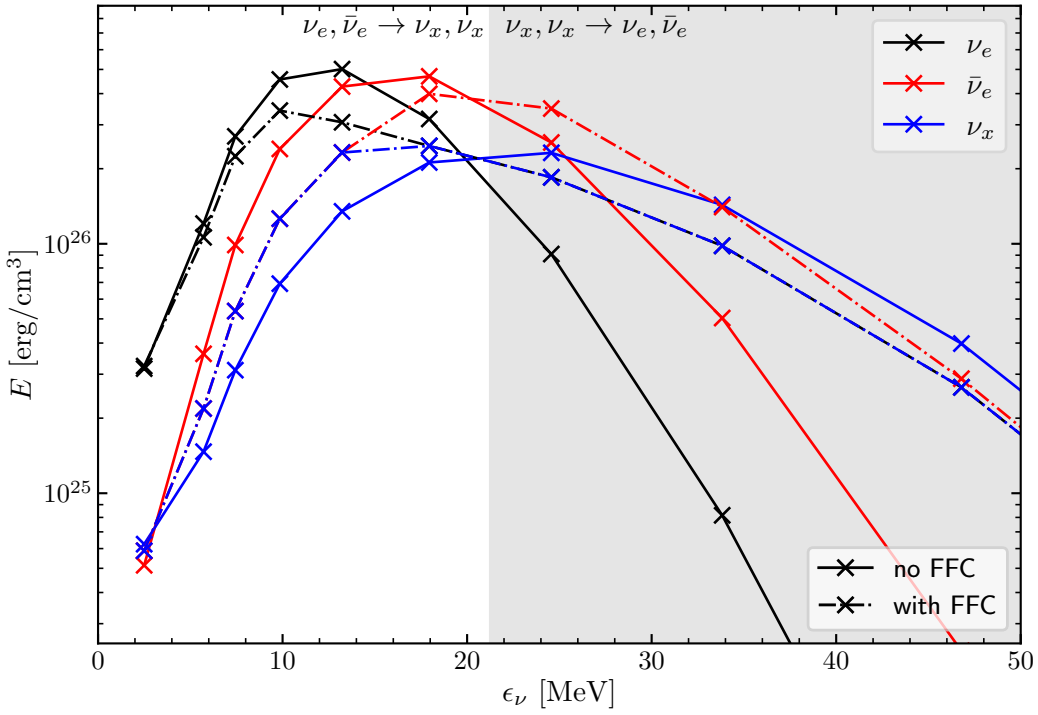

Figure 2.2 Test case of the implementation in spectral view. Dependence of the neutrino energy density, E, on the energy, ϵ, at a distance of 100 km before and after applying the flavor conversion prescription. Neutrino energy densities are sufficiently small that Pauli blocking is not an issue. The solid lines show data taken from model M9.0-1D-noFC at 70 ms after bounce. The dashed-dotted lines show data that is obtained when adding an additional time step including the flavor conversion prescription with $\rho_c = 10^{10}\,\mathrm{g\,cm^{-3}}$. In the unshaded region $\nu_e, \bar{\nu}_e \rightarrow \nu_x, \nu_x$ conversions take place. In the shaded region $\nu_x, \nu_x \rightarrow \nu_e, \bar{\nu}_e$ conversions take place. At $\epsilon \gtrsim 15$ MeV the electron lepton number changes sign.

at higher energies. The conservation of the energy dependent electron lepton number prevents one of $\overline{E}_{\nu_e}$ and $\overline{E}_{\bar{\nu}_e}$ to be equal to $\overline{E}_{\nu_x}$.

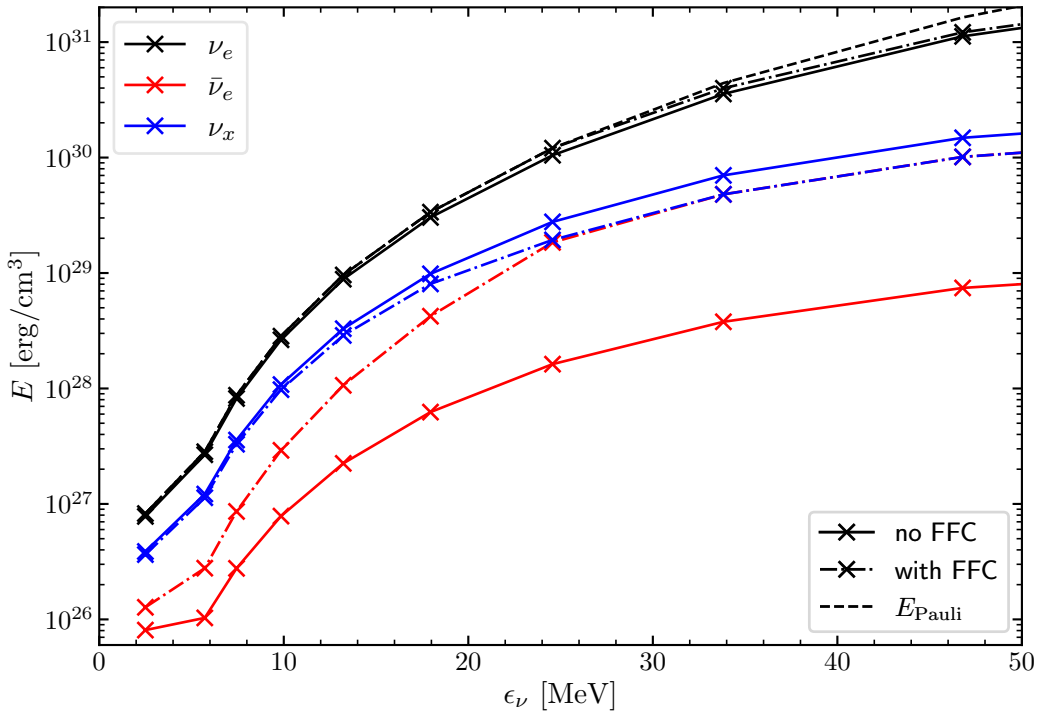

Figure 2.3 Test case of the implementation with the Pauli exclusion principle in spectral view. Dependence of the neutrino energy density, E, on the energy, ϵ, at a distance of 13 km before and after applying the flavor conversion prescription. The solid lines show data taken from model M20.0-1D-noFC at 50 ms after bounce. The dashed-dotted lines show data that is obtained when adding an additional time step including the flavor conversion prescription with $\rho_c = 10^{14}\,\mathrm{g\,cm^{-3}}$. The dashed line shows the maximum energy density allowed by the Pauli exclusion principle. For $\epsilon \lesssim 20$ MeV flavor conversions according to Equations 2.14 would result in a violation of the Pauli exclusion principle.

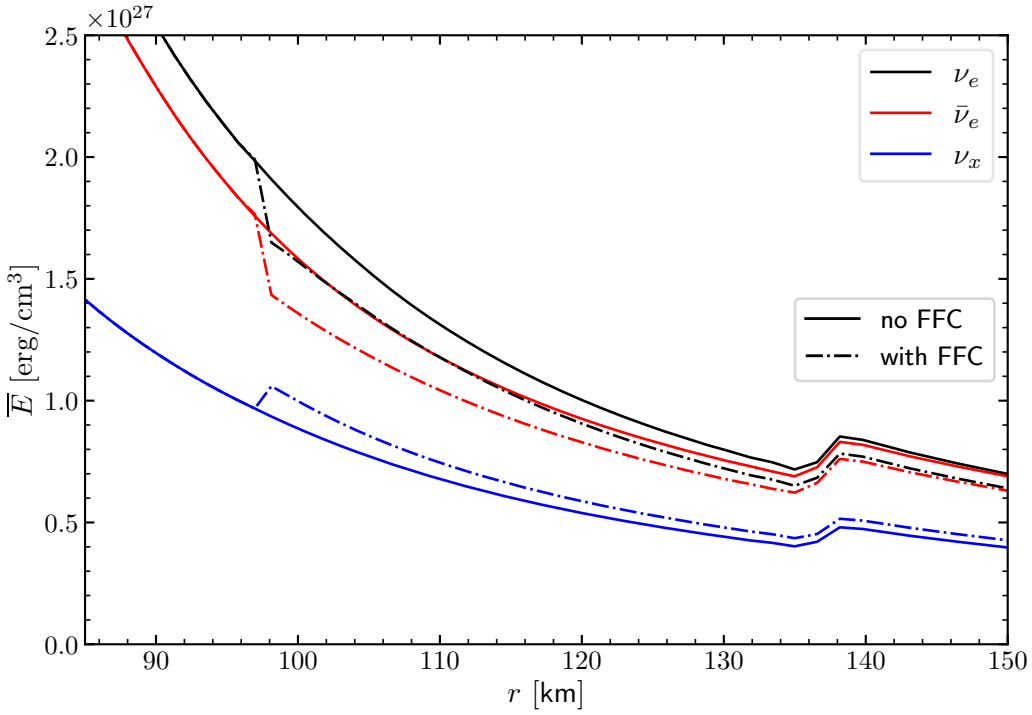

Figure 2.4 Test case of the implementation in radial view. Dependence of the energy integrated neutrino energy density ($\overline{E}$) on the distance to the center before and after applying the flavor conversion prescription. The solid lines show data taken from model M9.0-1D-noFC at 70 ms after bounce. The dashed-dotted lines show data that is obtained when adding an additional time step including the flavor conversion prescription with $\rho_c = 10^{10}\,\mathrm{g\,cm^{-3}}$. Note that neither $\overline{E}_{\nu_e}$ nor $\overline{E}_{\bar{\nu}_e}$ reaches down to $\overline{E}_{\nu_x}$ because the lepton number is energy dependent and changes sign (see Figure 2.2).

3 Core-Collapse Supernovae Simulations with Neutrino Flavor Conversions

Over the course of this thesis, I performed simulations of the collapse and accretion phase of 3 different progenitors with different zero-age main-sequence masses. The lightest progenitor model is an evolved $9.0\,M_\odot$ star [34]. It is an example of a progenitor model that consistently explodes in multi-D simulations [32, 41, 42, 134, 154]. In comparison, a $11.2\,M_\odot$ star [155] is usually less ready to blow up featuring a delayed and slower onset of shock expansion [156–159]. The third progenitor model, a $20.0\,M_\odot$ star [160], on the other hand exhibits a heavy iron core and a shallow density profile (Figure 3.1). Most multi-D simulations do not find a successful explosion from this progenitor [39, 41, 134, 161].

For each progenitor model I, ran simulations in 1D and 2D leading to a set of 6 series of simulations. For each series I, performed multiple simulations varying the critical

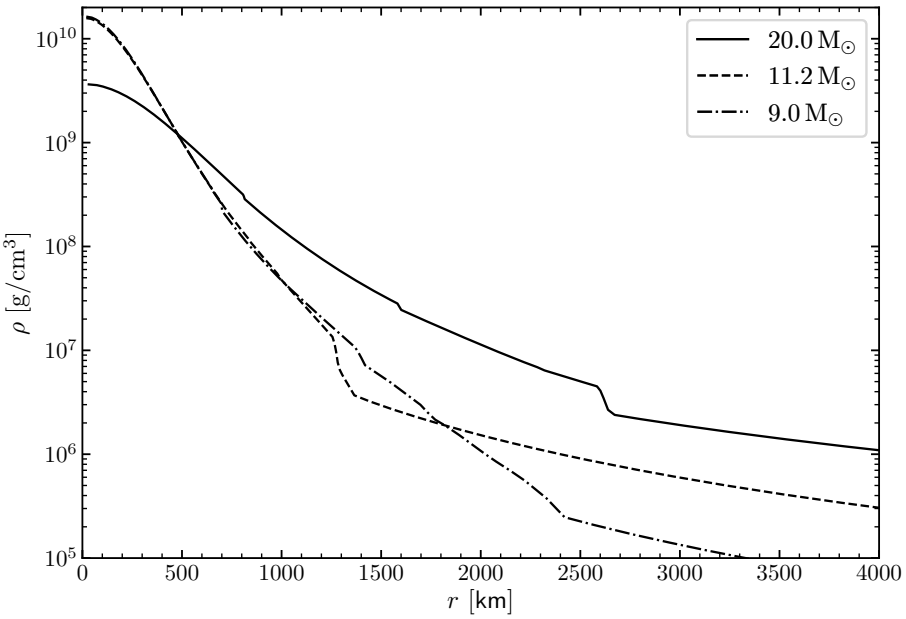

Figure 3.1 Density profiles of the used progenitors. The $9.0\,M_\odot$ and $11.2\,M_\odot$ progenitors feature a steep density profile that is usually associated with stars that are readily exploding in multi-D simulations. The $20.0\,M_\odot$ progenitor is more compact hampering an explosion.

density (ρ_c) below which flavor conversions take place. The convention for naming the simulations follows [162] and contains the zero-age main-sequence mass of the progenitor and indicates the dimensionality of the simulation as well as a notion of ρ_c: M9.0-1D-xxx, M11.2-1D-xxx, and M20.0-1D-xxx for the 1D models and M9.0-2D-xxx, M11.2-2D-xxx, and M20.0-2D-xxx for the 2D models, where xxx is a placeholder for either noFC ("no flavor conversion") or for the threshold density in units of $\mathrm{g\,cm^{-3}}$ in exponential notation. The values of ρ_c in units of $\mathrm{g\,cm^{-3}}$ chosen in this study are 10^9, 10^{10}, 10^{11}, 10^{12}, 10^{13}, or 10^{14}. The respective iso-density contours cover the region where the coupling of neutrinos to the stellar matter is strong enough to have an influence on the dynamical evolution. This leads to 7 simulations per series including the reference model, summing up to a total of 42 simulations that are the foundation for this thesis.

In the simulations, the radial grid is spaced logarithmically and consists of grid of 640 zones from 0 km up to 10,000 km. The 2D simulations are initialized with an output from the respective 1D simulation at $t_{\mathrm{pb}} = 5\,\mathrm{ms}$ after bounce and mapped to a polar grid with identical radial extent and spacing and 80 polar zones evenly spaced. To seed convection a random 0.1 % perturbation of the local density is applied. In these simulations, the innermost 2 km were calculated without polar dependency (1D core). Here, non-radial motions are essentially absent and the region can be calculated in spherical symmetry (1D core). In these simulations this volume is essentially treated as being spherically symmetric to avoid unnecessarily small time-steps according to the CFL-criterion [153]. The energy-dependent three species (ν_e, $\bar{\nu}_e$, ν_x) neutrino field is resolved on a grid of 15 logarithmically spaced cells from 0 MeV up to 400 MeV.

3.1 Simulations in Spherical Symmetry

In this section, I present the results of 21 simulations of accretion phase of 3 progenitor models in 1D. During the phase of collapse, I did not find differences between the simulations with no flavor conversions and the simulations with flavor conversions. The reason for this is that flavor conversions are implemented as a pairwise effect. During collapse ν_e and ν_x are practically absent so the effect of flavor conversions is negligible. As explained in Section 1.1, 1D simulations are inadequate to make robust predictions on the nature of CCSNe because they do not take into account non-radial hydrodynamic instabilities like convection inside the PNS and in the post-shock layer, which have a major influence for the explosion mechanism. Nevertheless, 1D simulations have a justification in this context because:

- Many consequences introduced by flavor conversions are present in 1D simulations. As I will show in this chapter, the effect of flavor conversions on the heating properties of neutrinos in different regions of the supernova has a significant influence on the dynamics also in 1D.

- The larger computational cost of mulit-D simulations exceeds the resources suitable for the testing phase of new features.

Table 3.1 Summary of 1D simulations. $r_{\mathrm{shock,max}}$ is the maximum expansion of the shock radius and $t_{\mathrm{shock,max}}$ is the time at which this is expansion is reached.

Label	M_{prog} [$\mathrm{M}_\odot$]	ρ_{c} [g/cm^3]	$r_{\mathrm{shock,max}}$ [km]	$t_{\mathrm{shock,max}}$ [ms]
M9.0-1D-noFC	9.0	x	143	106
M9.0-1D-1e09	9.0	10^9	144	109
M9.0-1D-1e10	9.0	10^{10}	153	106
M9.0-1D-1e11	9.0	10^{11}	137	108
M9.0-1D-1e12	9.0	10^{12}	130	47
M9.0-1D-1e13	9.0	10^{13}	135	336
M9.0-1D-1e14	9.0	10^{14}	117	40
M11.2-1D-noFC	11.2	x	207	102
M11.2-1D-1e09	11.2	10^9	256	125
M11.2-1D-1e10	11.2	10^{10}	281	129
M11.2-1D-1e11	11.2	10^{11}	240	114
M11.2-1D-1e12	11.2	10^{12}	195	97
M11.2-1D-1e13	11.2	10^{13}	152	91
M11.2-1D-1e14	11.2	10^{14}	149	91
M20.0-1D-noFC	20.0	x	146	72
M20.0-1D-1e09	20.0	10^9	148	81
M20.0-1D-1e10	20.0	10^{10}	153	80
M20.0-1D-1e11	20.0	10^{11}	134	53
M20.0-1D-1e12	20.0	10^{12}	127	49
M20.0-1D-1e13	20.0	10^{13}	120	48
M20.0-1D-1e14	20.0	10^{14}	120	48

- The analysis of multi-D simulations is more complicated. The amount of the generated data is larger and angular dependencies add an additional layer of complexity making it harder to find relevant differences. In addition, taking angular averages can smear out relevant features.

Table 3.1 lists the most important properties of the simulations in the 1D set. None of the models lead to a successful explosion but the evolution of the shock radius, in particular its maximum expansion, $r_{\mathrm{shock,max}}$, is as a rough indicator of the proximity of a CCSN simulation to explosion.

3.1.1 M9.0-1D

The simulations in this series reveal a systematic and sensitive dependence of the shock radius on the value of the threshold density ρ_{c} (only model M9.0-1D-1e13 is to some degree an outlier). A higher value of ρ_{c} strongly correlates with a weaker shock expansion, manifesting itself in a smaller maximum radius. A similar, but much less spread, systematic ordering is present in the PNS radii, defined by the iso-density surface $\rho(r_{\mathrm{PNS}}) = 10^{11}\,\mathrm{g\,cm^{-3}}$. This comes with little surprise because the region between

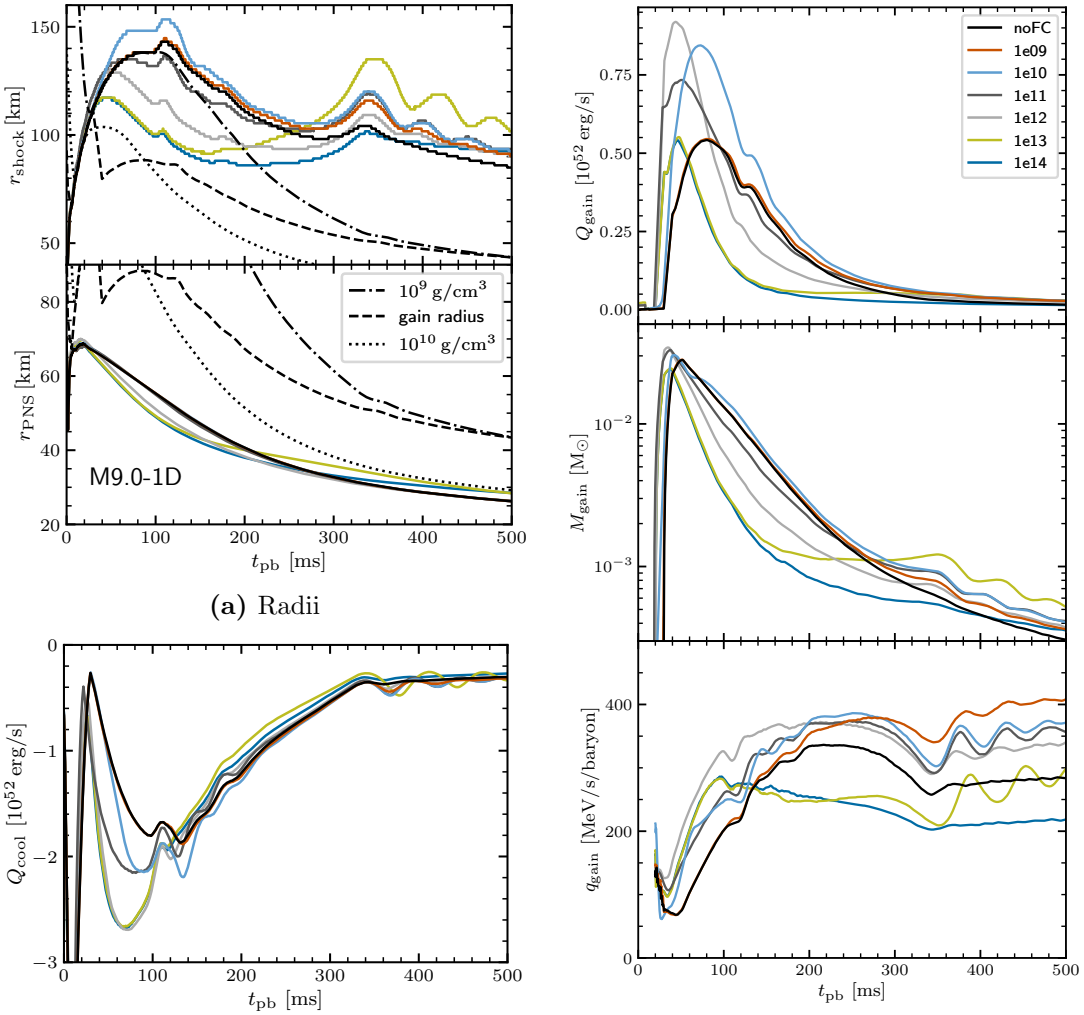

(a) Radii

(b) Cooling

(c) Heating

Figure 3.2 Dynamical properties of the M9.0-1D series. The color coding is according to the value of $\rho_{\rm c}$. (a): Shock radius ($r_{\rm shock}$, upper panel) and PNS radius ($r_{\rm PNS}$, lower panel) are strongly correlated; at the same time higher values of $\rho_{\rm c}$ correlate with a faster PNS contraction and thus a reduced expansion of the shock radius. Dashed-dotted, dashed, and dotted lines show the radius of the iso-density surfaces of $10^9\,\mathrm{g\,cm^{-3}}$ and $10^{10}\,\mathrm{g\,cm^{-3}}$ and the grain radius, respectively, of model M9.0-1D-noFC. (b): Total cooling in the cooling region ($Q_{\rm cool}$); higher values of $\rho_{\rm c}$ correlate with increased cooling (c): Heating properties in the gain region; all models with flavor conversion show higher specific heating rates ($q_{\rm gain}$); models with higher values of $\rho_{\rm c}$ correlate with smaller masses in the gain region ($M_{\rm gain}$) and therefore smaller total heating rates ($Q_{\rm gain}$).

the PNS surface and the stalled shock, in 1D simulations, is stratified in a way that is nearly in hydrostatic equilibrium during the post-bounce accretion phase [12, 28, 157]. Hence, the shock radius follows the contraction of the PNS.

The dynamical evolution of the M9.0-1D series can be divided in two parts. In the early phase ($t_{\rm pb} \lesssim 200\,{\rm ms}$), the shock radius of most flavor conversion models is reduced when compared to the reference model (Figure 3.2a). Only for models M9.0-1D-1e09 and M9.0-1D-1e10, the shock radius ($r_{\rm shock}$) extends as far as the reference model or even somewhat further. In the second phase ($t_{\rm pb} \gtrsim 200\,{\rm ms}$; the exact timing depends on the model), $r_{\rm shock}$ of the models with flavor conversion picks up pace again and exceeds the expansion of the shock radius of the reference model.

The weaker expansion of the shock radius in models M9.0-1D-1e11 – M9.0-1D-1e14 during the first phase is initiated by a more efficient cooling from neutrinos. Figure 3.2b shows $Q_{\rm cool}$, the total cooling rate by a net neutrino emission in the cooling layer. The cooling layer extends from the PNS surface up to the gain radius where the net effect of matter-neutrino interaction changes from cooling to heating. To guide the eye, both panels of Figure 3.2a show the gain radius for M9.0-1D-noFC which roughly agrees with the gain radius for the other models. In models M9.0-1D-1e12 – M9.0-1D-1e14, $Q_{\rm cool}$ can be more than twice as high as in the reference model. In these models, flavor conversions also enhance the cooling inside the PNS. This leads to a faster contraction that also reduces the masses in the gain layer due to the stratification mentioned above. The gain layer reaches from the gain radius to the shock radius. The effects of the cooling are strong enough that the shock radius is already well retreating at around $t_{\rm pb} = 105\,{\rm ms}$, a time when it reaches its maximum expansion in the reference model.

On the other hand, in models M9.0-1D-1e09 and M9.0-1D-1e10 flavor conversions do not happen in the cooling layer (or at least not from the beginning on). Therefore, the contraction of the PNS is not substantially enhanced. In model M9.0-1D-1e09, $r_{\rm shock}$ extends a little beyond and in model M9.0-1D-1e10 considerably further than in the reference model. This originates in an increased heating by the neutrinos in the grain region, the properties of which are schown in Figure 3.2c. The lower panel shows the specific heating rate in the gain region

$$q_{\rm gain} = \frac{Q_{\rm gain}}{M_{\rm gain}}, \tag{3.1}$$

with $Q_{\rm gain}$ (upper panel) the total heating rate in the gain region and $M_{\rm gain}$ (middle panel) the total mass in the gain region. While $q_{\rm gain}$ reflects the impact of the flavor conversions on the neutrino properties that determine the energy deposition in the post-shock layer, $Q_{\rm gain}$ is more directly responsible for the development of the shock expansion but depends sensitively on the mass in the gain layer. $M_{\rm gain}$ can change due to increased cooling in the cooling layer as described above. Interestingly, $q_{\rm gain}$ in the models with flavor conversions is strikingly higher than in the reference model. So flavor conversions, implemented with the recipe presented in Section 2.2, increase the heating in the heating region and increase the cooling in the cooling region.

This is by no means a generic result of flavor conversion but the result of two competing effects from two different types of conversions. At lower densities—outside of the PNS

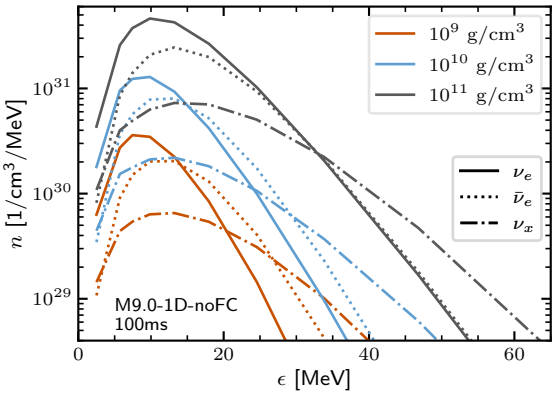

Figure 3.3 Neutrino spectra as function of neutrino energy at different densities for model M9.0-1D-noFC at $t_{\rm pb} = 100\,{\rm ms}$. The energy at which ν_x are not the least abundant species increases with density.

core— I find $\nu_e, \bar{\nu}_e \to \nu_x, \nu_x$ conversions at lower and medium energies, where ν_x are the least abundant species, and $\nu_x, \nu_x \to \nu_e, \bar{\nu}_e$ conversions at higher energies, where ν_e or $\bar{\nu}_e$ are the least abundant species. Conversions of type $\nu_e, \bar{\nu}_e \to \nu_x, \nu_x$ decrease the specific heating rate because ν_x transfer much less energy to the stellar medium. They are less tightly coupled. Hence, the newly formed ν_x can escape the region more easily and therefore can also enhance the cooling. On the other hand, conversions of type $\nu_x, \nu_x \to \nu_e, \bar{\nu}_e$ increase the heating rate because the newly formed ν_e and $\bar{\nu}_e$ interact much stronger with the medium because they can be absorbed in β-like reactions, which is kinematically forbidden for (most) ν_x.[1] Due to the quadratic dependence of the interaction cross section on the neutrino energy, the effect of conversions of high energy ν_x to electron type neutrinos is over-proportionally relevant and can compensate a net reduction of the number of ν_e and $\bar{\nu}_e$.

Specifically, the response of the specific heating rate depends on the energy at which conversions change from $\nu_e, \bar{\nu}_e \to \nu_x, \nu_x$ to $\nu_x, \nu_x \to \nu_e, \bar{\nu}_e$. Figure 3.3 shows the (unmixed) spectra of the three neutrino species (indicated by linestyles) for model M9.0-1D-noFC at $t_{\rm pb} = 100\,{\rm ms}$ at different densities as indicated by the color coding. As the density increases, the shapes and heights of the spectra[2] change due to the varying temperature and different interaction strengths of the different species. Therefore, the energy at which the type of conversions changes, increases as well and so does the fraction of neutrinos that undergo $\nu_e, \bar{\nu}_e \to \nu_x, \nu_x$ conversions. Broadly speaking, in the heating region the energy at which the type of the conversion changes is sufficiently small so the overall effect of conversions is to increase the heating. In the specific example of Figure 3.3, flavor conversions at a density of $10^{11}\,{\rm g\,cm^{-3}}$ would lead to $\nu_x, \nu_x \to \nu_e, \bar{\nu}_e$ conversions only for neutrinos with energies above 33 MeV, while conversions at a density of $10^{9}\,{\rm g\,cm^{-3}}$ would lead to these conversions for neutrinos with enegies above 20 MeV.

[1] Only a very small fraction has an energy that is above the rest mass of muons.
[2] and with it the differences of the shapes of the spectra

But it should be noted that neither are the energies where these transitions happen constant in time nor is the association with the cooling and the gain layer precise. Still this gives an intuitive explanation for the fact that the effects in the heating and cooling layer go into opposite directions.

Loosely speaking, in the cooling region and in the PNS mantle flavor conversions support the cooling. Since the coupling of neutrinos to the medium increases as the density increases the effects can be amplified at higher densities. Note that the increased cooling involves an increased emission of neutrinos. Also the following contraction involves compressional heating raising the mean energy of the emitted neutrinos. Therefore, increasing the cooling in the cooling region can increase q_{gain} as a secondary effect. The net effect on the expansion of the shock radius depends on the relative strength of the two effects. Comparing the different models, the volume where flavor conversions happen increases with ρ_{c}. For model M9.0-1D-1e09, the volume only covers a part of the heating region. Therefore, the shock expansion is slightly larger than in model M9.0-1D-noFC. In model M9.0-1D-1e10, a larger portion of the heating region is affected and r_{shock} is larger than in M9.0-1D-1e09. The gain radius is located at densities somewhere between a few $10^9\,\mathrm{g\,cm^{-3}}$ and a few $10^{10}\,\mathrm{g\,cm^{-3}}$ (depending on the time that has passed since the bounce, Figure 3.2c). In model M9.0-1D-1e10, flavor conversions start in parts of the cooling region at $t_{\mathrm{pb}} \gtrsim 60\,\mathrm{ms}$. At this time, the shock radius (and with it the size of the gain region) has grown large enough that the additional cooling in the cooling layer can fully be compensated. r_{shock} remains larger than in model M9.0-1D-noFC and M9.0-1D-1e09. In model M9.0-1D-1e11, flavor conversions happen in the cooling region from early on. There is no period of solely increased heating which could have lead to an increase of M_{gain}. Therefore, the shock expansion in this model is smaller than in models M9.0-1D-noFC, M9.0-1D-1e09, and M9.0-1D-1e10. Models M9.0-1D-1e12 – M9.0-1D-1e14 follow the trend of M9.0-1D-1e11 and have an even more decreased shock expansion because the cooling effect $\nu_e, \bar{\nu}_e \rightarrow \nu_x, \nu_x$ conversions is also present in the mantle of the PNS further reducing r_{PNS}.

In the second phase ($t_{\mathrm{pb}} \gtrsim 200\,\mathrm{ms}$), the contraction of the PNS in the reference model catches up with the contraction of those models where flavor conversions have accelerated the cooling. In this phase the overall magnitude of the cooling has decreased significantly and therefore also its relative importance. The masses in the gain layer converge. For all models with flavor conversion (except M9.0-1D-1e14) the total heating rate in the gain region exceeds the one of the M9.0-1D-noFC. When the O-shell is accreted at $t_{\mathrm{pb}} \simeq 320\,\mathrm{ms}$, consequently, r_{shock} extends further than the reference model.

Models M9.0-1D-1e13 and M9.0-1D-1e14 do not follow the trend of laid out by the other models with flavor conversions. At later times, the expansion of the shock radii exceeds the one of the other models. r_{PNS} and M_{gain} decrease slower (Figures 3.2a and 3.2c), and q_{gain} remains smaller than in the reference model. For model M9.0-1D-1e13, the largest expansion of the shock radius does not occur in the phase of the first shock expansion but following the accretion of the C-burning shell. The reason for this lies in the PNS core. In the first $\sim 100\,\mathrm{ms}$ after bounce the PNS radius contracts fastest for models M9.0-1D-1e13 and M9.0-1D-1e14. But strictly speaking the contraction of r_{PNS} tracks only the contraction of the outer layers of the PNS. In the inner regions, flavor

conversions slow down the contraction instead of accelerating it. Again this is caused by a change of the type of conversions. At densities above more than a few $10^{12}\,\mathrm{g\,cm^{-3}}$ the degeneracy of electrons increases which leads to a reduction of $\bar{\nu}_e$. Consequently, ν_x are not the least abundant species anymore and the type of conversion switches to $\nu_x, \nu_x \rightarrow \nu_e, \bar{\nu}_e$ conversions—at all energies. The newly formed $\bar{\nu}_e$ are immediately absorbed by the medium instead of escaping comparably unhindered like the ν_x would. The conversions therefore slow down the energy transport in the form of ν_x. The local temperature increases leading to a thermal expansion slowing down the contraction of the inner part of the PNS. So after (a few) 100 ms the contraction of the outer parts of the PNS slows down as well. The diminished contraction of the PNS also stabilizes M_{gain}. Due to the reduced energy transport within the PNS the emission of neutrinos remains at a higher level for a longer time. Finally, the increased M_{gain} enables a stronger shock expansion. In M9.0-1D-1e14 the effect is smaller and happens at later times because the conversions start deeper within the core and at $\rho = 10^{14}\,\mathrm{g\,cm^{-3}}$ the heavy lepton neutrino luminosity is smaller.

Flavor conversions also leave an imprint on the neutrino signatures that could be measured by a distant observer (Figure 3.4). They reduce the luminosity of ν_e and $\bar{\nu}_e$ while increasing the luminosity of ν_x. This confirms that the dominant conversion is of type $\nu_e, \bar{\nu}_e \rightarrow \nu_x, \nu_x$. The distribution of unmixed neutrinos of different flavors follows spectra of different mean energies. For heavy lepton type neutrinos, decoupling occurs in regions deep inside the PNS. Their spectra are typically hotter than those of $\bar{\nu}_e$ which in turn couple slightly stronger to the medium than ν_e. So the spectrum of $\bar{\nu}_e$ is hotter than the spectrum of ν_e. Flavor conversions mix these spectra and therefore increase the mean energy of ν_e and $\bar{\nu}_e$ while reducing the mean energy of ν_x. The luminosities and mean energies of models M9.0-1D-1e09 and M9.0-1D-1e10 are very similar but clearly distinct from M9.0-1D-noFC. This difference (especially for M9.0-1D-1e09) can solely be ascribed to the flavor conversion itself. It neither stems from an altered production of neutrinos (which only interact rarely at these densities) nor from drastically different dynamics (see discussion above). For the other models it is interesting to see that their influence on the dynamics is so strong that in a brief period of a few 10 ms the ν_e and ν_x luminosities exceed those of the respective luminosities in the reference model despite the general trend of flavor conversions which is to reduce the luminosity of ν_e. This implies that the accelerated contraction goes hand in hand with an accelerated deleptonization that can overcompensate the loss of ν_e from $\nu_e, \bar{\nu}_e \rightarrow \nu_x, \nu_x$ conversions.

The effects described in this section are, with a few exceptions, generic for simulations in 1D. To summarize, the effects are:

- Flavor conversions reduce the ν_e and $\bar{\nu}_e$ luminosity and increase the ν_x luminosity.
- Flavor conversions increase the ν_e and $\bar{\nu}_e$ mean energy and reduce the ν_x mean energy.
- $\nu_x, \nu_x \rightarrow \nu_e, \bar{\nu}_e$ Conversions at higher energies increase the specific heating rate in the heating region.

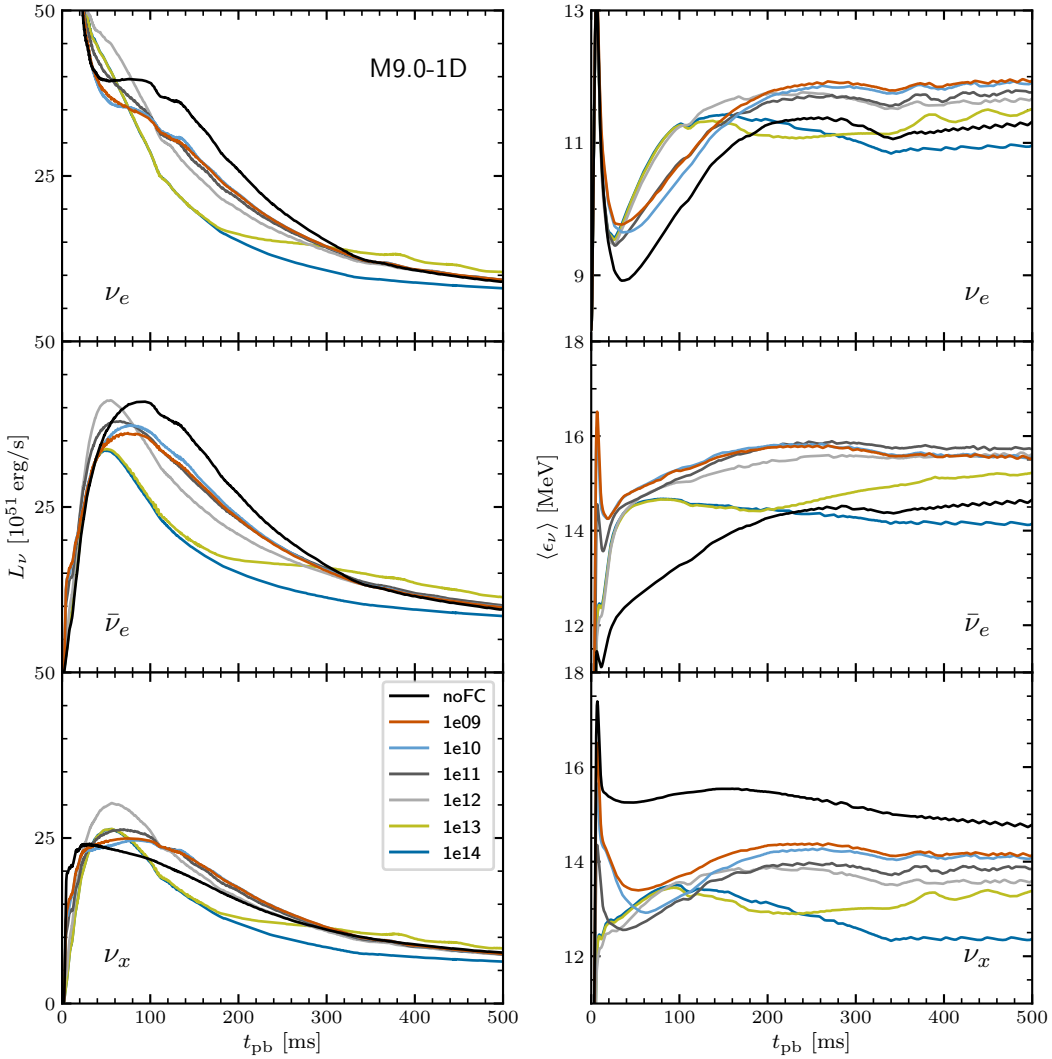

Figure 3.4 Luminosity (left) and mean energy (right) of ν_e (top), $\bar{\nu}_e$ (center), and ν_x (bottom) as functions of post-bounce time for the M9.0-1D series. In the top panel the maximum of the ν_e burst has been cut off for better visibility. The quantities are shown as measured by a distant observer, i.e. at a radius of 500 km, and transferred into the observer's lab-frame. Short-time fluctuations of the mean energy are reduced by smoothing the curves with a running average of 5 ms. In all models with flavor conversions the luminosity of ν_e and $\bar{\nu}_e$ is reduced while the luminosity of ν_x is increased as a consequence of flavor conversions. In models M9.0-1D-1e13 and M9.0-1D-1e14 the luminosity of ν_x is reduced due to the additional effect of reduced energy transport in the inner layers of the PNS. In models with flavor conversion the mean energies of ν_e and $\bar{\nu}_e$ are increased while the mean energies of ν_x are decreased. Also here, models M9.0-1D-1e13 and M9.0-1D-1e14 show secondary effects.

- $\nu_e, \bar{\nu}_e \rightarrow \nu_x, \nu_x$ Conversions at lower energies increase the cooling rate in the cooling region and the PNS mantle.

- $\nu_x, \nu_x \rightarrow \nu_e, \bar{\nu}_e$ Conversions in the PNS core reduce the energy transport and stabilize the PNS.

In the following sections I, will refer back to these effects and focus on the the additional aspects that arise from the different structure of the progenitors.

3.1.2 M11.2-1D

The M11.2-1D series shows the same correlation between the $r_{\mathrm{shock,max}}$ and ρ_{c} as in the M9.0-1D series. However, in the M11.2-1D series the shock expands rapidly very early on (Figure 3.5a). Even without flavor conversions this system is close to an explosion due to the steep decline of the density profile (Figure 3.1). Despite showing a dynamically different evolution, qualitatively the immediate effects of flavor conversions are the same as in the M9.0-1D series. Flavor conversions inside of the PNS accelerate its contraction via increased cooling rates (Figure 3.5b). Models M11.2-1D-1e12 – M11.2-1D-1e14 feature a reduced r_{shock} due to this effect. Outside of the PNS flavor conversions amplify the expansion because of increased heating rates (Figure 3.5c). The passing of the Si/Si-O interface[3] happens rather early. By coincidence this is at a time where flavor conversions strongly increase q_{gain}. For models M11.2-1D-1e09–M11.2-1D-1e11, these two effects add up and lead to a very pronounced shock expansion. Due to the limitations of spherical symmetry, where matter can only move outwards or inwards, the shock expansion completely throttles the mass accretion to the PNS which reduces the neutrino emission and thus the specific heating rate. The shock expansion ceases and the matter in the post-shock region collapses. As it returns to the vicinity of the PNS the neutrino emission (Figure 3.7) and the cooling rate (Figure 3.2b) increase drastically leading to transient peaks also in the heating rates. As a consequence, the shock radius shows a bounce-like pattern. The mass density in the Si/Si-O shell decreases only slowly and therefore also the mass accretion rate remains roughly constant (Figure 3.6). The dynamics steady down, the shock does not expand any further and all models reach a similar dynamical situation. At later times, only models M11.2-1D-1e13 and M11.2-2D-1e14 stand out because the contraction of the PNS progresses more slowly. The reasons for this are the same as in M9.0-1D-1e13, namely that the PNS contracts slower and so M_{gain} stabilizes which leads to a slower decrease of r_{shock} at $t_{\mathrm{pb}} \gtrsim 150\,\mathrm{ms}$.

Note that the models in this series show a slightly different systematic behavior of the neutrino emission and the specific heating in the gain layer when compared to the M9.0-1D series. This does not only include the additional collapse of matter leading to spike-like features in the luminosity and the mean energies (Figure 3.7). But also at later times, ongoing mass-accretion on the PNS increases the temperatures at the surface. Consequently the ν_e and $\bar{\nu}_e$ mean energies and therefore also the specific heating rate

[3] located at around 1300 km at the start of the simulation and being accreted at a distance of 400 km at around 80 ms after bounce

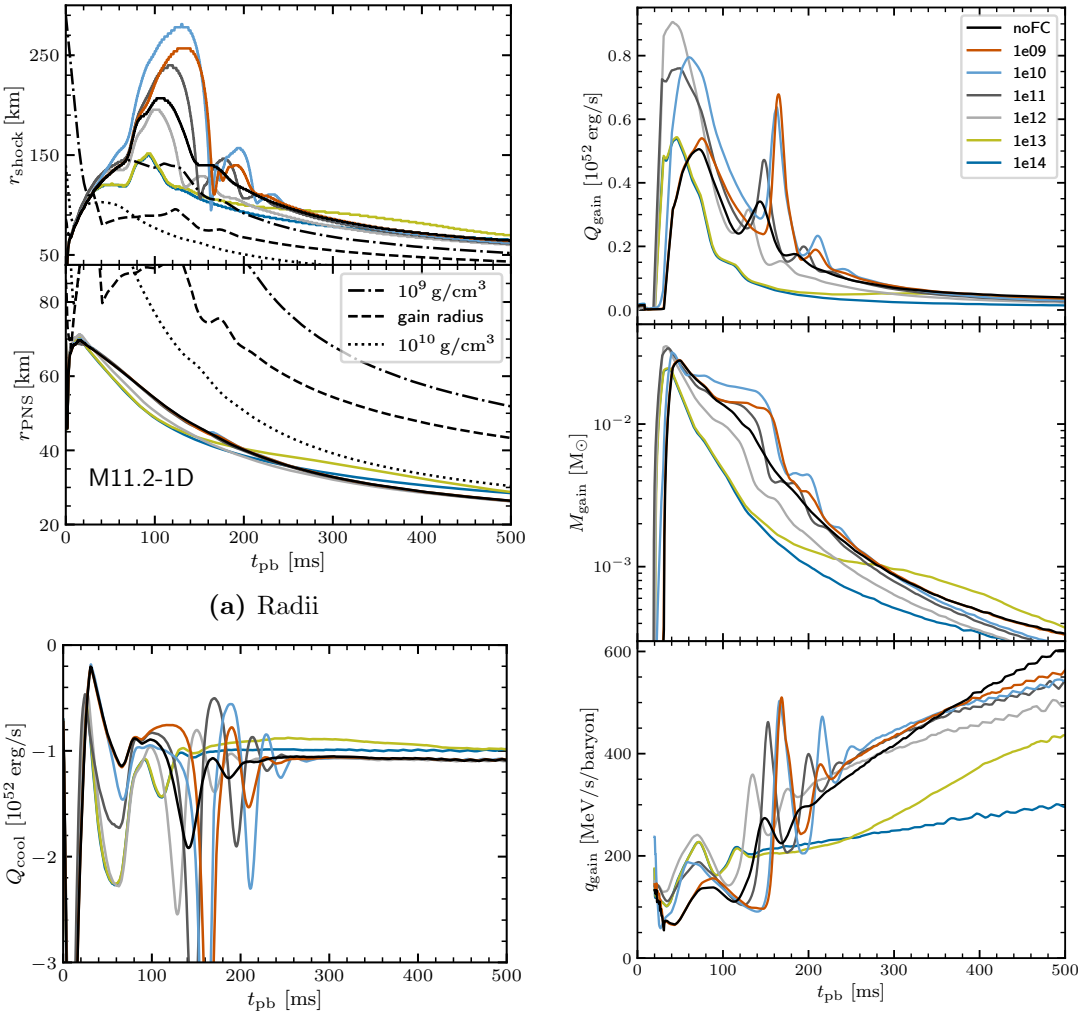

(a) Radii

(b) Cooling

(c) Heating

Figure 3.5 Dynamical properties of the M11.2-1D series. The color coding is according to the value of $\rho_{\rm c}$. (a): Early and strong shock expansion due to passing of the Si/Si-O interface; bounce-like feature in the due to limitations in 1D simulations (b): Total cooling in the cooling region ($Q_{\rm cool}$); short oscillatory features due to the collapse of the shock expansion (c): Heating properties in the gain region; models with flavor conversion tend to show higher specific heating rates ($q_{\rm gain}$); models with higher values of $\rho_{\rm c}$ correlate with smaller masses in the gain region ($M_{\rm gain}$) and therefore smaller total heating rates ($Q_{\rm gain}$)

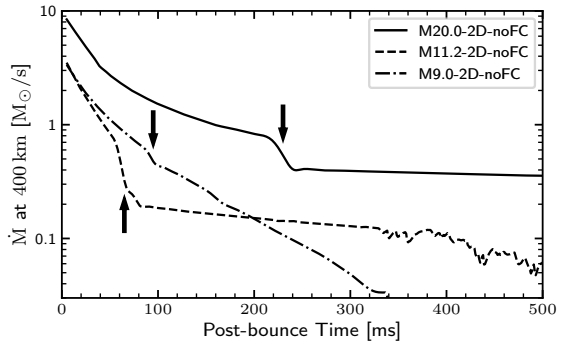

Figure 3.6 Mass accretion rates at 400 km elucidating the different progenitor structures. Arrows indicate the accretion of the Si/Si-O interface. The accretion rates in this figure are taken from 2D simulations but the accretion rates in the respective 1D simulations are the same.

increase. This can be seen most clearly in the reference model M11.2-1D-noFC (black lines in Figures 3.5c and 3.7). The mean energy of ν_x does not increase because they are produced in the inner region of the PNS. In this specific model the mean energies are even decreasing. The spectra of the different species approach each other and flavor conversions no longer lead to an increase of the specific heating rate, but instead tend to decrease it.

3.1.3 M20.0-1D

The results presented in this section were described already in [136]. Minor passages are taken from this reference which I contributed to as the first and leading author.

The M20.0-1D series shows the clearest correlation between the extension of the shock radius and the value of ρ_c (Figure 3.8a). This is because at no point in time any of the models is even close to successfully reviving the shock expansion. After the initial short period of shock expansion, lasting less than 100 ms, the dynamical evolution follows a steady contraction only briefly interrupted by the passing of the Si/Si-O interface at around $t_{pb} \sim 250$ ms.

Models M20.0-1D-noFC and M20.0-1D-1e09 evolve effectively identically. The position of the radius of the iso-density surface of $\rho = 10^9\,\mathrm{g\,cm^{-3}}$ is identical with the position of the shock radius for $t_{pb} \gtrsim 40$ ms (before it lies outside of it). The reference model does not include any flavor conversions. For model M20.0-1D-1e09 they occur only in the pre-shock region. This confirms that flavor conversions in the pre-shock region have no effect in terms of the dynamics. It shows that the (small) differences between the reference model and the model with $\rho_c = 10^9\,\mathrm{g\,cm^{-3}}$ in the M9.0-1D and M11.2-1D series can entirely be attributed to flavor conversions in a small volume of the heating region. Model M20.0-1D-1e10 shows the largest maximum expansion of the shock radius in this series, because of a short period of enhanced heating (Figure 3.8c). However, due to the shallow density gradient of the progenitor the iso-density surface of $10^{10}\,\mathrm{g\,cm^{-3}}$

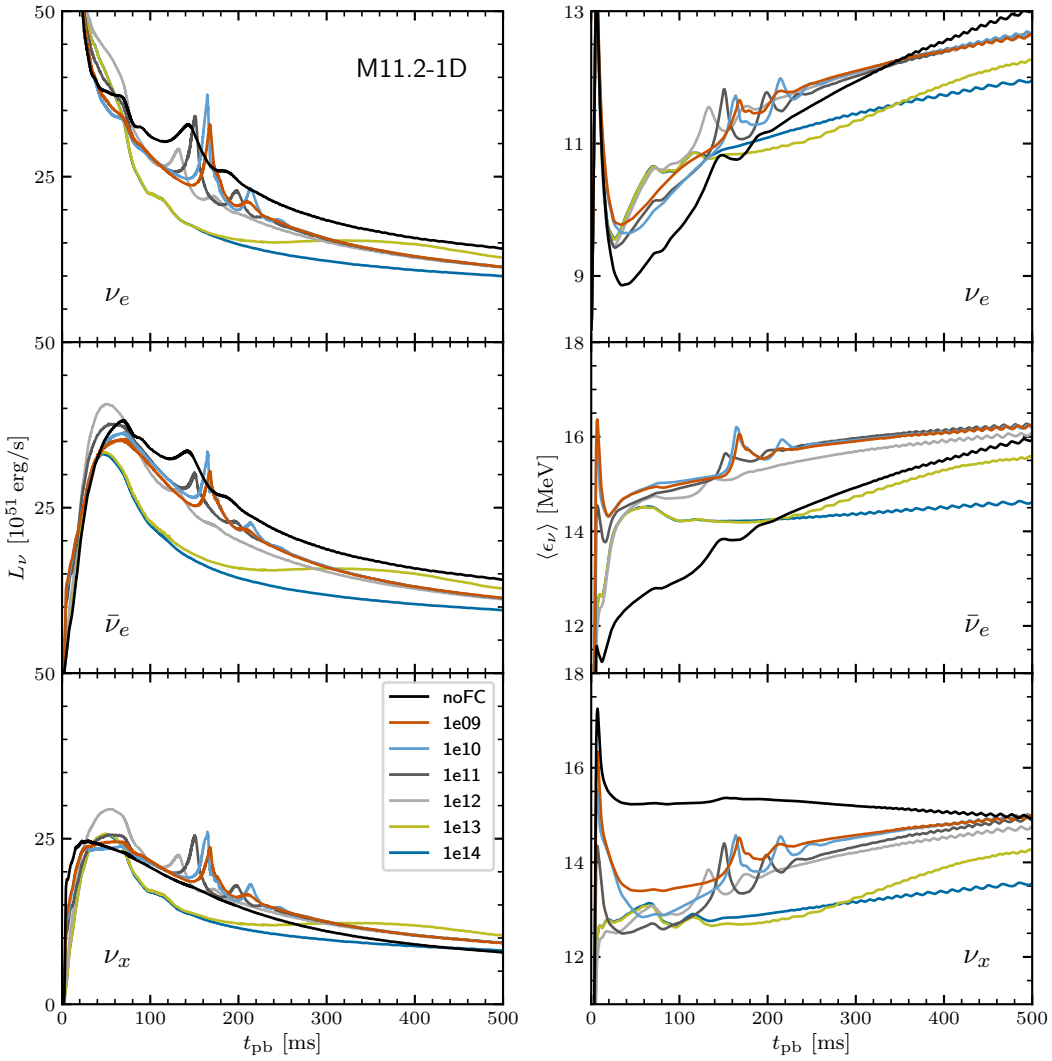

Figure 3.7 Luminosity (left) and mean energy (right) of ν_e (top), $\bar{\nu}_e$ (center), and ν_x (bottom) as functions of post-bounce time for the M11.2-1D series. In the top panel the maximum of the ν_e burst has been cut off for better visibility. The quantities are shown as measured by a distant observer, i.e. at a radius of 500 km, and transferred into the observer's lab-frame. Short-time fluctuations of the mean energy are reduced by smoothing the curves with a running average of 5 ms. In all models with flavor conversions the luminosity of ν_e and $\bar{\nu}_e$ is reduced while the luminosity of ν_x is increased as a consequence of flavor conversions. In models M11.2-1D-1e13 and M11.2-1D-1e14 the luminosity of ν_x is further reduced due to the additional effect of reduced energy transport in the inner layers of the PNS. In models with flavor conversion the mean energies of ν_e and $\bar{\nu}_e$ are increased while the mean energies of ν_x are decreased. This effect becomes weaker over time because the contraction of the ν_e and $\bar{\nu}_e$ neutrinospheres reduces the difference of the (unmixed) mean energies of the different flavors. Also here, models M9.0-1D-1e13 and M9.0-1D-1e14 show secondary effects.

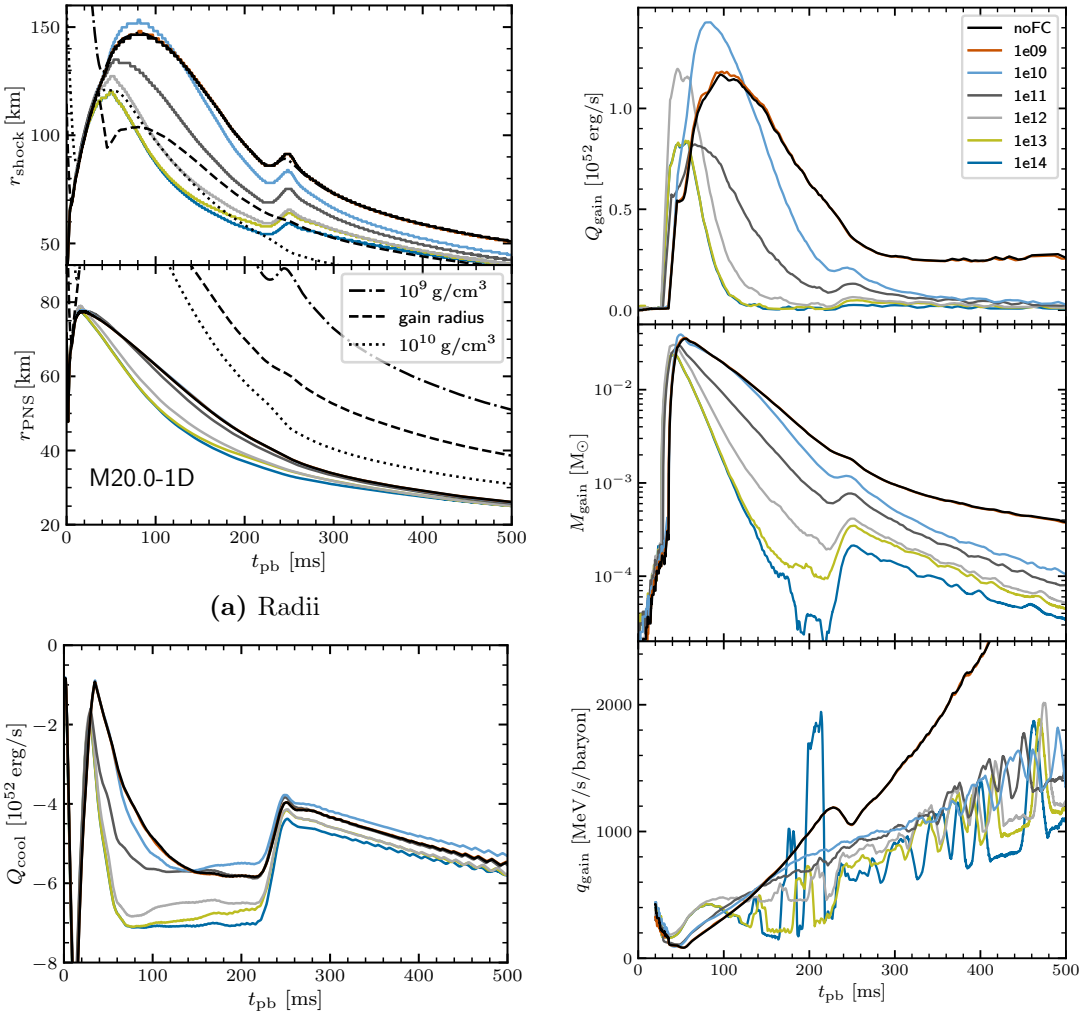

(a) Radii

(b) Cooling

(c) Heating

Figure 3.8 Dynamical properties of the M20.0-1D series. The color coding is according to the value of $\rho_{\rm c}$. (a): Weak shock expansion due to high accretion flow and strong PNS contraction (b): Total cooling in the cooling region ($Q_{\rm cool}$) (c): Heating properties in the gain region; models with flavor conversion show higher specific heating rates ($q_{\rm gain}$) only in the first ~ 100 ms after bounce; models with higher values of $\rho_{\rm c}$ have significantly smaller masses in the gain region ($M_{\rm gain}$) and therefore smaller total heating rates ($Q_{\rm gain}$)

crosses the gain radius comparably early and flavor conversions enhance the cooling in the cooling region just before contraction sets in after maximum shock expansion. This initiates a decrease of M_{gain}, decreasing the total heating rate which hinders the shock expansion. The shock radius retreats behind the shock radius of the reference model at $t_{\mathrm{pb}} \sim 130\,\mathrm{ms}$. In models M20.0-1D-1e11 – M20.0-1D-1e14 the much faster decrease of r_{shock} can directly be attributed to the cooling enhancing effect of $\nu_e, \bar{\nu}_e \rightarrow \nu_x, \nu_x$ conversions in the near-surface layers of the PNS (Figure 3.8b) that leads to an even faster contraction and faster decrease of M_{gain}. Though the Q_{cool} is temporarily decreased as a consequence of the passing of the Si/Si-O interface it remains high throughout the course of the simulation due to ongoing high mass accretion.

In general, this series confirms the findings of the previous two. During the initial period after bounce flavor conversions in the gain region enhance q_{gain}. For models M20.0-1D-1e12 – M20.0-1D-1e14, q_{gain} additionally increases because of an enhanced emission of neutrinos as a direct consequence of the increased cooling. At the same time matter sinks from the gain to the cooling layer leading to a net decrease of Q_{gain}. As accretion onto the PNS progresses, the temperatures near the ν_e and $\bar{\nu}_e$ neutrinospheres and the temperatures of the spectra of all flavors approach and eventually the mean energies of ν_e and $\bar{\nu}_e$ surpass that of ν_x. Over time the heating increasing effect of $\nu_x, \nu_x \rightarrow \nu_e, \bar{\nu}_e$ conversions is reduced while $\nu_e, \bar{\nu}_e \rightarrow \nu_x, \nu_x$ conversions still reduce the number of electron type neutrinos. At $t_{\mathrm{pb}} \approx 150\,\mathrm{ms}$, at the latest, the specific heating rates of the models with flavor conversions fall behind the heating rates of the reference model.

There is also a clear correlation between ρ_{c} and the luminosities and the mean energies (Figure 3.9). The faster contraction of the PNS is enabled by an increased overall emission of neutrinos. Hence, models with high values of ρ_{c} have higher ν_x luminosities and even the ν_e luminosities are increased during the first 80 ms after bounce. Afterwards, the electron type neutrino luminosities are reduced and only the luminosities of the heavy lepton type neutrinos are increased. Among the different models, a higher value of ρ_{c} correlates with lower luminosities. Flavor conversions increase the mean energies of ν_e and $\bar{\nu}_e$ and reduce the mean energies of ν_x. Models with higher values of ρ_{c} tend to have higher mean ν_e energies and lower ν_x energies. The reason for the energy ordering is again connected to an interplay of the strength of the PNS contraction and its influence on the temperatures at the neutrinospheres (for models M20.0-1D-1e12 – M20.0-1D-1e14), the dominant $\nu_e, \bar{\nu}_e \rightarrow \nu_x, \nu_x$ conversions in the bulk of the ν_e and ν_x spectra around their spectral peaks, and the $\nu_x, \nu_x \rightarrow \nu_e, \bar{\nu}_e$ conversions in the high-energy spectral tails. These conversions lead to an increase of the mean ν_e energies with higher threshold densities and similarly for the mean ν_x energies. The mean energies of $\bar{\nu}_e$ are mostly insensitive to the value of ρ_{c}.

As the mean energies of ν_e and $\bar{\nu}_e$ increases due to ongoing accretion the influence of flavor conversions becomes weaker. For ν_x on the other hand, the mean energy increases in models with flavor conversion while it stays roughly constant for the reference model.

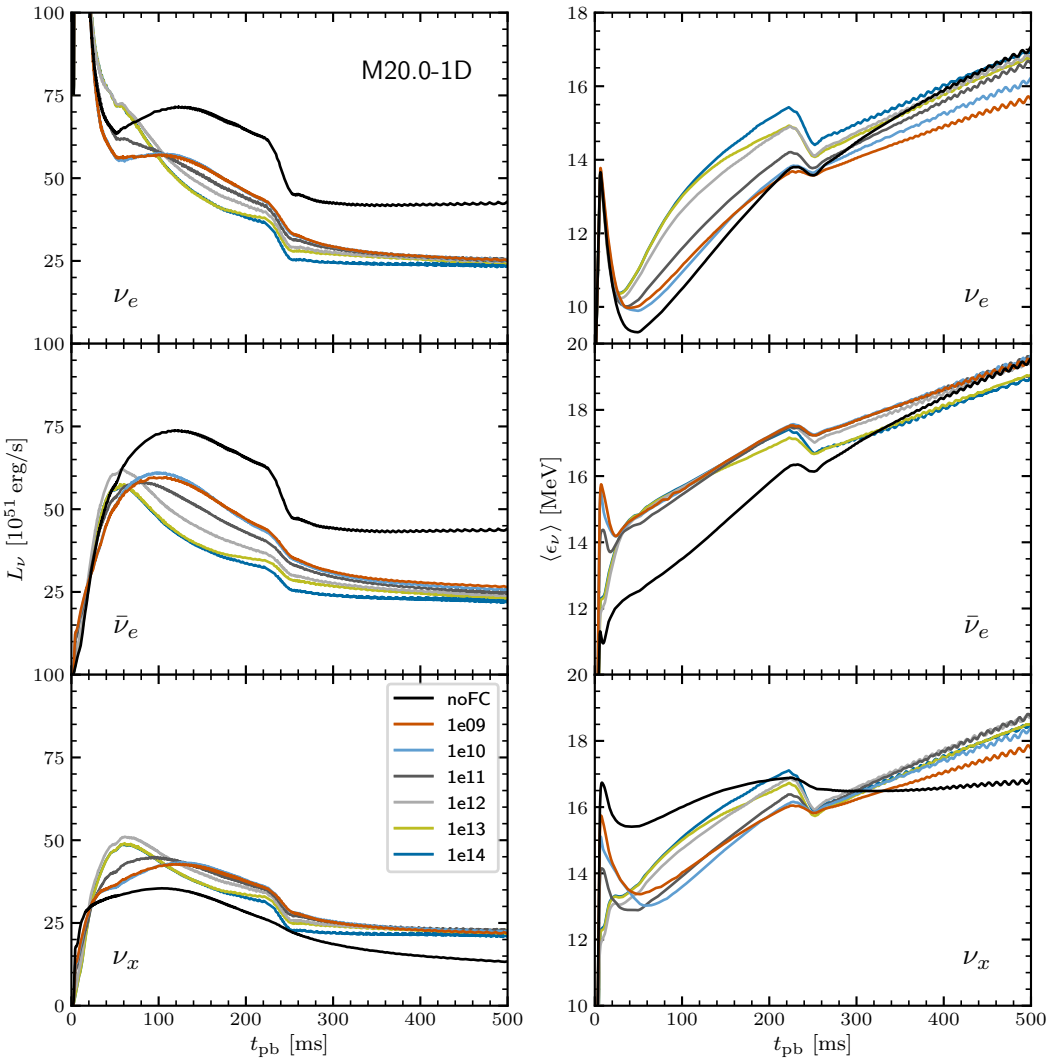

Figure 3.9 Luminosity (left) and mean energy (right) of ν_e (top), $\bar{\nu}_e$ (center), and ν_x (bottom) as functions of post-bounce time for the M20.0-1D series. In the top panel the maximum of the ν_e burst has been cut off for better visibility. The quantities are shown as measured by a distant observer, i.e. at a radius of 500 km, and transferred into the observer's lab-frame. Short-time fluctuations of the mean energy are reduced by smoothing the curves with a running average of 5 ms. In all models with flavor conversions the luminosity of ν_e and $\bar{\nu}_e$ is reduced while the luminosity of ν_x is increased as a consequence of flavor conversions. There is a clear correlation between the value of $\rho_{\rm c}$ and the strength of this effect. In models with flavor conversion the mean energies of ν_e and $\bar{\nu}_e$ are increased while the mean energies of ν_x are decreased. This effect becomes weaker over time because the contraction of the ν_e and $\bar{\nu}_e$ neutrinospheres reduces the difference of the (unmixed) mean energies of the different flavors.

3.2 Simulations in Axial Symmetry

In this section, I present the results of the 21 simulations of the accretion phase of the 3 progenitor models in 2D. The simulations in this series reveal that flavor conversions can act in different ways depending on the region where they occur and on the progenitor structure. All models in the M9.0-2D and M11.2-2D series show successful explosions while none of the models in the M20.0-2D series explodes within 500 ms after core bounce. Table 3.2 lists the most important properties of the simulations in 2D. The different outcomes of the series (exploding vs. non-exploding) can be attributed at large to the difference of the mass accretion rates caused by the progenitor structure. In the M9.0-2D and M11.2-2D series, the mass accretion rate (measured at a radius of 400 km) drops significantly below $1\,\mathrm{M}_\odot/\mathrm{s}$ well within 60 ms after core bounce while this value is reached only at around $t_\mathrm{pb} \sim 200$ ms in the M20.0-2D series (Figure 3.6). The effect of flavor conversions is non-uniform. In those series that lead to successful explosions they tend to facilitate the shock revival and lead to earlier explosions for some models. For the other models, the explosion occurs at the same time as in the respective reference model. In the M20.0-2D series on the other hand the shock expansion is diminished in models with flavor conversion when compared to the reference model though the effect is weaker than in the M20.0-1D series.

3.2.1 M9.0-2D

In model M9.0-2D-noFC, the reference model of the M9.0-2D series, the explosion sets in at $t_\mathrm{pb} \sim 350$ ms. Throughout this chapter I use the time when the mean shock radius passes 400 km as criterion for the onset of the explosion. I find distinctively earlier explosions for models with flavor conversions *outside* of the PNS (M9.0-2D-1e09 – M9.0-2D-1e11) and explosion times similar to model M9.0-2D-noFC for models with flavor conversions also reaching *into* the PNS (M9.0-2D-1e12 – M9.0-2D-1e14); see Figure 3.10a.

In model M9.0-2D-1e09, flavor conversions enter the post-shock region 100 ms after the bounce but are restricted to the gain region where $\nu_x, \nu_x \rightarrow \nu_e, \bar{\nu}_e$ conversions at high energies enhance q_gain (Figures 3.10a and 3.10c). Though q_gain increases only by a small amount, due to the small size of the region where flavor conversions are active, M_gain increases steadily. Therefore, compared to the reference model, also Q_gain increases steadily supporting the explosion, which sets in at $t_\mathrm{pb} \simeq 260$ ms, nearly 100 ms earlier than in model M9.0-2D-noFC. In model M9.0-2D-1e10, flavor conversions are active in a large part of the heating region from early on and q_gain is significantly enhanced. This facilitates the generation of convection in the post-shock layer (Figure 3.11), which prolongs the residence of matter in the gain layer. Compared to the reference model, M_gain and Q_gain are considerably increased. At $t_\mathrm{pb} \simeq 220$ ms, the explosion sets in; earliest in this series.

During the first 200 ms after bounce, the trajectory of the shock radius from model M9.0-2D-1e11 follows the one of the reference model. This is not because there is no difference between the two models but rather is the result of two competing effects

Table 3.2 Summary of 2D simulations. For models that exhibit a successful explosion $t_{400\,\mathrm{km}}$ is the time after bounce when the mean shock radius is located at $r = 400\,\mathrm{km}$, which I use as the time when explosion sets in, and $M_{\mathrm{PNS},500\,\mathrm{ms}}$ is the baryonic mass of the PNS at $t_{\mathrm{pb}} = 500\,\mathrm{ms}$. For the non-exploding models $r_{\mathrm{shock,max}}$ is the maximum expansion of the shock radius and $t_{\mathrm{shock,max}}$ is the time at which this is expansion reached.

Label	M_{prog} [$\mathrm{M}_\odot$]	ρ_{c} [$\mathrm{g/cm^3}$]	$t_{400\,\mathrm{km}}$ [ms]	$M_{\mathrm{PNS},500\,\mathrm{ms}}$ [$\mathrm{M}_\odot$]
M9.0-2D-noFC	9.0	x	350	1.362
M9.0-2D-1e09	9.0	10^9	252	1.353
M9.0-2D-1e10	9.0	10^{10}	218	1.346
M9.0-2D-1e11	9.0	10^{11}	268	1.353
M9.0-2D-1e12	9.0	10^{12}	332	1.358
M9.0-2D-1e13	9.0	10^{13}	337	1.358
M9.0-2D-1e14	9.0	10^{14}	343	1.358
M11.2-2D-noFC	11.2	x	409	1.354
M11.2-2D-1e09	11.2	10^9	151	1.321
M11.2-2D-1e10	11.2	10^{10}	139	1.301
M11.2-2D-1e11	11.2	10^{11}	171	1.328
M11.2-2D-1e12	11.2	10^{12}	411[a]	1.352
M11.2-2D-1e13	11.2	10^{13}	141	1.323
M11.2-2D-1e14	11.2	10^{14}	273	1.350
			$r_{\mathrm{shock,max}}$ [km]	$t_{\mathrm{shock,max}}$ [ms]
M20.0-2D-noFC	20.0	x	146	82
M20.0-2D-1e09	20.0	10^9	148	80
M20.0-2D-1e10	20.0	10^{10}	153	78
M20.0-2D-1e11	20.0	10^{11}	135	55
M20.0-2D-1e12	20.0	10^{12}	129	51
M20.0-2D-1e13	20.0	10^{13}	139	60
M20.0-2D-1e14	20.0	10^{14}	132	54

[a] The shock radius of this model crosses 400 km multiple times. This value is the one after which the explosion finally sets in.

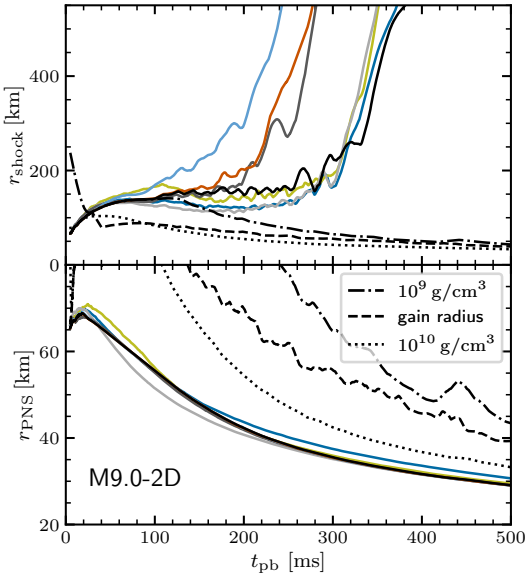

(a) Radii

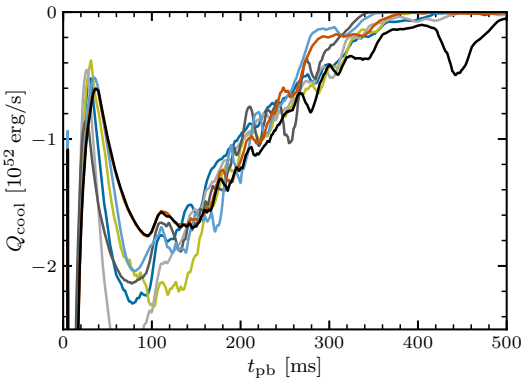

(b) Cooling

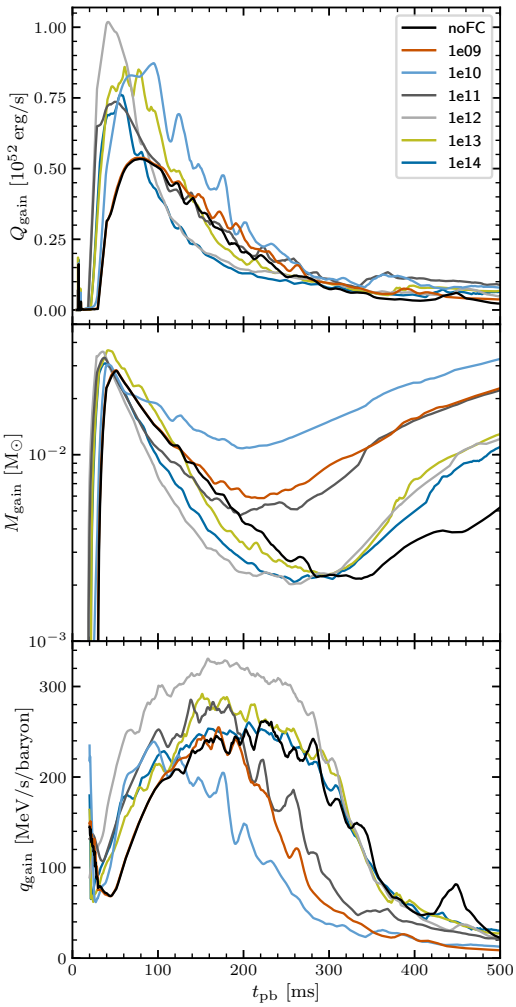

(c) Heating

Figure 3.10 Dynamical properties of the M9.0-2D series. The color coding is according to the value of $\rho_{\rm c}$. (a): PNS and shock radii are loosely correlated; at the same time higher values of $\rho_{\rm c}$ correlate with a faster PNS contraction and thus reduced expansion of the shock radius (b): Total cooling in the cooling region ($Q_{\rm cool}$); higher values of $\rho_{\rm c}$ weakly correlate with increased cooling (c): Heating properties in the gain region; all models with flavor conversion show higher specific heating rates ($q_{\rm gain}$); models with higher values of $\rho_{\rm c}$ correlate with smaller masses in the gain region ($M_{\rm gain}$) and therefore smaller total heating rates ($Q_{\rm gain}$).

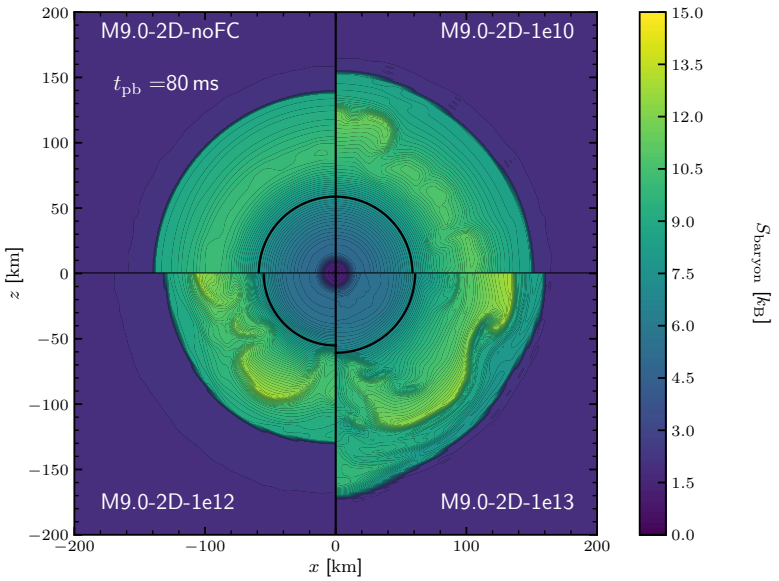

Figure 3.11 Beginning of the post-shock convection in the M9.0-2D series at $t_{\rm pb} = 80\,\rm ms$. Flavor conversions increase $q_{\rm gain}$, which facilitates the generation of convection in the post-shock region.

from flavor conversions in model M9.0-2D-1e11. Like in model M9.0-2D-1e10, $\nu_x, \nu_x \rightarrow \nu_e, \bar{\nu}_e$ conversions in the heating region increase $q_{\rm gain}$ and support the generation of convection, which is beneficial for the revival of the shock. On the other hand, $\nu_e, \bar{\nu}_e \rightarrow \nu_x, \nu_x$ conversions that are dominant in the cooling region enable a faster contraction. Therefore, $M_{\rm gain}$ decreases faster than in the reference model. Around $t_{\rm pb} = 100\,\rm ms$ the cooling rates become similar again (Figure 3.10b) while $q_{\rm gain}$ remains higher. $M_{\rm gain}$ approaches the value as in M9.0-2D-noFC and surpasses it at $t_{\rm pb} = 200\,\rm ms$. The shock radius expands and the explosion is launched at $t_{\rm pb} \simeq 270\,\rm ms$, again earlier than in the reference model. Model M9.0-2D-1e12 exhibits the same two competing effects. Compared to M9.0-2D-1e11, the effect on the $Q_{\rm cool}$ is stronger because the outer layers of the PNS are affected by enhanced cooling as well. The faster cooling can directly be seen in the contraction of the PNS radius that shrinks strongest in this series. Also the enhanced cooling reduces $M_{\rm gain}$ and results in a considerably weaker shock expansion. At the same time the contraction also leads to compressional heating increasing the neutrino emission and their mean energies in general (Figure 3.12). This leads to the largest value for $q_{\rm gain}$ in this series. At $t_{\rm pb} \sim 300\,\rm ms$, when the mass accretion rate has decreased sufficiently, $M_{\rm gain}$ stabilizes and explosion sets in about 50 ms later—for this and all other models not discussed yet. The fact that in these three and the reference model the explosion sets in roughly at the same time suggests that for these models the onset of shock expansion is less connected to details of altered neutrino physics but originates in the continuously decreasing mass accretion rate (Figure 3.6).

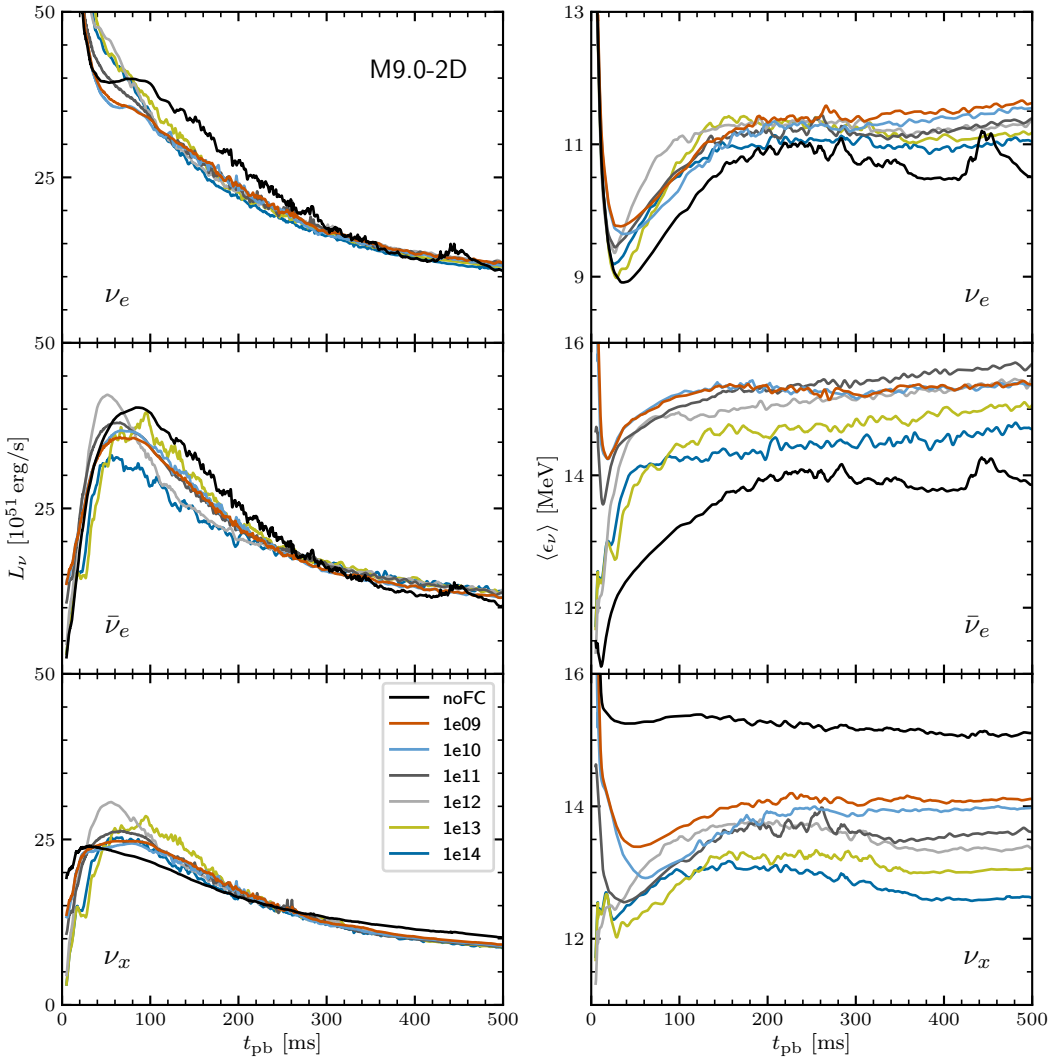

Figure 3.12 Neutrino properties for the simulations of the M9.0-2D series. Short-time fluctuations of the mean energy are reduced by smoothing the curves with a running average of 5 ms. All quantities are measured at a distance of 500 km and in the reference frame of a distant observer.

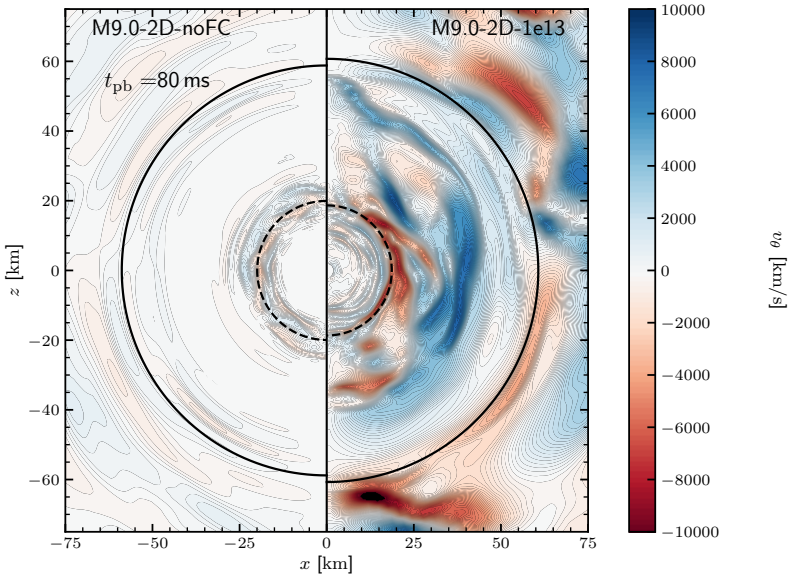

Figure 3.13 Lateral velocity (v_θ) indicating convection in models M9.0-2D-noFC (left) and M9.0-2D-1e13 (right) at $t_{\rm pb} = 80\,{\rm ms}$. The solid line shows the PNS radius and the dashed line shows the radius of the iso-density surface of $\langle\rho\rangle = 10^{13}\,{\rm g\,cm^{-3}}$, where $\langle\rho\rangle$ is the angle averaged matter density. Flavor conversions of type $\nu_x, \nu_x \rightarrow \nu_e, \bar{\nu}_e$ at $\rho \lesssim 10^{13}\,{\rm g\,cm^{-3}}$ lead to an increase of the local temperature which stirs PNS convection.

Models M9.0-2D-1e13 and M9.0-2D-1e14 where flavor conversions also happen in the PNS core, feature an additional effect originating in $\nu_x, \nu_x \rightarrow \nu_e, \bar{\nu}_e$ conversions in the inner regions of the PNS. Like their 1D counterparts, the newly formed $\bar{\nu}_e$ are quickly absorbed increasing the local temperature and effectively decreasing the *radiative* energy transport outwards. However, in 2D simulations non-radial motions are possible. Especially in model M9.0-2D-1e13, the increase of the local temperature stirs PNS convection (Figure 3.13). The critical density, $\rho_{\rm c}$, lies exactly in the convectively unstable region. The energy transport via PNS convection has a direct impact on the dynamics outside of the PNS because the energy is still coupled to the hydrodynamical system. This is different from the energy transport via ν_x, in which case the neutrinos decouple at densities of a few $10^{13}\,{\rm g\,cm^{-3}}$ from the stellar medium and the energy is lost radiatively. Furthermore, convection stabilizes the PNS against contraction and also leads to an increase of the matter temperatures in the outer parts of the PNS, increasing the production of ν_e and $\bar{\nu}_e$ [163]. In model M9.0-2D-1e13, flavor conversions increase the PNS convection right away. The PNS radius contracts slower than in all other models until $t_{\rm pb} = 100\,{\rm ms}$. Compared to M9.0-2D-1e12 and M9.0-2D-14, in this period, $Q_{\rm cool}$ is increased only to a minor degree. Within this series, model M9.0-2D-1e13 has the largest value of $M_{\rm gain}$ and the shock radius evolves similarly to the one in model M9.0-2D-1e10. However, the contraction of the PNS is merely delayed. About 100 ms after bounce,

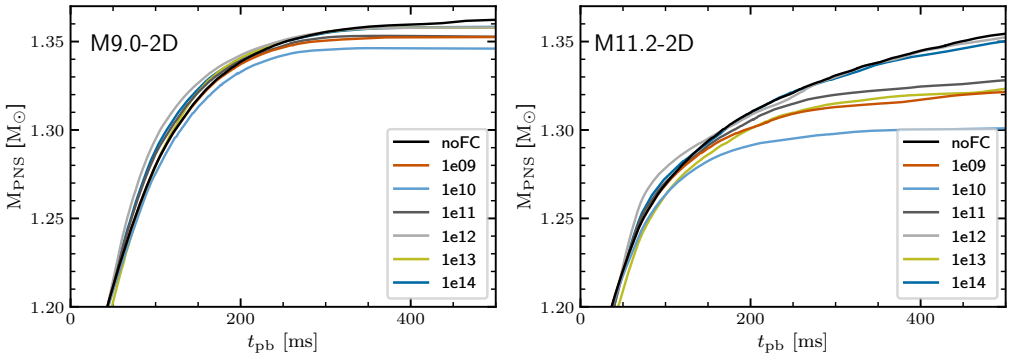

Figure 3.14 Mass of the PNS over time for the M9.0-2D series (left) and M11.2-2D (right) series.

the PNS radius approaches the extension of the other models. $Q_{\rm cool}$ increases, and the contraction of the shock radius proceeds faster than in the reference model. For model M9.0-2D-1e14 PNS convection is enhanced less strongly. This is because at the interface between no flavor conversion and flavor conversions the luminosities of ν_x are smaller. Therefore, less ν_x are converted to ν_e and $\bar{\nu}_e$ and the increase of the heating is reduced. Correspondingly, the shock radius evolves more like in model M9.0-2D-1e12. Still, after some time PNS contraction is stronger than in the reference model and the contraction of the PNS radius is decelerated at $t_{\rm pb} \gtrsim 150\,$ms.

Another aspect of increased PNS convection is its connection to the emission of gravitational waves (GWs). Until $t_{\rm pb} \approx 300\,$ms the lateral velocities in M9.0-2D-1e13 are larger than those in M9.0-2D-noFC by a factor of a few. PNS convection excites gravity waves in the layer between the convective zone and the surface of the PNS [164, 165]. Non-radial mass movements lead to the emission of GW in the frequency range of a few 100 Hz up to about 1000 Hz. A stronger PNS convection could lead to higher amplitudes in the GW signal. However, a thorough analysis of this is beyond the scope of this thesis.

As explosion sets in, the mass accretion to the PNS is throttled. Therefore, an early explosion correlates with a small $M_{\rm PNS}$ (Figure 3.14, left panel). Model M9.0-2D-1e10, exhibiting the earliest explosion, has a baryonic PNS mass of about $1.346\,M_\odot$ and models M9.0-2D-1e09 and M9.0-2D-1e11 have a baryonic mass of about $1.352\,M_\odot$. Models M9.0-2D1e12 – M9.0-2D1e14, in which explosion sets in roughly 100 ms later have a baryonic mass of about $1.36\,M_\odot$. Note that the mass is not final because the PNS further grows through accretion at later times. See also Table 3.2.

In this series of models, the luminosities of all flavors show a steady decline (Figure 3.12, left panel). This is because the accretion flow onto the PNS is small and neutrino emission is dominated by the cooling of the PNS. The decrease of the ν_e and $\bar{\nu}_e$ luminosity is similar to the decrease within the the M9.0-1D series. Characteristic spikes in the ν_e and $\bar{\nu}_e$ luminosity stemming from accretion events onto the PNS are also present in the ν_x luminosity, especially in those models where flavor conversion reach the PNS or are even present inside. The presence of flavor conversions is clearly visible in

the mean energies (right panels). Flavor conversions significantly reduce mean energies of ν_x and increase the mean energies of ν_e and $\bar{\nu}_e$. A rough correlation between high values of ρ_c and lower values of the mean energies for $\bar{\nu}_e$ and ν_x can be seen.

3.2.2 M11.2-2D

In the M11.2-2D series, the mass accretion rate drops more early and steeper than in the other series. The Si/Si-O interface passes the shock radius already about 60 ms after bounce. The subsequent expansion of the shock radius leads to a comparably large heating region in all models. In 4 out of 6 models with flavor conversions the explosion sets in more than 150 ms earlier than in the reference model without flavor conversions where the explosion is launched at about $t_{pb} = 400$ ms (Figure 3.15a).

In models M11.2-2D-1e09 and M11.2-2D-1e10, the explosion is aided by the increase of q_{gain} (Figure 3.15c). It is launched 150 ms and 140 ms after bounce, respectively (Figure 3.15a). Note that in model M11.2-2D-1e09 the heating rate only increase after the iso-density surface of $10^9\,\mathrm{g\,cm^{-3}}$ crosses the shock radius, which is at the time when the Si/Si-O interface passes. However, the density gradient in the progenitor model is so steep that the density quickly falls below $10^9\,\mathrm{g\,cm^{-3}}$ in a large volume of the post-shock region. The passing of the interface leads to a sudden expansion of the shock radius, which decreases Q_{cool}, slowing down the decrease of the mass in the gain layer caused by the contraction of the PNS. In all models with flavor conversion, the combination of this effect and the increased specific heating rate leads to a more extended shock expansion than in the reference model.

In model M11.2-2D-1e11, M_{gain} remains roughly constant for a period of more than 100 ms as the mean shock radius continuously increases. The explosion sets in at $t_{pb} \sim 200$ ms. For M11.2-2D-1e12, the mass in the gain layer is somewhat smaller. The decrease is sufficient to prevent an earlier explosion though the mean shock radius is transiently pushed out beyond 450 km. Instead, it takes another cycle of convective overturn for the model to explode at $t_{pn} = 400$ ms, similar to the reference model M11.2-2D-noFC.

At this point I would like to expand on the behavior of model M11.2-2D-1e13. The evolution of its shock radius does not seem to fit within the trend of the other models with the explosion setting in as exceptionally early, at the same time as in models M11.2-2D-1e10 and M11.2-2D-1e09. The reason for the early explosion is a coincidence of two effects. Like its counterpart in the M9.0-2D series (M9.0-2D-1e13) this model features an enhanced PNS convection and correspondingly larger r_{PNS} and M_{gain}. In model M11.2-2D-1e13 additionally, the mass accretion rate drops very early. This reduces the ram pressure of the infalling material, further stabilizing the gain layer. The combined effects lead to the early explosion. The coincidence is not present in M9.0-2D-1e13 where the mass accretion rate decreases continuously, which is why it is not exploding earlier than the reference model. Also in model M11.2-2D-1e14, both effects are present but not coincident. The PNS convection increasing effect develops later since the interface at $\rho = 10^{14}\,\mathrm{g\,cm^{-3}}$ is further inside and the luminosity of ν_x, whose conversion to ν_e and $\bar{\nu}_e$ is boosts the convection, are lower. The explosion sets in earlier than in the reference model but only about 100 ms. Therefore, the early explosion in M11.2-2D-1e13 should

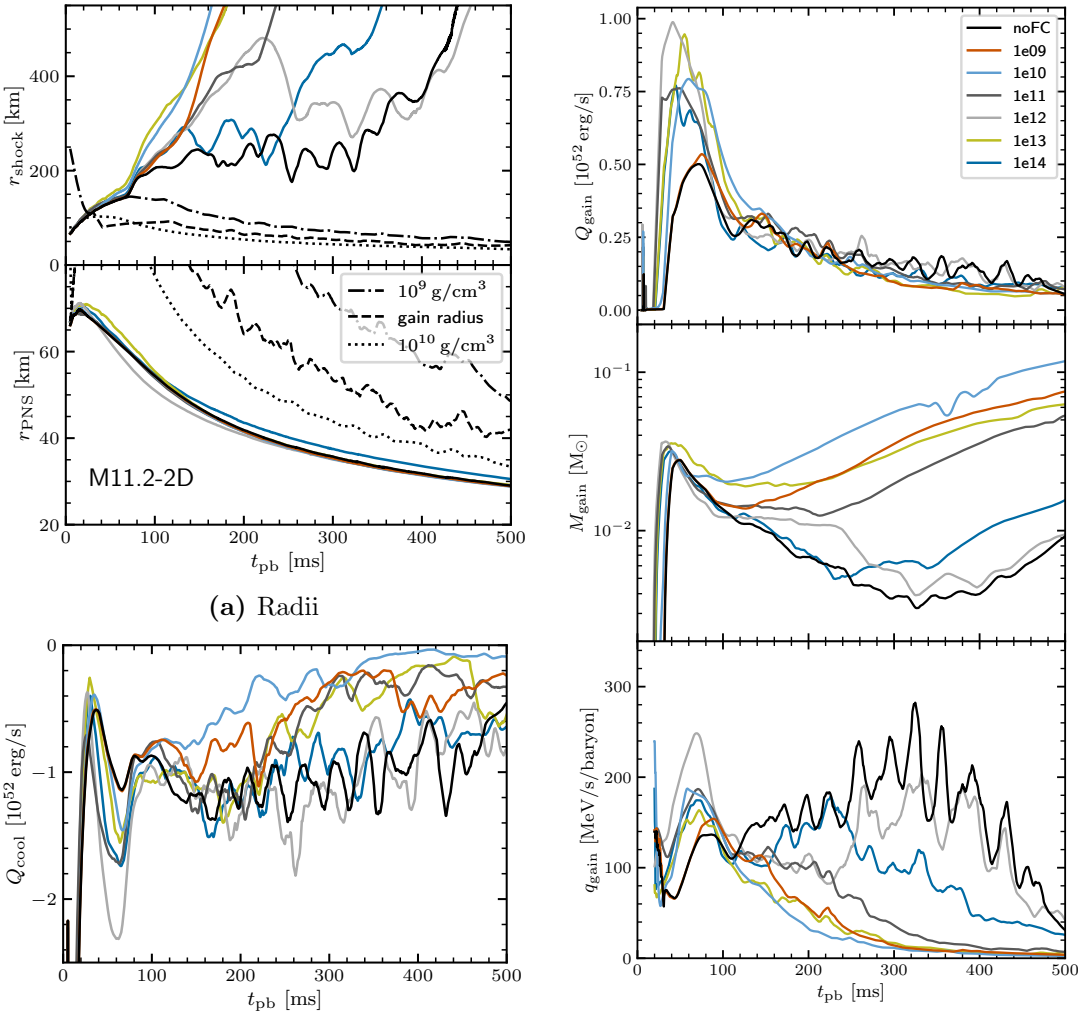

(a) Radii

(b) Cooling

(c) Heating

Figure 3.15 Dynamical properties of the M11.2-2D series. The color coding is according to the value of $\rho_{\rm c}$. (a): Early and strong shock expansion due to passing of the Si/Si-O interface (b): Total cooling in the cooling region ($Q_{\rm cool}$) (c): Heating properties in the gain region; models with flavor conversion tend to show higher specific heating rates ($q_{\rm gain}$) before explosion sets in; models with higher values of $\rho_{\rm c}$ correlate with smaller masses in the gain region, ($M_{\rm gain}$)

neither be considered as evidence for early explosions as a result of flavor conversions inside the PNS nor is robust prediction for the $11.2\,M_\odot$ progenitor. It is rather a result of the coincidence of enhanced PNS convection activity and an early drop in the reduced mass accretion rate.

Even more than in the M9.0-2D series the different times when explosion sets in leads to a diversity of the PNS masses. Note that in this series the masses still visibly increase at $t_{\rm pb} = 500\,{\rm ms}$ (Figure 3.14, right panel). M11.2-2D-1e10 has the lightest PNS with a mass of of $1.30\,M_\odot$. For M11.2-2D-1e09, M11.2-2D-1e11, and M11.2-2D-1e13 $M_{\rm PNS}$ exceed $1.32\,M_\odot$. For M11.2-2D-1e12, M11.2-2D-1e14 and M11.2-2D-noFC it exceeds $1.35\,M_\odot$ and keeps increasing.

The luminosities of the models with flavor conversions are smaller but not much reduced compared to the reference model (Figure 3.16), unlike in the M11.2-1D series. This is because with the small mass accretion rate the emission of neutrinos comes mostly from the cooling of the PNS—even more than in the M9.0-2D set. The difference to the M11.2-1D series is especially large for models M11.2-2D-1e13 and M11.2-2D-1e14 and connected to the increased PNS convection. The mean energies on the other hand are comparable to the respective models of the M11.2-1D series with ν_e and $\bar{\nu}_e$ mean energies being considerably higher than in the reference model and ν_x mean energies being reduced accordingly. At least for the mean energies of $\bar{\nu}_e$ and ν_x a rough ordering according to the value of $\rho_{\rm c}$ with high values of $\rho_{\rm c}$ correlating with lower mean energies can be seen.

3.2.3 M20.0-2D

In the M20.0-2D series, none of the models leads to an explosion (Figure 3.17a), in contrast to the M9.0-2D and M11.2-2D series, where all models eventually exhibit an explosion. Instead, this series of simulations agrees rather well with the results from the M20.0-1D series. Most strikingly, all models with flavor conversions tend to have reduced shock radii and there are no signs for any of them reaching conditions favorable for a revival of the shock expansion. However, there are a few differences to the behavior in 1D. Multi-dimensional flows through their stabilizing effects slow down the contraction of the shock radii. At a given time for a given value of $\rho_{\rm c}$, $r_{\rm shock}$ and $r_{\rm PNS}$ are larger than in the respective model of the 1D series. The specific heating rate in M20.0-2D-noFC (and also M20.0-2D-1e09) increases less than in the respective 1D models (Figure 3.8c and Figure 3.17c). This comes from the fact that the contraction of the ν_e and $\bar{\nu}_e$ neutrinospheres is slowed down and the mean energies of the neutrinos increase less strongly. As a result, the mean energy of ν_x remains higher than the mean energy of ν_e and $\bar{\nu}_e$ for a longer time. Therefore, flavor conversions keep increasing the mean energy of ν_e and $\bar{\nu}_e$, which increases the heating in flavor conversion models. In the respective 1D models, this effect reduces over time because models with flavor conversion contract faster. In the end, the 2D models with flavor conversion still show a tendency to be less likely to explode. However, compared to the 1D models this tendency is weaker.

For model M20.0-2D-1e09, some parts of the gain region overlap with the region where flavor conversions occur. But the overlap is too small to have a relevant dynamical effect

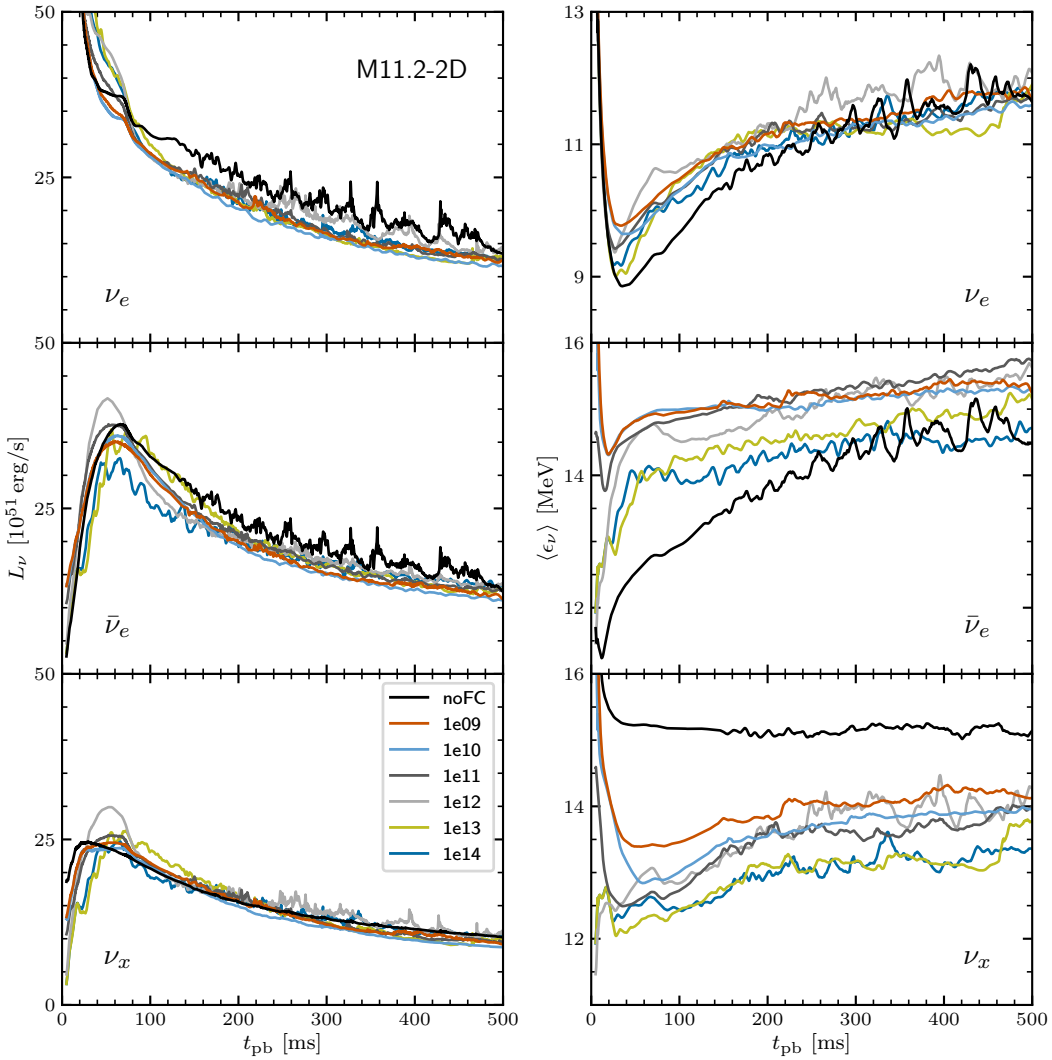

Figure 3.16 Neutrino properties for the simulations of the M11.2-2D series. Short-time fluctuations of the mean energy are reduced by smoothing the curves with a running average of 5 ms. All quantities are measured at a distance of 500 km and in the reference frame of a distant observer.

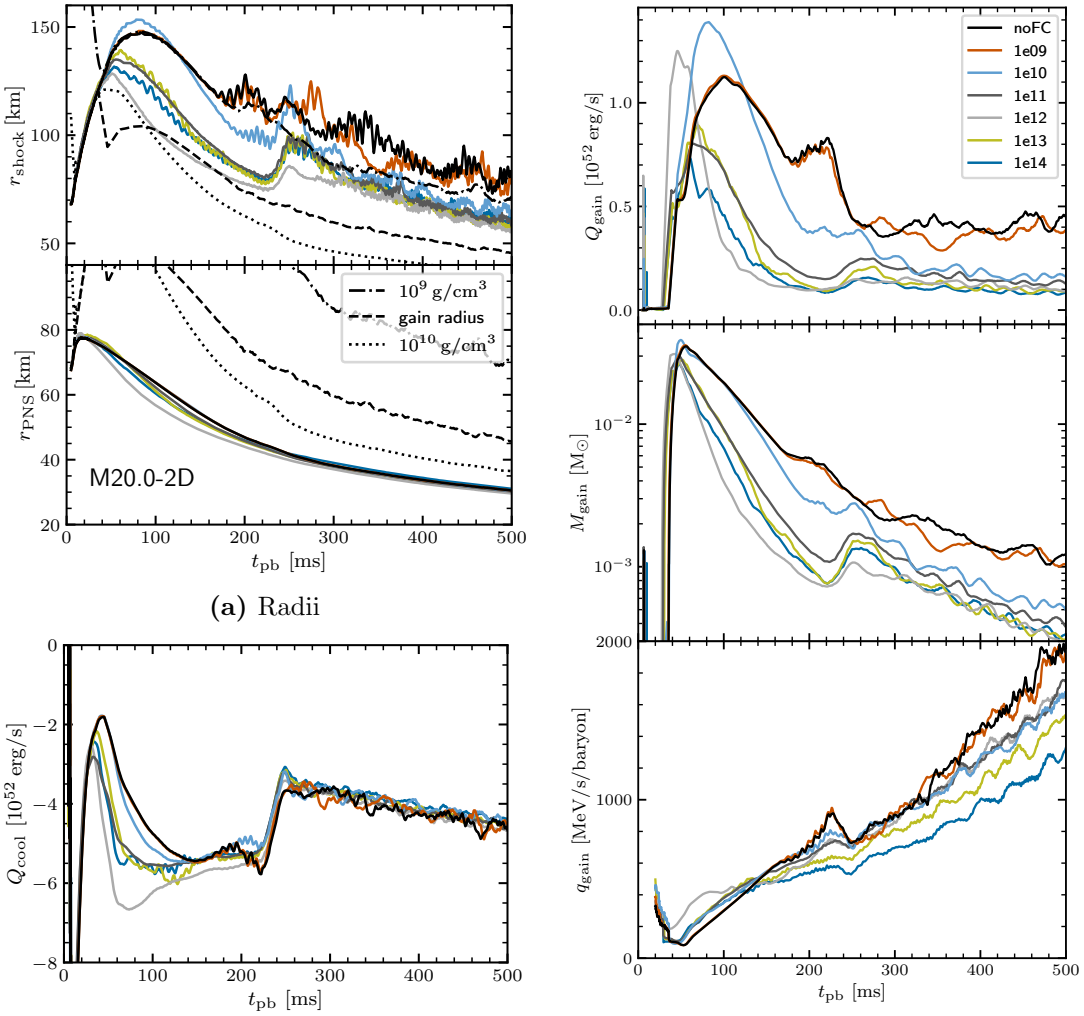

(a) Radii

(b) Cooling

(c) Heating

Figure 3.17 Dynamical properties of the M20.0-2D series. The color coding is according to the value of $\rho_{\rm c}$. (a): Weak shock expansion due to high accretion flow and strong contraction of thePNS. (b): Total cooling in the cooling region ($Q_{\rm cool}$). (c): Heating properties in the gain region; models with flavor conversion show higher specific heating rates ($q_{\rm gain}$) only in the first $\sim$ 150 ms after bounce; models with higher values of $\rho_{\rm c}$ have significantly smaller masses in the gain region ($M_{\rm gain}$) and therefore smaller total heating rates ($Q_{\rm gain}$).

and the shock radius behaves effectively as in the reference model. In model M20.0-2D-1e10, the shock transiently pushes further out than the shock in the reference model. But flavor conversions soon become active in the cooling region and the cooling enhancing effect dominates, just like in its 1D counterpart.

In models M20.0-2D-1e11 and M20.0-2D-1e12, the cooling enhancing effects dominate from the beginning on and M_{gain} is reduced with the meanwhile familiar impact on the shock expansion. Model M20.0-2D-1e12 has the lowest values for the shock expansion in this series.

As in the other 2D series, models M20.0-2D-1e13 and M20.0-2D-1e14 have an enhanced PNS convection that attenuates the earlier contraction of the PNS and therefore the contraction of the shock radius. The latter evolves as the shock radius of model M20.0-2D-1e11.

In this series of simulations, the PNS masses naturally keep increasing. The evolution is very similar for all models and at $t_{\mathrm{pb}} = 500,\mathrm{ms}$ they have reached a baryonic mass of about $1.91\,\mathrm{M}_\odot$ increasing at a speed of about $0.035\,\mathrm{M}_\odot\,s^{-1}$.

There is a clear difference between the neutrino luminosities of the models involving flavor conversion and the luminosities in the reference model. The ν_e and $\bar{\nu}_e$ luminosities are persistently lower and the ν_x luminosities are persistently higher in the simulations with flavor conversions (Figure 3.18). In fact, they are similar to the ones found in the M20.0-1D series because in both series none of the models shows a successful explosion. However, the mean energies of ν_e and $\bar{\nu}_e$ are reduced because stabilizing effects of non-radial flows slow down the contraction of the neutrinospheres, which remain at larger radii where the temperatures are smaller. For this reason, the range of higher energies over which $\nu_x, \nu_x \rightarrow \nu_e, \bar{\nu}_e$ conversions take remains larger for a longer period of times. For models with flavor conversions, the mean energies of ν_x remain smaller than in the reference model.

3.2.4 Delayed Onset of Flavor Conversions

The studies in this thesis are motivated but not strictly limited to FFC. In fact, FFC should obey the constraints used to construct the flavor conversion scheme used in this thesis (that is the conservation of the total neutrino number and the individual lepton numbers). However, FFC are proven to be triggered by crossings in the angular distribution of the ELN[4][85]. Studies explicitly searching for ELN crossings in simulations that do not take into account flavor conversions [95] find that it takes some time to develop ELN crossings since they occur not before around 100 ms after bounce. In models M9.0-2D-1e10 and M11.2-2D-1e10, the seeds to an early explosion have been already laid at this time.

Therefore, I repeated the simulations of M9.0-2D-1e09–M9.0-2D-1e11 and M11.2-2D-1e09–M11.2-2D-1e11 but turned on the flavor conversion scheme only after $t_{\mathrm{pb}} = 100\,\mathrm{ms}$. I will refer to these models with the same labels as the respective original simulations but add "-100ms".

[4] Or the respective equivalent if $n_{\nu_\mu} \neq n_{\bar{\nu}_\mu}$ or $n_{\nu_\tau} \neq n_{\bar{\nu}_\tau}$ [83]

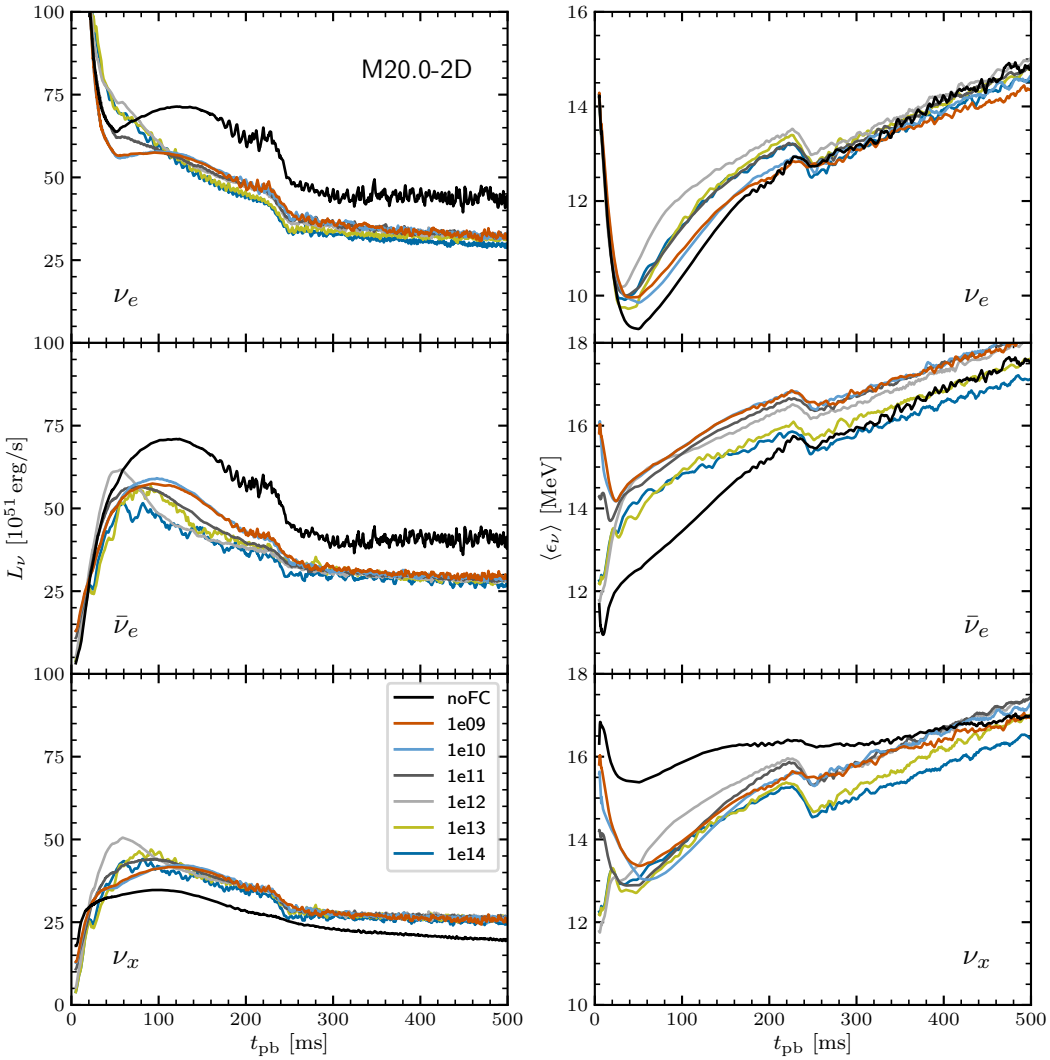

Figure 3.18 Neutrino properties for the simulations of the M20.0-2D series. Short-time fluctuations of the mean energy are reduced by smoothing the curves with a running average of 5 ms. All quantities are measured at a distance of 500 km and in the reference frame of a distant observer.

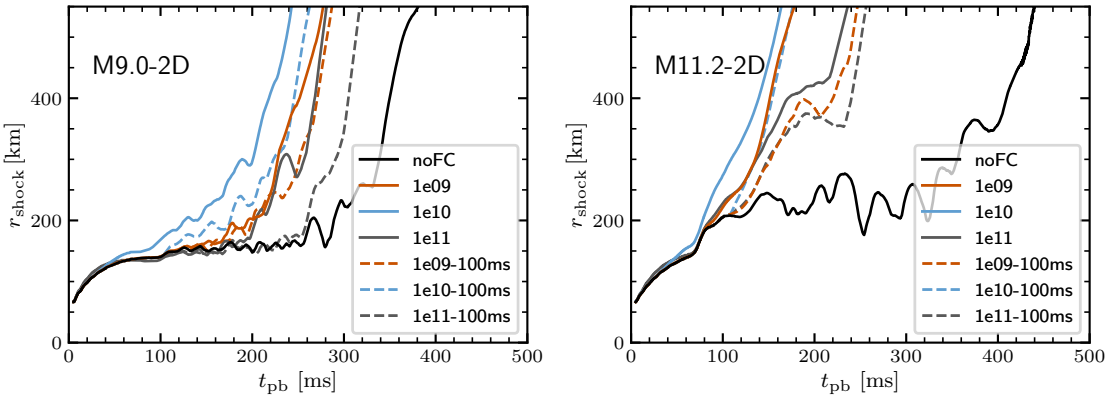

Figure 3.19 Shock radii of models with flavor conversion from the beginning (solid) and starting at $t_{\rm pb} = 100\,{\rm ms}$ (dashed) as functions of post-bounce time for the simulations of the M9.0-2D series (left) and M11.2-2D series (right).

The delayed onset does not cause any qualitative differences. Still, all models with flavor conversions show an earlier onset of the explosion than the respective reference models without flavor conversions(Figure 3.19). Compared to the respective model with flavor conversions from the beginning on, the explosion is delayed by about 20 ms. For models M9.0-2D-1e11-100ms, M11.2-2D-1e09-100ms, and M11.2-2D-1e11-100ms the explosion sets in with a larger delay due to an additional convective turn over, which could be a stochastic effect. The onset of the explosion is not delayed by more than 100 ms, compared to the respective simulations with immediate flavor conversions.

4 Summary of the Key Findings

In the course of this thesis I have performed 1D and 2D simulations initialized with three progenitor systems of different masses. The baryonic density is used as a criterion for the occurrence of flavor conversions and each simulation takes a different values of the critical density ρ_c as a fixed parameter. The naming scheme of the studied models encodes these parameters, e.g. M9.0-1D-1e09 refers to a progenitor of mass $9.0\,M_\odot$ simulated in 1D with $\rho_c = 10^9\,\mathrm{g\,cm^{-3}}$. Models with the suffix -noFC refer to reference simulations without flavor conversion. In regions where the density is below ρ_c, flavor conversions occur. This enables me to link their presence in different regions to (not necessarily local) effects on the explosion dynamics. The detailed impact on the supernova dynamics and the PNS structure can involve fairly complex feedback effects, depending on the phase of the evolution and the region where flavor conversions occur (heating layer, cooling layer, or inside the PNS). They reveal that the effects of flavor mixing are multi-layered and can affect the dynamics in different directions. The following sections summarize the non-trivial impact of neutrino flavor conversions on the explosion dynamics of CCSNe.

4.1 Flavor Conversions Outside of the Shocked Region

In the pre-shock region neutrino interactions are not frequent enough to have a relevant heating or cooling effect on the stellar matter. Therefore, flavor conversions upstream of the shock have almost no influence on the dynamical evolution of the system, but they would still change the observable neutrino signal.

4.2 Flavor Conversions in the Heating Region

Within the post-shock region and in the outer layers of the PNS $\nu_e, \bar{\nu}_e \rightarrow \nu_x, \nu_x$ conversions amplify neutrino cooling while $\nu_x, \nu_x \rightarrow \nu_e, \bar{\nu}_e$ conversions amplify neutrino heating processes. This is because ν_e and $\bar{\nu}_e$ couple more strongly to the stellar medium than ν_x, so the appearance of ν_e and $\bar{\nu}_e$ (at the cost of ν_x) increases the neutrino absorption rates whereas the appearance of ν_x (at the cost of ν_e and $\bar{\nu}_e$) decreases it. Both processes can happen at the same time ($\nu_e, \bar{\nu}_e \rightarrow \nu_x, \nu_x$ at lower; $\nu_x, \nu_x \rightarrow \nu_e, \bar{\nu}_e$ at higher energies). The energy-integrated heating or cooling rate is affected differently at varying locations depending on the energy at which conversions switch from $\nu_e, \bar{\nu}_e \rightarrow \nu_x, \nu_x$ to $\nu_x, \nu_x \rightarrow \nu_e, \bar{\nu}_e$ [1] and the local shapes of the neutrino spectra of the (unmixed) flavors.

In all simulations with flavor conversions in the heating region, the integrated specific heating rate, q_{gain}, increases, and in multi-dimensional simulations convection sets in

[1] That is the energy defining the spectral region in which ν_x are not the least abundant species anymore.

earlier. Both effects are beneficial for a successful explosion. Despite the limitations of spherical symmetry, models M11.2-1D-1e09 – M11.2-1D-1e11 feature an enhanced period of shock expansion and come close to a successful explosion [2]. Those 2D simulations in which flavor conversions are restricted to the heating region exhibit earlier explosions (models M9.0-2D-1e09, M9.0-2D-1e10, M11.2-2D-1e09, and M11.2-2D-1e10). For model M20.0-2D-1e09 flavor conversions do not cover a relevant portion of the heating region and for model M20.0-2D-1e10 flavor conversions occur in the cooling region too early so that the enhancement of the cooling prevents the development of conditions favorable for explosion. Therefore, flavor conversions do not increase the "explodability" in these models.

4.3 Flavor Conversions in the Cooling Region

In the cooling region, flavor conversions increase the cooling of matter by neutrinos. This is because there is a radial dependence of the consequences of flavor conversions on the local heating rate. At smaller radii a larger portion of the spectrum is subject to $\nu_e, \bar{\nu}_e \rightarrow \nu_x, \nu_x$ conversions. Hence, at a certain radius, flavor conversions cease to increase the local specific heating rate and instead decrease it. This turning point roughly coincides with the position of the gain radius. As a result, flavor conversions in the cooling region lead to higher cooling rates. Though q_{gain} remains higher, a stronger cooling further downstream amplifies the contraction of the PNS which increases the downward flow of mass out of the gain layer. This reduces the mass in the gain layer, M_{gain}, and therefore indirectly decreases the total heating in the gain region, Q_{gain}. Still, models M9.0-2D-1e11 and M11.2-2D-1e11 show an earlier onset of explosion compared to the reference model without flavor conversions. In the respective models with $\rho_{\mathrm{c}} = 10^{12}\,\mathrm{g\,cm^{-3}}$, where flavor conversions in the outer mantle of the PNS also lead to an even faster contraction, the explosion sets in at the same time as in the reference models.

4.4 Flavor Conversions Inside the PNS — Models with $\rho_{\mathrm{c}} = 10^{13}\,\mathrm{g\,cm^{-3}}$

In certain regions of the PNS, flavor conversions play an unexpected, special role. At densities above some $10^{12}\,\mathrm{g\,cm^{-3}}$ flavor conversions of type $\nu_x, \nu_x \rightarrow \nu_e, \bar{\nu}_e$ take place at all energies due to the low abundance of $\bar{\nu}_e$. As a consequence, in models M9.0-2D-1e13, M11.2-2D-1e13, and M20.0-2D-1e13, the local heating rate at the interface between the region with and without flavor conversions increases due to ν_e and $\bar{\nu}_e$ absorption. In 1D simulations, flavor conversions decelerate the energy release from the PNS core. In 2D simulations, the opposite effect is present. The absorption leads to a sudden heating that enhances the convection inside the PNS. Also, convection starts earlier. This stabilizes the PNS against contraction and increases energy transport from the inner parts of the PNS to the outer. Combined with the right timing of the accretion of a composition

[2] Though, in the end, also these models do not lead to a successful explosion in 1D.

shell interface of the collapsing progenitor star, this can lead to an exceptionally early explosion (as in model M11.2-2D-1e13).

5 Conclusions and Outlook

In the past years, neutrino flavor conversions have appeared as a challenge to numerical simulations of core-collapse supernovae (CCSNe). They arise as a consequence of the quantum mechanical nature of neutrinos and are a collective phenomenon due to neutrino self-interaction. A comprehensive understanding of the neutrino evolution requires the solution of the quantum-kinetic equation (QKE), which numerically remains impossible in the near future given the large separation of scales. Resolving fast flavor conversions (FFC), at the moment regarded as the dominating type of flavor conversions in the dynamically relevant regions, requires a resolution at the scale of a few cm while typical simulations cannot go beyond a resolution of a few 10 m without becoming unreasonably computationally expensive.

The work presented in this thesis, for the first time, includes neutrino flavor conversions in multi-dimensional, neutrino-radiation hydrodynamics simulations of CCSNe. I included a parameterized version of maximum flavor conversion that is compatible with conservation laws that are given by the nature of being an effect of coherent forward scattering. This allows me to infer a maximum effect that flavor conversions can have on the evolution of a CCSN. Using a density criterion to restrict flavor conversions to certain regions, I can attribute arising effects to the occurrence in these regions. This study defogs landmarks on the map of flavor conversions in CCSNe instead of charting precise paths based on simulations that are deemed to be unreliable at this stage.

I assume a maximum flavor equipartition that is compatible with conserving energy, momentum, and individual lepton numbers, to shed light on the maximum effect that flavor conversions can have on the dynamics of a CCSN. Because this does not rely on a specific scenario for flavor conversions it allows an analysis of the effects while being agnostic about the details of their origin.

Focusing on the immediate dynamical impact, the results suggest that flavor conversions can both facilitate or weaken the onset of runaway shock expansion, depending on the core structure of the stellar progenitor and the region where flavor conversions are assumed to occur. In the post-shock region they lead to stronger neutrino heating and enhance convection, which is beneficial for explosion. Conversions in regions where neutrinos have a cooling effect accelerate the contraction of the proto-neutron star (PNS). But deep inside this, they once more stir convection, which slows down the contraction. Flavor conversions modify the neutrino spectra reducing the ν_e and $\bar{\nu}_e$ luminosities while increasing their mean energies.

In a number of investigated models flavor conversions lead to earlier explosions. In any specific model, the time for the onset of the explosion directly correlates with the mass of the nascent neutron star. Hence, earlier explosions due to flavor conversions can lower the minimum neutron star mass expected from stellar collapse and could explain the

formation of neutron stars below $1.2\,M_\odot$, whose observations challenge current CCSN models [32, 166, 167]. For example, model M11.2-2D-1e10 (an axially symmetric (2D) simulation initialized with the $11.2\,M_\odot$ progenitor model and flavor conversions only occurring in the gain region) produces a neutron star with a baryonic mass of only $1.30\,M_\odot$ (gravitational mass of about $1.19\,M_\odot$ with a 12 km radius; [168]) instead of about $\gtrsim 1.36\,M_\odot$ found in the model without flavor conversions.

In all simulations with initialized with the $20.0\,M_\odot$ progenitor, flavor conversions hinder the explosion as a consequence of their occurrence in the cooling region. If flavor conversions systematically reduce the tendency of massive progenitors to explode, this will increase the black hole formation rate. If further simulations support this finding it might help to explain a discrepancy between the observation of the progenitor systems of type-II supernovae and the results of state-of-the-art numerical simulations. With such observations one can estimate the zero-age-main-sequence mass of stars. A systematic survey could not find progenitor systems whose zero-age-main-sequence exceeds 17–$20\,M_\odot$ [169]. Since current multidimensional models yield explosions well beyond this mass range [21, 170] it has been termed the red supergiant problem. A systematic reduction of the tendency to explode in such models would be intriguing evidence for flavor conversions.

In models where flavor conversions are present in the convectively unstable region in the PNS they lead to an earlier onset of convection. Furthermore, the lateral velocities in the models with flavor conversion are larger than in the respective reference model by a factor of a few. PNS convection causes a high frequency GW signal in the range of a few 100 Hz up to about 1000 Hz [164]. Larger velocities of the matter increase the amplitude of the gravitational waves (GWs) and could lead to a distinctive imprint in the signal. Though it is known that in 2D simulations the amplitude of GWs is overestimated, due to artificially coherent motion in axial symmetry, a comparison between the models with and without flavor conversions yields relative effects which can be transferable to a scenario without artificial symmetries. Detailed calculations are required to make substantial predictions but are beyond the scope of this thesis.

5.1 Observable Neutrino Signal

Of course, flavor conversions also affect the properties of the neutrino emission itself. This is true even if the flavor conversions do not leave an imprint on the dynamics, that is, if flavor conversions take place only in the pre-shock region. Naturally, the mixing prescription leads to an equalization of the spectra of the different flavors. $\nu_e, \bar{\nu}_e \rightarrow \nu_x, \nu_x$ conversions in the bulk of the energy spectra around the spectral peaks increase the ν_x luminosity at the cost of the ν_e and $\bar{\nu}_e$ luminosities. At the same time, $\nu_x, \nu_x \rightarrow \nu_e, \bar{\nu}_e$ conversions of high-energy ν_x in the spectral tail harden the ν_e and $\bar{\nu}_e$ spectra while the ν_x mean energy decreases. The equalization can be quite strong. In the reference models, there is a characteristic step-like decline of the luminosities and mean energies for ν_e and $\bar{\nu}_e$ at the time when the Si/Si-O composition interface of the progenitor falls through the shock. In the M20.0-1D and M20.0-2D series, this can also be seen for ν_x.

If confirmed, this feature and the rise of the high-energy tail of ν_e and $\bar{\nu}_e$ are signatures of neutrino flavor conversions to be probed in the observation of the next galactic CCSN. For the exact shape of the signal, the effect of matter resonances and other phenomena of flavor conversion like matter oscillations on the way to detectors on earth still need to be taken into account.

5.2 Flavor Conversions in a Broader Context

The effect of flavor conversions on the neutrino-driven mechanism of CCSNe is comparable to other supportive influences that are a topic of current research. For example the multidimensional nature of stars at the onset of collapse (in particular density and velocity inhomogeneities associated with convective oxygen and silicon shell burning) is important for the successful shock revival in fully multidimensional simulations [36, 37]. Considering the accuracy of the treatment of microphysical effects, such as the presence of muons in the high-density medium [24, 37], strangeness-dependent contributions to the axial-vector coupling constant of neutral current neutrino-nucleon scattering [39, 171], or higher effective nucleon mass at densities above roughly 10 % of the nuclear saturation density [172, 173] have a beneficial impact on the explosions. Also, magnetic fields can aid the initiation of the shock expansion even without the field-amplifying effects of rapid rotation, provided the pre-collapse core of the progenitor star is strongly magnetized [43, 174–176].

Non-standard physics such as a hadron-quark phase transition [177], beyond-standard-model particle physics [178, 179], and modified theories of gravity [180] have been suggested as potentially supportive to shock revival. In contrast to such possibilities, which reach beyond the limits of currently well constrained physics, flavor conversions are a phenomenon that occurs within the framework of well established theory, and its consequences for CCSNe should therefore be better understood.

Unlike most of the effects mentioned above, the impact of flavor conversions on the CCSN dynamics differs in low-mass ($9.0\,\mathrm{M}_\odot$ and $11.2\,\mathrm{M}_\odot$) and high-mass ($20.0\,\mathrm{M}_\odot$) progenitors. In the simulations initialized with one of the former progenitors, flavor conversions lead to earlier explosions, whereas in the simulations initialized with the latter progenitor, the collapse to a black hole seems to be even more favored. This is an intriguing result. It requires verification by more simulations initialized with different progenitor models. It is also interesting to see if this results still holds in simulations using a more elaborate treatment of the neutrino flavor evolution, replacing the simplifying assumptions chosen in the context of this thesis.

5.3 Outlook and Further Directions

Although this study was motivated by FFC, the revealed effects could be relevant also for flavor conversions in slow modes, provided that they occur close enough to the PNS and on scales shorter than the scale of the numerical resolution in this environment.

In this context, it is worth noting that the prescription of flavor equilibration is indeed expected to apply for slow modes [116, 181, 182].

This work does not explicitly account for specific effects of the recently unearthed phenomenon of collision induced flavor conversions [122–126]. It would require a more dedicated exploration of such a phenomenon, especially since collisional instabilities do not maintain the conservation of the electron lepton number (ELN). Should, however, collision induced conversions trigger FFC, the overall consequences might also be mimicked by the schematic treatment used in this thesis. Still, the inclusion of collision induced flavor conversions in dynamical CCSN simulations and their impact on the physics of these settings remain open questions at this moment. For a discussion of their impact on the supernova physics based on static backgrounds adopted from a CCSN simulation at different post-bounce times see [124].

Further work on practical solutions of the QKE in supernovae and neutron star mergers is also imperative [117, 121], including a better understanding of the final states after flavor conversions. But also a more realistic criterion for the onset of flavor conversions, based on angular crossings of the lepton number as required for instabilities in FFC, is needed. This would eliminate the need of a parameter to be sampled and open the possibility to advance to fully multi-dimensional simulations without any spacial symmetries (3D), which otherwise is unfeasible due to the high computational costs. Emerging machine-learning techniques [**Abbar2023˙3**, **Abbar2023˙4**, 103] might be particularly helpful for this, provided that they are reliable enough.

The first-of-a-kind simulations studied in this thesis open the door for further investigations of the consequences of flavor conversions in CCSN. The potential effect on higher amplitudes in the GW signals has already been mentioned. Simulations for a wider range of progenitors are needed to verify the bimodal outcome of flavor conversions to either support or hinder the neutrino-driven mechanism. Of particular interest are cases where flavor conversions make the difference between a successful or failed explosion. If flavor conversions lead to a systematic shift of the black hole formation rate they would also modify the predictions for the diffuse supernova neutrino background [183]. Furthermore, simulations with longer evolution times are needed to explore the consequences of flavor conversions on observable signals and CCSN properties. Explosion energies could be increased since an earlier onset of the explosion also means that more matter is ejected after being heated by neutrino radiation. Likewise this effects the nucleosynthesis in neutrino-heated ejecta that depends sensitively on the ratio of neutrons to protons. The absorption of ν_e and $\bar{\nu}_e$ in the neutrino heated ejecta modifies this ratio and because flavor conversions modify the electron type neutrino luminosities and spectra the generation of elements will be affected [19]. An extended set of models would provide the necessary input data to answer the question how flavor conversions change the nucleosynthetic yields of CCSN. Long-term simulations can also show to which degree flavor conversions influence neutrino signal in the cooling phase. The transport of energy via PNS convection is more efficient than from diffusion alone [184]. So again, special attention should be payed to models with flavor conversions reaching into the PNS core region.

Additional Information

Published Material

In the course of this PhD work, two peer-reviewed articles have been published:

- [136]: Jakob Ehring, Sajad Abbar, Hans-Thomas Janka, Georg Raffelt, and Irene Tamborra. "Fast neutrino flavor conversion in core-collapse supernovae: A parametric study in 1D models". In: *Phys. Rev. D* 107.10, 103034 (May 2023), p. 103034. DOI: 10.1103/PhysRevD.107.103034. arXiv: 2301.11938 [astro-ph.HE]
- [162]: Jakob Ehring, Sajad Abbar, Hans-Thomas Janka, Georg Raffelt, and Irene Tamborra. "Fast Neutrino Flavor Conversions Can Help and Hinder Neutrino-Driven Explosions". In: *Phys. Rev. Lett.* 131.6, 061401 (Aug. 2023), p. 061401. DOI: 10.1103/PhysRevLett.131.061401. arXiv: 2305.11207 [astro-ph.HE]

In both publications I am the lead author.

Funding

This work was supported by the German Research Foundation (DFG) through the Collaborative Research Centre "Neutrinos and Dark Matter in Astro- and Particle Physics (NDM)," Grant No. SFB-1258 – 283604770, and under Germany's Excellence Strategy through the Cluster of Excellence ORIGINS EXC-2094-390783311.

Computational Resources

The simulations discussed in this thesis were performed on the *Cobra* HPC system of the Max Planck Computing and Data Facility (MPCDF). The analysis of these simulations was done on the *lnx-23* machine of the Max-Planck-Institute for Astrophysics (MPA).

Software

This thesis would not have been possible without the following software:

- ALCAR [131]
- SNAPPY
- Numpy [185], Scipy [186]

Additional Information

- IPython [187]
- Matplotlib [188]

List of Abbreviations

1D one dimensional; simulations under the constraint of spherical symmetry

2D two dimensional; simulations under the constraint of axial symmetry

CCSN core-collapse supernova

ELN angular elctron lepton number

FFC fast flavor conversions

GW gravitational wave

NS neutron star

PNS proto-neutron star

QKE quantum-kinetic equation

List of Figures

List of Tables

Bibliography

[1] W. Baade and F. Zwicky. "On Super-novae". In: *Proceedings of the National Academy of Science* 20.5 (May 1934), pp. 254–259. DOI: 10.1073/pnas.20.5.254.

[2] W. Baade and F. Zwicky. "Cosmic Rays from Super-novae". In: *Proceedings of the National Academy of Science* 20.5 (May 1934), pp. 259–263. DOI: 10.1073/pnas.20.5.259.

[3] N. U. Mayall. "The Crab Nebula, a Probable Supernova". In: *Leaflet of the Astronomical Society of the Pacific* 3.119 (Jan. 1939), p. 145.

[4] David H. Staelin and III Reifenstein Edward C. "Pulsating Radio Sources near the Crab Nebula". In: *Science* 162.3861 (Dec. 1968), pp. 1481–1483. DOI: 10.1126/science.162.3861.1481.

[5] Stirling A. Colgate and Richard H. White. "The Hydrodynamic Behavior of Supernovae Explosions". In: *ApJ* 143 (Mar. 1966), p. 626. DOI: 10.1086/148549.

[6] H. A. Bethe and J. R. Wilson. "Revival of a stalled supernova shock by neutrino heating". In: *ApJ* 295 (Aug. 1985), pp. 14–23. DOI: 10.1086/163343.

[7] K. S. Hirata et al. "Observation in the Kamiokande-II detector of the neutrino burst from supernova SN1987A". In: *Phys. Rev. D* 38.2 (July 1988), pp. 448–458. DOI: 10.1103/PhysRevD.38.448.

[8] C. B. Bratton et al. "Angular distribution of events from SN1987A". In: *Phys. Rev. D* 37.12 (June 1988), pp. 3361–3363. DOI: 10.1103/PhysRevD.37.3361.

[9] E.N. Alexeyev et al. "Detection of the neutrino signal from SN 1987A in the LMC using the INR Baksan underground scintillation telescope". In: *Physics Letters B* 205.2 (1988), pp. 209–214. ISSN: 0370-2693. DOI: https://doi.org/10.1016/0370-2693(88)91651-6. URL: https://www.sciencedirect.com/science/article/pii/0370269388916516.

[10] H. A. Bethe. "Supernova mechanisms". In: *Reviews of Modern Physics* 62.4 (Oct. 1990), pp. 801–866. DOI: 10.1103/RevModPhys.62.801.

[11] H. -Th. Janka et al. "Theory of core-collapse supernovae". In: *Phys. Rep.* 442.1-6 (Apr. 2007), pp. 38–74. DOI: 10.1016/j.physrep.2007.02.002. arXiv: astro-ph/0612072 [astro-ph].

[12] Hans-Thomas Janka. "Explosion Mechanisms of Core-Collapse Supernovae". In: *Annual Review of Nuclear and Particle Science* 62.1 (Nov. 2012), pp. 407–451. DOI: 10.1146/annurev-nucl-102711-094901. arXiv: 1206.2503 [astro-ph.SR].

[13] Adam Burrows. "Colloquium: Perspectives on core-collapse supernova theory". In: *Reviews of Modern Physics* 85.1 (Jan. 2013), pp. 245–261. DOI: 10.1103/RevModPhys.85.245. arXiv: 1210.4921 [astro-ph.SR].

[14] Hans-Thomas Janka. "Neutrino-Driven Explosions". In: *Handbook of Supernovae*. Ed. by Athem W. Alsabti and Paul Murdin. 2017, p. 1095. DOI: 10.1007/978-3-319-21846-5_109.

[15] Hans-Thomas Janka. "Neutrino Emission from Supernovae". In: *Handbook of Supernovae*. Ed. by Athem W. Alsabti and Paul Murdin. 2017, p. 1575. DOI: 10.1007/978-3-319-21846-5_4.

[16] Thierry Foglizzo. "Explosion Physics of Core-Collapse Supernovae". In: *Handbook of Supernovae*. Ed. by Athem W. Alsabti and Paul Murdin. 2017, p. 1053. DOI: 10.1007/978-3-319-21846-5_52.

[17] Gabriel Martínez-Pinedo et al. "Neutrinos and Their Impact on Core-Collapse Supernova Nucleosynthesis". In: *Handbook of Supernovae*. Ed. by Athem W. Alsabti and Paul Murdin. 2017, p. 1805. DOI: 10.1007/978-3-319-21846-5_78.

[18] Anthony Mezzacappa et al. "Physical, numerical, and computational challenges of modeling neutrino transport in core-collapse supernovae". In: *Living Reviews in Computational Astrophysics* 6.1, 4 (Dec. 2020), p. 4. DOI: 10.1007/s41115-020-00010-8. arXiv: 2010.09013 [astro-ph.HE].

[19] Hans-Thomas Janka and Andreas Bauswein. "Dynamics and Equation of State Dependencies of Relevance for Nucleosynthesis in Supernovae and Neutron Star Mergers". In: *Handbook of Nuclear Physics*. Ed. by Isao Tanihata, Hiroshi Toki, and Toshitaka Kajino. Singapore: Springer Nature Singapore, 2020, pp. 1–98. ISBN: 978-981-15-8818-1. DOI: 10.1007/978-981-15-8818-1_93-1. URL: https://doi.org/10.1007/978-981-15-8818-1_93-1.

[20] Shinya Wanajo. "Nucleosynthesis in Neutrino-Heated Ejecta and Neutrino-Driven Winds of Core-Collapse Supernovae: Neutrino-Induced Nucleosynthesis". In: *Handbook of Nuclear Physics*. Ed. by Isao Tanihata, Hiroshi Toki, and Toshitaka Kajino. Singapore: Springer Nature Singapore, 2020, pp. 1–33. ISBN: 978-981-15-8818-1. DOI: 10.1007/978-981-15-8818-1_89-1. URL: https://doi.org/10.1007/978-981-15-8818-1_89-1.

[21] A. Burrows and D. Vartanyan. "Core-collapse supernova explosion theory". In: *Nature* 589.7840 (Jan. 2021), pp. 29–39. DOI: 10.1038/s41586-020-03059-w. arXiv: 2009.14157 [astro-ph.SR].

[22] J. M. LeBlanc and J. R. Wilson. "A Numerical Example of the Collapse of a Rotating Magnetized Star". In: *ApJ* 161 (Aug. 1970), p. 541. DOI: 10.1086/150558.

[23] E. Mueller and W. Hillebrandt. "A magnetohydrodynamical supernova model." In: *A&A* 80 (Dec. 1979), pp. 147–154.

[24] R. Bollig et al. "Muon Creation in Supernova Matter Facilitates Neutrino-Driven Explosions". In: *Phys. Rev. Lett.* 119.24, 242702 (Dec. 2017), p. 242702. DOI: 10.1103/PhysRevLett.119.242702. arXiv: 1706.04630 [astro-ph.HE].

[25] Robert Günther Bollig. "Muon Creation and Effects in Supernovae". Dissertation. München: Technische Universität München, Jan. 2018.

[26] Mathias Th. Keil, Georg G. Raffelt, and Hans-Thomas Janka. "Monte Carlo Study of Supernova Neutrino Spectra Formation". In: *ApJ* 590.2 (June 2003), pp. 971–991. DOI: 10.1086/375130. arXiv: astro-ph/0208035 [astro-ph].

[27] C. J. Horowitz. "Weak magnetism for antineutrinos in supernovae". In: *Phys. Rev. D* 65.4, 043001 (Feb. 2002), p. 043001. DOI: 10.1103/PhysRevD.65.043001. arXiv: astro-ph/0109209 [astro-ph].

[28] H. -Th. Janka. "Conditions for shock revival by neutrino heating in core-collapse supernovae". In: *A&A* 368 (Mar. 2001), pp. 527–560. DOI: 10.1051/0004-6361:20010012. arXiv: astro-ph/0008432 [astro-ph].

[29] C. J. Horowitz and Gang Li. "Nucleosynthesis in Supernovae". In: *Phys. Rev. Lett.* 82.26 (June 1999), pp. 5198–5201. DOI: 10.1103/PhysRevLett.82.5198. arXiv: astro-ph/9904171 [astro-ph].

[30] C. Fröhlich et al. "Neutrino-Induced Nucleosynthesis of A> 64 Nuclei: The νp Process". In: *Phys. Rev. Lett.* 96.14, 142502 (Apr. 2006), p. 142502. DOI: 10.1103/PhysRevLett.96.142502. arXiv: astro-ph/0511376 [astro-ph].

[31] J. Pruet et al. "Nucleosynthesis in Early Supernova Winds. II. The Role of Neutrinos". In: *ApJ* 644.2 (June 2006), pp. 1028–1039. DOI: 10.1086/503891. arXiv: astro-ph/0511194 [astro-ph].

[32] G. Stockinger et al. "Three-dimensional models of core-collapse supernovae from low-mass progenitors with implications for Crab". In: *MNRAS* 496.2 (Aug. 2020), pp. 2039–2084. DOI: 10.1093/mnras/staa1691. arXiv: 2005.02420 [astro-ph.HE].

[33] L. Hüdepohl et al. "Neutrino Signal of Electron-Capture Supernovae from Core Collapse to Cooling". In: *Phys. Rev. Lett.* 104.25, 251101 (June 2010), p. 251101. DOI: 10.1103/PhysRevLett.104.251101. arXiv: 0912.0260 [astro-ph.SR].

[34] Tuguldur Sukhbold et al. "Core-collapse Supernovae from 9 to 120 Solar Masses Based on Neutrino-powered Explosions". In: *ApJ* 821.1, 38 (Apr. 2016), p. 38. DOI: 10.3847/0004-637X/821/1/38. arXiv: 1510.04643 [astro-ph.HE].

[35] Luca Boccioli et al. "Explosion Mechanism of Core-collapse Supernovae: Role of the Si/Si-O Interface". In: *ApJ* 949.1, 17 (May 2023), p. 17. DOI: 10.3847/1538-4357/acc06a. arXiv: 2207.08361 [astro-ph.HE].

[36] Bernhard Müller et al. "Supernova simulations from a 3D progenitor model - Impact of perturbations and evolution of explosion properties". In: *MNRAS* 472.1 (Nov. 2017), pp. 491–513. DOI: 10.1093/mnras/stx1962. arXiv: 1705.00620 [astro-ph.SR].

[37] Robert Bollig et al. "Self-consistent 3D Supernova Models From -7 Minutes to +7 s: A 1-bethe Explosion of a 19 $M_\odot$ Progenitor". In: *ApJ* 915.1, 28 (July 2021), p. 28. DOI: 10.3847/1538-4357/abf82e. arXiv: 2010.10506 [astro-ph.HE].

[38] Florian Hanke et al. "SASI Activity in Three-dimensional Neutrino-hydrodynamics Simulations of Supernova Cores". In: *ApJ* 770.1, 66 (June 2013), p. 66. DOI: 10.1088/0004-637X/770/1/66. arXiv: 1303.6269 [astro-ph.SR].

[39] Tobias Melson et al. "Neutrino-driven Explosion of a 20 Solar-mass Star in Three Dimensions Enabled by Strange-quark Contributions to Neutrino-Nucleon Scattering". In: *ApJ* 808.2, L42 (Aug. 2015), p. L42. DOI: 10.1088/2041-8205/808/2/L42. arXiv: 1504.07631 [astro-ph.SR].

[40] Alexander Summa et al. "Rotation-supported Neutrino-driven Supernova Explosions in Three Dimensions and the Critical Luminosity Condition". In: *ApJ* 852.1, 28 (Jan. 2018), p. 28. DOI: 10.3847/1538-4357/aa9ce8. arXiv: 1708.04154 [astro-ph.HE].

[41] Robert Glas et al. "Three-dimensional Core-collapse Supernova Simulations with Multidimensional Neutrino Transport Compared to the Ray-by-ray-plus Approximation". In: *ApJ* 873.1, 45 (Mar. 2019), p. 45. DOI: 10.3847/1538-4357/ab0423. arXiv: 1809.10146 [astro-ph.HE].

[42] Adam Burrows et al. "The overarching framework of core-collapse supernova explosions as revealed by 3D FORNAX simulations". In: *MNRAS* 491.2 (Jan. 2020), pp. 2715–2735. DOI: 10.1093/mnras/stz3223. arXiv: 1909.04152 [astro-ph.HE].

[43] Bernhard Müller and Vishnu Varma. "A 3D simulation of a neutrino-driven supernova explosion aided by convection and magnetic fields". In: *MNRAS* 498.1 (Nov. 2020), pp. L109–L113. DOI: 10.1093/mnrasl/slaa137. arXiv: 2007.04775 [astro-ph.HE].

[44] Ko Nakamura, Tomoya Takiwaki, and Kei Kotake. "Three-dimensional simulation of a core-collapse supernova for a binary star progenitor of SN 1987A". In: *MNRAS* 514.3 (Aug. 2022), pp. 3941–3952. DOI: 10.1093/mnras/stac1586. arXiv: 2202.06295 [astro-ph.HE].

[45] John M. Blondin, Anthony Mezzacappa, and Christine DeMarino. "Stability of Standing Accretion Shocks, with an Eye toward Core-Collapse Supernovae". In: *ApJ* 584.2 (Feb. 2003), pp. 971–980. DOI: 10.1086/345812. arXiv: astro-ph/0210634 [astro-ph].

[46] T. Foglizzo et al. "Instability of a Stalled Accretion Shock: Evidence for the Advective-Acoustic Cycle". In: *ApJ* 654.2 (Jan. 2007), pp. 1006–1021. DOI: 10.1086/509612. arXiv: astro-ph/0606640 [astro-ph].

[47] Robert H. Kraichnan. "Inertial Ranges in Two-Dimensional Turbulence". In: *The Physics of Fluids* 10.7 (July 1967), pp. 1417–1423. ISSN: 0031-9171. DOI: 10.1063/1.1762301. eprint: https://pubs.aip.org/aip/pfl/article-pdf/10/7/1417/12451215/1417_1_online.pdf. URL: https://doi.org/10.1063/1.1762301.

[48] Florian Hanke et al. "Is Strong SASI Activity the Key to Successful Neutrino-driven Supernova Explosions?" In: *ApJ* 755.2, 138 (Aug. 2012), p. 138. DOI: 10.1088/0004-637X/755/2/138. arXiv: 1108.4355 [astro-ph.SR].

[49] H. Duan and J. P. Kneller. "TOPICAL REVIEW: Neutrino flavour transformation in supernovae". In: *Journal of Physics G Nuclear Physics* 36.11, 113201 (Nov. 2009), p. 113201. DOI: 10.1088/0954-3899/36/11/113201. arXiv: 0904.0974 [astro-ph.HE].

[50] Huaiyu Duan, George M. Fuller, and Yong-Zhong Qian. "Collective Neutrino Oscillations". In: *Annual Review of Nuclear and Particle Science* 60 (Nov. 2010), pp. 569–594. DOI: 10.1146/annurev.nucl.012809.104524. arXiv: 1001.2799 [hep-ph].

[51] A. Mirizzi et al. "Supernova neutrinos: production, oscillations and detection". In: *Nuovo Cimento Rivista Serie* 39.1-2 (Feb. 2016), pp. 1–112. DOI: 10.1393/ncr/i2016-10120-8. arXiv: 1508.00785 [astro-ph.HE].

[52] Shunsaku Horiuchi and James P. Kneller. "What can be learned from a future supernova neutrino detection?" In: *Journal of Physics G Nuclear Physics* 45.4 (Apr. 2018), p. 043002. DOI: 10.1088/1361-6471/aaa90a. arXiv: 1709.01515 [astro-ph.HE].

[53] Sherwood Richers and Manibrata Sen. "Fast Flavor Transformations". In: *Handbook of Nuclear Physics*. Ed. by Isao Tanihata, Hiroshi Toki, and Toshitaka Kajino. Singapore: Springer Nature Singapore, 2020, pp. 1–17. ISBN: 978-981-15-8818-1. DOI: 10.1007/978-981-15-8818-1_125-1. arXiv: 2207.03561. URL: https://doi.org/10.1007/978-981-15-8818-1_125-1.

[54] Irene Tamborra and Shashank Shalgar. "New Developments in Flavor Evolution of a Dense Neutrino Gas". In: *Annual Review of Nuclear and Particle Science* 71 (Sept. 2021), pp. 165–188. DOI: 10.1146/annurev-nucl-102920-050505. arXiv: 2011.01948 [astro-ph.HE].

[55] Francesco Capozzi and Ninetta Saviano. "Neutrino Flavor Conversions in High-Density Astrophysical and Cosmological Environments". In: *Universe* 8.2 (Feb. 2022), p. 94. DOI: 10.3390/universe8020094. arXiv: 2202.02494 [hep-ph].

[56] Maria Cristina Volpe. "Neutrinos from dense: flavor mechanisms, theoretical approaches, observations, new directions". In: *arXiv e-prints*, arXiv:2301.11814 (Jan. 2023), arXiv:2301.11814. DOI: 10.48550/arXiv.2301.11814. arXiv: 2301.11814 [hep-ph].

[57] Carlo Giunti and Chung W. Kim. *Fundamentals of Neutrino Physics and Astrophysics*. Oxford University Press, Mar. 2007. ISBN: 9780198508717. DOI: 10.1093/acprof:oso/9780198508717.001.0001. URL: https://doi.org/10.1093/acprof:oso/9780198508717.001.0001.

[58] L. Wolfenstein. "Neutrino oscillations in matter". In: *Phys. Rev. D* 17.9 (May 1978), pp. 2369–2374. DOI: 10.1103/PhysRevD.17.2369.

[59] S. P. Mikheyev and A. Yu. Smirnov. "Resonance enhancement of oscillations in matter and solar neutrino spectroscopy". In: *Yadernaya Fizika* 42 (Jan. 1985), pp. 1441–1448.

[60] Raymond Davis Jr., Don S. Harmer, and Kenneth C. Hoffman. "Search for neutrinos from the sun". In: *Phys. Rev. Lett.* 20 (1968), pp. 1205–1209. DOI: 10.1103/PhysRevLett.20.1205.

[61] John N. Bahcall, Neta A. Bahcall, and G. Shaviv. "Present status of the theoretical predictions for the Cl-36 solar neutrino experiment". In: *Phys. Rev. Lett.* 20 (1968), pp. 1209–1212. DOI: 10.1103/PhysRevLett.20.1209.

[62] Amol S. Dighe and Alexei Yu. Smirnov. "Identifying the neutrino mass spectrum from a supernova neutrino burst". In: *Phys. Rev. D* 62.3, 033007 (Aug. 2000), p. 033007. DOI: 10.1103/PhysRevD.62.033007. arXiv: hep-ph/9907423 [hep-ph].

[63] Jérôme Gava et al. "Dynamical Collective Calculation of Supernova Neutrino Signals". In: *Phys. Rev. Lett.* 103.7, 071101 (Aug. 2009), p. 071101. DOI: 10.1103/PhysRevLett.103.071101. arXiv: 0902.0317 [hep-ph].

[64] James Pantaleone. "Neutrino oscillations at high densities". In: *Physics Letters B* 287.1-3 (Aug. 1992), pp. 128–132. DOI: 10.1016/0370-2693(92)91887-F.

[65] G. Sigl and G. Raffelt. "General kinetic description of relativistic mixed neutrinos". In: *Nucl. Phys. B* 406 (1993), pp. 423–451. DOI: 10.1016/0550-3213(93)90175-O.

[66] R. F. Sawyer. "Multiangle instability in dense neutrino systems". In: *Phys. Rev. D* 79.10, 105003 (May 2009), p. 105003. DOI: 10.1103/PhysRevD.79.105003. arXiv: 0803.4319 [astro-ph].

[67] Basudeb Dasgupta et al. "Multiple Spectral Splits of Supernova Neutrinos". In: *Phys. Rev. Lett.* 103.5, 051105 (July 2009), p. 051105. DOI: 10.1103/PhysRevLett.103.051105. arXiv: 0904.3542 [hep-ph].

[68] Arka Banerjee, Amol Dighe, and Georg Raffelt. "Linearized flavor-stability analysis of dense neutrino streams". In: *Phys. Rev. D* 84.5, 053013 (Sept. 2011), p. 053013. DOI: 10.1103/PhysRevD.84.053013. arXiv: 1107.2308 [hep-ph].

[69] Sajad Abbar and Huaiyu Duan. "Fast neutrino flavor conversion: Roles of dense matter and spectrum crossing". In: *Phys. Rev. D* 98.4, 043014 (Aug. 2018), p. 043014. DOI: 10.1103/PhysRevD.98.043014. arXiv: 1712.07013 [hep-ph].

[70] Steen Hannestad et al. "Self-induced conversion in dense neutrino gases: Pendulum in flavor space". In: *Phys. Rev. D* 74.10, 105010 (Nov. 2006), p. 105010. DOI: 10.1103/PhysRevD.74.105010. arXiv: astro-ph/0608695 [astro-ph].

[71] Huaiyu Duan et al. "Simulation of coherent nonlinear neutrino flavor transformation in the supernova environment: Correlated neutrino trajectories". In: *Phys. Rev. D* 74.10, 105014 (Nov. 2006), p. 105014. DOI: 10.1103/PhysRevD.74.105014. arXiv: astro-ph/0606616 [astro-ph].

[72] Huaiyu Duan et al. "Coherent Development of Neutrino Flavor in the Supernova Environment". In: *Phys. Rev. Lett.* 97.24, 241101 (Dec. 2006), p. 241101. DOI: 10.1103/PhysRevLett.97.241101. arXiv: astro-ph/0608050 [astro-ph].

[73] Andreu Esteban-Pretel et al. "Mu-tau neutrino refraction and collective three-flavor transformations in supernovae". In: *Phys. Rev. D* 77.6, 065024 (Mar. 2008), p. 065024. DOI: 10.1103/PhysRevD.77.065024. arXiv: 0712.1137 [astro-ph].

[74] Srdjan Sarikas et al. "Suppression of Self-Induced Flavor Conversion in the Supernova Accretion Phase". In: *Phys. Rev. Lett.* 108.6, 061101 (Feb. 2012), p. 061101. DOI: 10.1103/PhysRevLett.108.061101. arXiv: 1109.3601 [astro-ph.SR].

[75] Huaiyu Duan and Alexander Friedland. "Self-Induced Suppression of Collective Neutrino Oscillations in a Supernova". In: *Phys. Rev. Lett.* 106.9, 091101 (Mar. 2011), p. 091101. DOI: 10.1103/PhysRevLett.106.091101. arXiv: 1006.2359 [hep-ph].

[76] Sovan Chakraborty et al. "Analysis of matter suppression in collective neutrino oscillations during the supernova accretion phase". In: *Phys. Rev. D* 84.2, 025002 (July 2011), p. 025002. DOI: 10.1103/PhysRevD.84.025002. arXiv: 1105.1130 [hep-ph].

[77] Sovan Chakraborty et al. "No Collective Neutrino Flavor Conversions during the Supernova Accretion Phase". In: *Phys. Rev. Lett.* 107.15, 151101 (Oct. 2011), p. 151101. DOI: 10.1103/PhysRevLett.107.151101. arXiv: 1104.4031 [hep-ph].

[78] Charles J. Stapleford, Carla Fröhlich, and James P. Kneller. "Coupling neutrino oscillations and simulations of core-collapse supernovae". In: *Phys. Rev. D* 102.8, 081301 (Oct. 2020), p. 081301. DOI: 10.1103/PhysRevD.102.081301. arXiv: 1910.04172 [astro-ph.HE].

[79] Sajad Abbar and Huaiyu Duan. "Neutrino flavor instabilities in a time-dependent supernova model". In: *Physics Letters B* 751 (Dec. 2015), pp. 43–47. DOI: 10.1016/j.physletb.2015.10.019. arXiv: 1509.01538 [astro-ph.HE].

[80] R. F. Sawyer. "Speed-up of neutrino transformations in a supernova environment". In: *Phys. Rev. D* 72.4, 045003 (Aug. 2005), p. 045003. DOI: 10.1103/PhysRevD.72.045003. arXiv: hep-ph/0503013 [astro-ph].

[81] R. F. Sawyer. "Neutrino Cloud Instabilities Just above the Neutrino Sphere of a Supernova". In: *Phys. Rev. Lett.* 116.8, 081101 (Feb. 2016), p. 081101. DOI: 10.1103/PhysRevLett.116.081101. arXiv: 1509.03323 [astro-ph.HE].

[82] Madhurima Chakraborty and Sovan Chakraborty. "Three flavor neutrino conversions in supernovae: slow & fast instabilities". In: *J. Cosmology Astropart. Phys.* 2020.1, 005 (Jan. 2020), p. 005. DOI: 10.1088/1475-7516/2020/01/005. arXiv: 1909.10420 [hep-ph].

[83] Francesco Capozzi et al. "Mu-Tau Neutrinos: Influencing Fast Flavor Conversions in Supernovae". In: *Phys. Rev. Lett.* 125.25, 251801 (Dec. 2020), p. 251801. DOI: 10.1103/PhysRevLett.125.251801. arXiv: 2005.14204 [hep-ph].

[84] Francesco Capozzi et al. "Fast neutrino flavor conversions in one-dimensional core-collapse supernova models with and without muon creation". In: *Phys. Rev. D* 103.6, 063013 (Mar. 2021), p. 063013. DOI: 10.1103/PhysRevD.103.063013. arXiv: 2012.08525 [astro-ph.HE].

[85] Taiki Morinaga. "Fast neutrino flavor instability and neutrino flavor lepton number crossings". In: *Phys. Rev. D* 105.10, L101301 (May 2022), p. L101301. DOI: 10.1103/PhysRevD.105.L101301. arXiv: 2103.15267 [hep-ph].

[86] Shashank Shalgar and Irene Tamborra. "Dispelling a myth on dense neutrino media: fast pairwise conversions depend on energy". In: *J. Cosmology Astropart. Phys.* 2021.1, 014 (Jan. 2021), p. 014. DOI: 10.1088/1475-7516/2021/01/014. arXiv: 2007.07926 [astro-ph.HE].

[87] Chinami Kato and Hiroki Nagakura. "Effects of energy-dependent scatterings on fast neutrino flavor conversions". In: *Phys. Rev. D* 106.12, 123013 (Dec. 2022), p. 123013. DOI: 10.1103/PhysRevD.106.123013. arXiv: 2207.09496 [astro-ph.HE].

[88] S. Chakraborty et al. "Self-induced flavor conversion of supernova neutrinos on small scales". In: *J. Cosmology Astropart. Phys.* 2016.1 (Jan. 2016), pp. 028–028. DOI: 10.1088/1475-7516/2016/01/028. arXiv: 1507.07569 [hep-ph].

[89] Ignacio Izaguirre, Georg Raffelt, and Irene Tamborra. "Fast Pairwise Conversion of Supernova Neutrinos: A Dispersion Relation Approach". In: *Phys. Rev. Lett.* 118.2, 021101 (Jan. 2017), p. 021101. DOI: 10.1103/PhysRevLett.118.021101. arXiv: 1610.01612 [hep-ph].

[90] Sajad Abbar. "Searching for fast neutrino flavor conversion modes in core-collapse supernova simulations". In: *J. Cosmology Astropart. Phys.* 2020.5, 027 (May 2020), p. 027. DOI: 10.1088/1475-7516/2020/05/027. arXiv: 2003.00969 [astro-ph.HE].

[91] Hiroki Nagakura. "Retrieval of energy spectra for all flavours of neutrinos from core-collapse supernova with multiple detectors". In: *MNRAS* 500.1 (Jan. 2021), pp. 319–332. DOI: 10.1093/mnras/staa3287. arXiv: 2008.10082 [astro-ph.HE].

[92] Hiroki Nagakura and Lucas Johns. "Constructing angular distributions of neutrinos in core-collapse supernovae from zeroth and first moments calibrated by full Boltzmann neutrino transport". In: *Phys. Rev. D* 103.12, 123025 (June 2021), p. 123025. DOI: 10.1103/PhysRevD.103.123025. arXiv: 2104.05729 [astro-ph.HE].

[93] Lucas Johns and Hiroki Nagakura. "Fast flavor instabilities and the search for neutrino angular crossings". In: *Phys. Rev. D* 103.12, 123012 (June 2021), p. 123012. DOI: 10.1103/PhysRevD.103.123012. arXiv: 2104.04106 [hep-ph].

[94] Sherwood Richers. "Evaluating approximate flavor instability metrics in neutron star mergers". In: *Phys. Rev. D* 106.8, 083005 (Oct. 2022), p. 083005. DOI: 10.1103/PhysRevD.106.083005. arXiv: 2206.08444 [astro-ph.HE].

[95] Hiroki Nagakura et al. "Where, when, and why: Occurrence of fast-pairwise collective neutrino oscillation in three-dimensional core-collapse supernova models". In: *Phys. Rev. D* 104.8, 083025 (Oct. 2021), p. 083025. DOI: 10.1103/PhysRevD.104.083025. arXiv: 2108.07281 [astro-ph.HE].

[96] Milad Delfan Azari et al. "Fast collective neutrino oscillations inside the neutrino sphere in core-collapse supernovae". In: *Phys. Rev. D* 101.2, 023018 (Jan. 2020), p. 023018. DOI: 10.1103/PhysRevD.101.023018. arXiv: 1910.06176 [astro-ph.HE].

[97] Sajad Abbar et al. "Fast neutrino flavor conversion modes in multidimensional core-collapse supernova models: The role of the asymmetric neutrino distributions". In: *Phys. Rev. D* 101.4, 043016 (Feb. 2020), p. 043016. DOI: 10.1103/PhysRevD.101.043016. arXiv: 1911.01983 [astro-ph.HE].

[98] Robert Glas et al. "Fast neutrino flavor instability in the neutron-star convection layer of three-dimensional supernova models". In: *Phys. Rev. D* 101.6, 063001 (Mar. 2020), p. 063001. DOI: 10.1103/PhysRevD.101.063001. arXiv: 1912.00274 [astro-ph.HE].

[99] Sajad Abbar et al. "On the occurrence of fast neutrino flavor conversions in multidimensional supernova models". In: *Phys. Rev. D* 100.4, 043004 (Aug. 2019), p. 043004. DOI: 10.1103/PhysRevD.100.043004. arXiv: 1812.06883 [astro-ph.HE].

[100] Sajad Abbar et al. "On the characteristics of fast neutrino flavor instabilities in three-dimensional core-collapse supernova models". In: *Phys. Rev. D* 103.6, 063033 (Mar. 2021), p. 063033. DOI: 10.1103/PhysRevD.103.063033. arXiv: 2012.06594 [astro-ph.HE].

[101] Hiroki Nagakura, Kohsuke Sumiyoshi, and Shoichi Yamada. "Possible Early Linear Acceleration of Proto-neutron Stars via Asymmetric Neutrino Emission in Core-collapse Supernovae". In: *ApJ* 880.2, L28 (Aug. 2019), p. L28. DOI: 10.3847/2041-8213/ab30ca. arXiv: 1907.04863 [astro-ph.HE].

[102] Taiki Morinaga et al. "Fast neutrino-flavor conversion in the preshock region of core-collapse supernovae". In: *Physical Review Research* 2.1, 012046 (Feb. 2020), p. 012046. DOI: 10.1103/PhysRevResearch.2.012046. arXiv: 1909.13131 [astro-ph.HE].

[103] Sajad Abbar. "Applications of machine learning to detecting fast neutrino flavor instabilities in core-collapse supernova and neutron star merger models". In: *Phys. Rev. D* 107.10, 103006 (May 2023), p. 103006. DOI: 10.1103/PhysRevD.107.103006. arXiv: 2303.05560 [astro-ph.HE].

[104] Meng-Ru Wu et al. "Collective fast neutrino flavor conversions in a 1D box: Initial conditions and long-term evolution". In: *Phys. Rev. D* 104.10, 103003 (Nov. 2021), p. 103003. DOI: 10.1103/PhysRevD.104.103003. arXiv: 2108.09886 [hep-ph].

[105] Sherwood Richers, Donald Willcox, and Nicole Ford. "Neutrino fast flavor instability in three dimensions". In: *Phys. Rev. D* 104.10, 103023 (Nov. 2021), p. 103023. DOI: 10.1103/PhysRevD.104.103023. arXiv: 2109.08631 [astro-ph.HE].

[106] Joshua D. Martin, Sajad Abbar, and Huaiyu Duan. "Nonlinear flavor development of a two-dimensional neutrino gas". In: *Phys. Rev. D* 100.2, 023016 (July 2019), p. 023016. DOI: 10.1103/PhysRevD.100.023016. arXiv: 1904.08877 [hep-ph].

[107] Joshua D. Martin, Changhao Yi, and Huaiyu Duan. "Dynamic fast flavor oscillation waves in dense neutrino gases". In: *Physics Letters B* 800, 135088 (Jan. 2020), p. 135088. DOI: 10.1016/j.physletb.2019.135088. arXiv: 1909.05225 [hep-ph].

[108] Soumya Bhattacharyya and Basudeb Dasgupta. "Late-time behavior of fast neutrino oscillations". In: *Phys. Rev. D* 102.6, 063018 (Sept. 2020), p. 063018. DOI: 10.1103/PhysRevD.102.063018.

[109] Sajad Abbar. "Turbulence fingerprint on collective oscillations of supernova neutrinos". In: *Phys. Rev. D* 103.4, 045014 (Feb. 2021), p. 045014. DOI: 10.1103/PhysRevD.103.045014. arXiv: 2007.13655 [astro-ph.HE].

[110] Sherwood Richers et al. "Code comparison for fast flavor instability simulations". In: *Phys. Rev. D* 106.4, 043011 (Aug. 2022), p. 043011. DOI: 10.1103/PhysRevD.106.043011. arXiv: 2205.06282 [astro-ph.HE].

[111] Zewei Xiong et al. "Evaluating approximate asymptotic distributions for fast neutrino flavor conversions in a periodic 1D box". In: *Phys. Rev. D* 108.6, 063003 (Sept. 2023), p. 063003. DOI: 10.1103/PhysRevD.108.063003. arXiv: 2307.11129 [astro-ph.HE].

[112] Francesco Capozzi et al. "Collisional Triggering of Fast Flavor Conversions of Supernova Neutrinos". In: *Phys. Rev. Lett.* 122.9, 091101 (Mar. 2019), p. 091101. DOI: 10.1103/PhysRevLett.122.091101. arXiv: 1808.06618 [hep-ph].

[113] Joshua D. Martin et al. "Fast flavor oscillations in dense neutrino media with collisions". In: *Phys. Rev. D* 103.6, 063001 (Mar. 2021), p. 063001. DOI: 10.1103/PhysRevD.103.063001. arXiv: 2101.01278 [hep-ph].

[114] Shashank Shalgar and Irene Tamborra. "Change of direction in pairwise neutrino conversion physics: The effect of collisions". In: *Phys. Rev. D* 103.6, 063002 (Mar. 2021), p. 063002. DOI: 10.1103/PhysRevD.103.063002. arXiv: 2011.00004 [astro-ph.HE].

[115] Chinami Kato, Hiroki Nagakura, and Masamichi Zaizen. "Flavor conversions with energy-dependent neutrino emission and absorption". In: *Phys. Rev. D* 108.2, 023006 (July 2023), p. 023006. DOI: 10.1103/PhysRevD.108.023006. arXiv: 2303.16453 [astro-ph.HE].

[116] Shashank Shalgar and Irene Tamborra. "Neutrino flavor conversion, advection, and collisions: Toward the full solution". In: *Phys. Rev. D* 107.6, 063025 (Mar. 2023), p. 063025. DOI: 10.1103/PhysRevD.107.063025. arXiv: 2207.04058 [astro-ph.HE].

[117] Shashank Shalgar and Irene Tamborra. "Do we have enough evidence to invalidate the mean-field approximation adopted to model collective neutrino oscillations?" In: *Phys. Rev. D* 107.12, 123004 (June 2023), p. 123004. DOI: 10.1103/PhysRevD.107.123004. arXiv: 2304.13050 [astro-ph.HE].

[118] Masamichi Zaizen and Hiroki Nagakura. "Simple method for determining asymptotic states of fast neutrino-flavor conversion". In: *Phys. Rev. D* 107.10, 103022 (May 2023), p. 103022. DOI: 10.1103/PhysRevD.107.103022. arXiv: 2211.09343 [astro-ph.HE].

[119] Masamichi Zaizen and Hiroki Nagakura. "Characterizing quasisteady states of fast neutrino-flavor conversion by stability and conservation laws". In: *Phys. Rev. D* 107.12, 123021 (June 2023), p. 123021. DOI: 10.1103/PhysRevD.107.123021. arXiv: 2304.05044 [astro-ph.HE].

[120] Hiroki Nagakura and Masamichi Zaizen. "Time-Dependent and Quasisteady Features of Fast Neutrino-Flavor Conversion". In: *Phys. Rev. Lett.* 129.26, 261101 (Dec. 2022), p. 261101. DOI: 10.1103/PhysRevLett.129.261101. arXiv: 2206.04097 [astro-ph.HE].

[121] Hiroki Nagakura. "Roles of Fast Neutrino-Flavor Conversion on the Neutrino-Heating Mechanism of Core-Collapse Supernova". In: *Phys. Rev. Lett.* 130.21, 211401 (May 2023), p. 211401. DOI: 10.1103/PhysRevLett.130.211401. arXiv: 2301.10785 [astro-ph.HE].

[122] Lucas Johns. "Collisional flavor instabilities of supernova neutrinos". In: *arXiv e-prints*, arXiv:2104.11369 (Apr. 2021), arXiv:2104.11369. DOI: 10.48550/arXiv.2104.11369. arXiv: 2104.11369 [hep-ph].

[123] Lucas Johns and Zewei Xiong. "Collisional instabilities of neutrinos and their interplay with fast flavor conversion in compact objects". In: *Phys. Rev. D* 106.10, 103029 (Nov. 2022), p. 103029. DOI: 10.1103/PhysRevD.106.103029. arXiv: 2208.11059 [hep-ph].

[124] Zewei Xiong et al. "Evolution of collisional neutrino flavor instabilities in spherically symmetric supernova models". In: *Phys. Rev. D* 107.8, 083016 (Apr. 2023), p. 083016. DOI: 10.1103/PhysRevD.107.083016. arXiv: 2210.08254 [astro-ph.HE].

[125] Zewei Xiong et al. "Collisional flavor instability in dense neutrino gases". In: *Phys. Rev. D* 108.8, 083002 (Oct. 2023), p. 083002. DOI: 10.1103/PhysRevD.108.083002. arXiv: 2212.03750 [hep-ph].

[126] Yu-Chia Lin and Huaiyu Duan. "Collision-induced flavor instability in dense neutrino gases with energy-dependent scattering". In: *Phys. Rev. D* 107.8, 083034 (Apr. 2023), p. 083034. DOI: 10.1103/PhysRevD.107.083034. arXiv: 2210.09218 [hep-ph].

[127] Chinami Kato, Hiroki Nagakura, and Lucas Johns. "Collisional flavor swap with neutrino self-interactions". In: *arXiv e-prints*, arXiv:2309.02619 (Sept. 2023), arXiv:2309.02619. DOI: 10.48550/arXiv.2309.02619. arXiv: 2309.02619 [astro-ph.HE].

[128] Lucas Johns and Hiroki Nagakura. "Self-consistency in models of neutrino scattering and fast flavor conversion". In: *Phys. Rev. D* 106.4, 043031 (Aug. 2022), p. 043031. DOI: 10.1103/PhysRevD.106.043031. arXiv: 2206.09225 [hep-ph].

[129] Oliver Just et al. "Fast neutrino conversion in hydrodynamic simulations of neutrino-cooled accretion disks". In: *Phys. Rev. D* 105.8, 083024 (Apr. 2022), p. 083024. DOI: 10.1103/PhysRevD.105.083024. arXiv: 2203.16559 [astro-ph.HE].

[130] Xinyu Li and Daniel M. Siegel. "Neutrino Fast Flavor Conversions in Neutron-Star Postmerger Accretion Disks". In: *Phys. Rev. Lett.* 126.25, 251101 (June 2021), p. 251101. DOI: 10.1103/PhysRevLett.126.251101. arXiv: 2103.02616 [astro-ph.HE].

[131] O. Just, M. Obergaulinger, and H. -T. Janka. "A new multidimensional, energy-dependent two-moment transport code for neutrino-hydrodynamics". In: *MNRAS* 453.4 (Nov. 2015), pp. 3386–3413. DOI: 10.1093/mnras/stv1892. arXiv: 1501.02999 [astro-ph.HE].

[132] Martin Obergaulinger. "Astrophysical magnetohydrodynamics and radiative transfer". Dissertation. München: Technische Universität München, Jan. 2008.

[133] Oliver Just. "Multidimensional, Two-Moment Multi-Group Neutrino Transport and its Application to Black-Hole Accretion Tori as Remnants of Neutron-Star Mergers". Dissertation. München: Technische Universität München, 2012.

[134] O. Just et al. "Core-collapse supernova simulations in one and two dimensions: comparison of codes and approximations". In: *MNRAS* 481.4 (Dec. 2018), pp. 4786–4814. DOI: 10.1093/mnras/sty2578. arXiv: 1805.03953 [astro-ph.HE].

[135] Robert Glas. "Applications of Different Neutrino-Transport Methods in Three-Dimensional Supernova Simulations". Dissertation. München: Technische Universität München, Jan. 2019.

[136] Jakob Ehring et al. "Fast neutrino flavor conversion in core-collapse supernovae: A parametric study in 1D models". In: *Phys. Rev. D* 107.10, 103034 (May 2023), p. 103034. DOI: 10.1103/PhysRevD.107.103034. arXiv: 2301.11938 [astro-ph.HE].

[137] A. W. Steiner, M. Hempel, and T. Fischer. "Core-collapse Supernova Equations of State Based on Neutron Star Observations". In: *ApJ* 774.1, 17 (Sept. 2013), p. 17. DOI: 10.1088/0004-637X/774/1/17. arXiv: 1207.2184 [astro-ph.SR].

[138] A. Marek et al. "Exploring the relativistic regime with Newtonian hydrodynamics: an improved effective gravitational potential for supernova simulations". In: *A&A* 445.1 (Jan. 2006), pp. 273–289. DOI: 10.1051/0004-6361:20052840. arXiv: astro-ph/0502161 [astro-ph].

[139] Alain Munier and Robert Weaver. "Radiation transfer in the fluid frame: A covariant formulation: Part I: Radiation hydrodynamics". In: *Computer Physics Reports* 3.3 (1986), pp. 127–164. ISSN: 0167-7977. DOI: https://doi.org/10.1016/0167-7977(86)90007-9. URL: https://www.sciencedirect.com/science/article/pii/0167797786900079.

[140] Alain Munier and Robert Weaver. "Radiation transfer in the fluid frame: A covariant formulation: Part II: The radiation transfer equation". In: *Computer Physics Reports* 3.3 (1986), pp. 165–208. ISSN: 0167-7977. DOI: https://doi.org/10.1016/0167-7977(86)90008-0. URL: https://www.sciencedirect.com/science/article/pii/0167797786900080.

[141] M. Rampp and H. -T. Janka. "Radiation hydrodynamics with neutrinos. Variable Eddington factor method for core-collapse supernova simulations". In: *A&A* 396 (Dec. 2002), pp. 361–392. DOI: 10.1051/0004-6361:20021398. arXiv: astro-ph/0203101 [astro-ph].

[142] S. Pennisi and M. Trovato. "On the irreducibility of professor G.F. Smith's representations for isotropic functions". In: *International Journal of Engineering Science* 25.8 (1987), pp. 1059–1065. ISSN: 0020-7225. DOI: https://doi.org/10.1016/0020-7225(87)90097-8. URL: https://www.sciencedirect.com/science/article/pii/0020722587900978.

[143] C. D. Levermore. "Relating Eddington factors to flux limiters." In: *J. Quant. Spec. Radiat. Transf.* 31.2 (Feb. 1984), pp. 149–160. DOI: 10.1016/0022-4073(84)90112-2.

[144] G. N. Minerbo. "Maximum entropy Eddington factors." In: *J. Quant. Spec. Radiat. Transf.* 20.6 (Jan. 1978), pp. 541–545. DOI: 10.1016/0022-4073(78)90024-9.

[145] S. W. Bruenn. "Stellar core collapse - Numerical model and infall epoch". In: *ApJS* 58 (Aug. 1985), pp. 771–841. DOI: 10.1086/191056.

[146] Anthony Mezzacappa and Stephen W. Bruenn. "Type II Supernovae and Boltzmann Neutrino Transport: The Infall Phase". In: *ApJ* 405 (Mar. 1993), p. 637. DOI: 10.1086/172394.

[147] W. R. Yueh and J. R. Buchler. "Neutrino transport in supernova models: S/N method." In: *ApJ* 217 (Oct. 1977), pp. 565–577. DOI: 10.1086/155605.

[148] J. Cernohorsky. "Symmetries in Neutrino-Electron Scattering". In: *ApJ* 433 (Sept. 1994), p. 247. DOI: 10.1086/174639.

[149] J. A. Pons, J. A. Miralles, and J. M. Ibáñez. "Legendre expansion of the $\nu\bar{\nu} \leftrightarrow e^+e^-$ kernel: Influence of high order terms". In: *Astron. Astrophys. Suppl.* 129 (Apr. 1998), pp. 343–351. DOI: 10.1051/aas:1998189. arXiv: astro-ph/9802333 [astro-ph].

[150] S. W. Bruenn and A. Mezzacappa. "Ion screening effects and stellar collapse". In: *Phys. Rev. D* 56 (12 Dec. 1997), pp. 7529–7547. DOI: 10.1103/PhysRevD.56.7529. URL: https://link.aps.org/doi/10.1103/PhysRevD.56.7529.

[151] C. J. Horowitz. "Neutrino trapping in a supernova and the screening of weak neutral currents". In: *Phys. Rev. D* 55.8 (Apr. 1997), pp. 4577–4581. DOI: 10.1103/PhysRevD.55.4577. arXiv: astro-ph/9603138 [astro-ph].

[152] Evan O'Connor. "An Open-source Neutrino Radiation Hydrodynamics Code for Core-collapse Supernovae". In: *ApJS* 219.2, 24 (Aug. 2015), p. 24. DOI: 10.1088/0067-0049/219/2/24. arXiv: 1411.7058 [astro-ph.HE].

[153] R. Courant, K. Friedrichs, and H. Lewy. "Über die partiellen Differenzengleichungen der mathematischen Physik". In: *Mathematische Annalen* 100 (Jan. 1928), pp. 32–74. DOI: 10.1007/BF01448839.

[154] David Radice et al. "Electron-capture and Low-mass Iron-core-collapse Supernovae: New Neutrino-radiation-hydrodynamics Simulations". In: *ApJ* 850.1, 43 (Nov. 2017), p. 43. DOI: 10.3847/1538-4357/aa92c5. arXiv: 1702.03927 [astro-ph.HE].

[155] S. E. Woosley, A. Heger, and T. A. Weaver. "The evolution and explosion of massive stars". In: *Reviews of Modern Physics* 74.4 (Nov. 2002), pp. 1015–1071. DOI: 10.1103/RevModPhys.74.1015.

[156] R. Buras et al. "Two-dimensional hydrodynamic core-collapse supernova simulations with spectral neutrino transport. I. Numerical method and results for a 15 M⊙ star". In: *A&A* 447.3 (Mar. 2006), pp. 1049–1092. DOI: 10.1051/0004-6361:20053783. arXiv: astro-ph/0507135 [astro-ph].

[157] A. Marek and H. -Th. Janka. "Delayed Neutrino-Driven Supernova Explosions Aided by the Standing Accretion-Shock Instability". In: *ApJ* 694.1 (Mar. 2009), pp. 664–696. DOI: 10.1088/0004-637X/694/1/664. arXiv: 0708.3372 [astro-ph].

[158] Tomoya Takiwaki, Kei Kotake, and Yudai Suwa. "Three-dimensional Hydrodynamic Core-collapse Supernova Simulations for an 11.2 $M_\odot$ Star with Spectral Neutrino Transport". In: *ApJ* 749.2, 98 (Apr. 2012), p. 98. DOI: 10.1088/0004-637X/749/2/98. arXiv: 1108.3989 [astro-ph.HE].

[159] B. Müller. "The dynamics of neutrino-driven supernova explosions after shock revival in 2D and 3D". In: *MNRAS* 453.1 (Oct. 2015), pp. 287–310. DOI: 10.1093/mnras/stv1611. arXiv: 1506.05139 [astro-ph.SR].

[160] S. E. Woosley and A. Heger. "Nucleosynthesis and remnants in massive stars of solar metallicity". In: *Phys. Rep.* 442.1-6 (Apr. 2007), pp. 269–283. DOI: 10.1016/j.physrep.2007.02.009. arXiv: astro-ph/0702176 [astro-ph].

[161] David Vartanyan et al. "Revival of the fittest: exploding core-collapse supernovae from 12 to 25 $M_\odot$". In: *MNRAS* 477.3 (July 2018), pp. 3091–3108. DOI: 10.1093/mnras/sty809. arXiv: 1801.08148 [astro-ph.HE].

[162] Jakob Ehring et al. "Fast Neutrino Flavor Conversions Can Help and Hinder Neutrino-Driven Explosions". In: *Phys. Rev. Lett.* 131.6, 061401 (Aug. 2023), p. 061401. DOI: 10.1103/PhysRevLett.131.061401. arXiv: 2305.11207 [astro-ph.HE].

[163] Wolfgang Keil, H. -Thomas Janka, and Ewald Mueller. "Ledoux Convection in Protoneutron Stars—A Clue to Supernova Nucleosynthesis?" In: *ApJ* 473 (Dec. 1996), p. L111. DOI: 10.1086/310404. arXiv: astro-ph/9610203 [astro-ph].

[164] Kei Kotake and Takami Kuroda. "Gravitational Waves from Core-Collapse Supernovae". In: *Handbook of Supernovae*. Ed. by Athem W. Alsabti and Paul Murdin. 2017, p. 1671. DOI: 10.1007/978-3-319-21846-5_9.

[165] A. Marek, H. -T. Janka, and E. Müller. "Equation-of-state dependent features in shock-oscillation modulated neutrino and gravitational-wave signals from supernovae". In: *A&A* 496.2 (Mar. 2009), pp. 475–494. DOI: 10.1051/0004-6361/200810883. arXiv: 0808.4136 [astro-ph].

[166] Yudai Suwa et al. "On the minimum mass of neutron stars". In: *MNRAS* 481.3 (Dec. 2018), pp. 3305–3312. DOI: 10.1093/mnras/sty2460. arXiv: 1808.02328 [astro-ph.HE].

[167] J. G. Martinez et al. "Pulsar J0453+1559: A Double Neutron Star System with a Large Mass Asymmetry". In: *ApJ* 812.2, 143 (Oct. 2015), p. 143. DOI: 10.1088/0004-637X/812/2/143. arXiv: 1509.08805 [astro-ph.HE].

[168] J. M. Lattimer and M. Prakash. "Neutron Star Structure and the Equation of State". In: *ApJ* 550.1 (Mar. 2001), pp. 426–442. DOI: 10.1086/319702. arXiv: astro-ph/0002232 [astro-ph].

[169] S. J. Smartt et al. "The death of massive stars - I. Observational constraints on the progenitors of Type II-P supernovae". In: *MNRAS* 395.3 (May 2009), pp. 1409–1437. DOI: 10.1111/j.1365-2966.2009.14506.x. arXiv: 0809.0403 [astro-ph].

[170] Ko Nakamura et al. "Systematic features of axisymmetric neutrino-driven core-collapse supernova models in multiple progenitors". In: *PASJ* 67.6, 107 (Dec. 2015), p. 107. DOI: 10.1093/pasj/psv073. arXiv: 1406.2415 [astro-ph.HE].

[171] C. J. Horowitz et al. "Neutrino-nucleon scattering in supernova matter from the virial expansion". In: *Phys. Rev. C* 95.2, 025801 (Feb. 2017), p. 025801. DOI: 10.1103/PhysRevC.95.025801. arXiv: 1611.05140 [nucl-th].

[172] A. S. Schneider et al. "Equation of state effects in the core collapse of a 20 -$M_\odot$ star". In: *Phys. Rev. C* 100.5, 055802 (Nov. 2019), p. 055802. DOI: 10.1103/PhysRevC.100.055802. arXiv: 1906.02009 [astro-ph.HE].

[173] H. Yasin et al. "Equation of State Effects in Core-Collapse Supernovae". In: *Phys. Rev. Lett.* 124.9, 092701 (Mar. 2020), p. 092701. DOI: 10.1103/PhysRevLett.124.092701. arXiv: 1812.02002 [nucl-th].

[174] M. Obergaulinger, H. -Th. Janka, and M. A. Aloy. "Magnetic field amplification and magnetically supported explosions of collapsing, non-rotating stellar cores". In: *MNRAS* 445.3 (Dec. 2014), pp. 3169–3199. DOI: 10.1093/mnras/stu1969. arXiv: 1405.7466 [astro-ph.SR].

[175] J. Matsumoto et al. "Magnetic support for neutrino-driven explosion of 3D non-rotating core-collapse supernova models". In: *MNRAS* 516.2 (Oct. 2022), pp. 1752–1767. DOI: 10.1093/mnras/stac2335. arXiv: 2202.07967 [astro-ph.HE].

[176] Vishnu Varma, Bernhard Müller, and Fabian R. N. Schneider. "3D simulations of strongly magnetized non-rotating supernovae: explosion dynamics and remnant properties". In: *MNRAS* 518.3 (Jan. 2023), pp. 3622–3636. DOI: 10.1093/mnras/stac3247. arXiv: 2204.11009 [astro-ph.HE].

[177] Tobias Fischer et al. "Quark deconfinement as a supernova explosion engine for massive blue supergiant stars". In: *Nature Astronomy* 2 (Oct. 2018), pp. 980–986. DOI: 10.1038/s41550-018-0583-0. arXiv: 1712.08788 [astro-ph.HE].

[178] T. Rembiasz et al. "Heavy sterile neutrinos in stellar core-collapse". In: *Phys. Rev. D* 98.10, 103010 (Nov. 2018), p. 103010. DOI: 10.1103/PhysRevD.98.103010. arXiv: 1806.03300 [astro-ph.HE].

[179] Kanji Mori et al. "Shock revival in core-collapse supernovae assisted by heavy axionlike particles". In: *Phys. Rev. D* 105.6, 063009 (Mar. 2022), p. 063009. DOI: 10.1103/PhysRevD.105.063009. arXiv: 2112.03613 [astro-ph.HE].

[180] Takami Kuroda and Masaru Shibata. "Spontaneous scalarization as a new core-collapse supernova mechanism and its multimessenger signals". In: *Phys. Rev. D* 107.10, 103025 (May 2023), p. 103025. DOI: 10.1103/PhysRevD.107.103025. arXiv: 2302.09853 [astro-ph.HE].

[181] Andreu Esteban-Pretel et al. "Decoherence in supernova neutrino transformations suppressed by deleptonization". In: *Phys. Rev. D* 76.12, 125018 (Dec. 2007), p. 125018. DOI: 10.1103/PhysRevD.76.125018. arXiv: 0706.2498 [astro-ph].

[182] Shashank Shalgar and Irene Tamborra. "Neutrino decoupling is altered by flavor conversion". In: *Phys. Rev. D* 108.4, 043006 (Aug. 2023), p. 043006. DOI: 10.1103/PhysRevD.108.043006. arXiv: 2206.00676 [astro-ph.HE].

[183] Daniel Kresse, Thomas Ertl, and Hans-Thomas Janka. "Stellar Collapse Diversity and the Diffuse Supernova Neutrino Background". In: *ApJ* 909.2, 169 (Mar. 2021), p. 169. DOI: 10.3847/1538-4357/abd54e. arXiv: 2010.04728 [astro-ph.HE].

[184] Damiano F. G. Fiorillo et al. "Supernova simulations confront SN 1987A neutrinos". In: *Phys. Rev. D* 108.8, 083040 (Oct. 2023), p. 083040. DOI: 10.1103/PhysRevD.108.083040. arXiv: 2308.01403 [astro-ph.HE].

[185] Charles R. Harris et al. "Array programming with NumPy". In: *Nature* 585.7825 (Sept. 2020), pp. 357–362. DOI: 10.1038/s41586-020-2649-2. URL: https://doi.org/10.1038/s41586-020-2649-2.

[186] Pauli Virtanen et al. "SciPy 1.0: Fundamental Algorithms for Scientific Computing in Python". In: *Nature Methods* 17 (2020), pp. 261–272. DOI: 10.1038/s41592-019-0686-2.

[187] Fernando Pérez and Brian E. Granger. "IPython: a System for Interactive Scientific Computing". In: *Computing in Science and Engineering* 9.3 (May 2007), pp. 21–29. ISSN: 1521-9615. DOI: 10.1109/MCSE.2007.53. URL: https://ipython.org.

[188] J. D. Hunter. "Matplotlib: A 2D graphics environment". In: *Computing in Science & Engineering* 9.3 (2007), pp. 90–95. DOI: 10.1109/MCSE.2007.55.

Acknowledgments

An dieser Stelle möchte ich mich bei einigen Personen bedanken ohne die ich diese Arbeit nicht hätte anfertigen können.

Allen voran danke ich meinen Betreuern *Hans-Thomas Janka* und *Georg Raffelt*. Durch euch hatte ich die Möglichkeit an diesem Thema zu forschen und meinen Fußabdruck in der Wissenschaft zu hinterlassen. Danke für die anregenden Diskussionen, dass ihr euer Wissen zu Supernovae und Neutrinos an mich weitergegeben habt und für euer Verständnis, wenn manche Sachen länger gebraucht haben, als ursprünglich geplant.

I thank *Sajad Abbar* for his supervision and help especially when interpreting the results of my work, for his patience elucidating me with the mysteries of flavor conversions, and for his contribution to writing the papers that have emerged from of this thesis.

Ich bin *Robert Glas* zu Dank verpflichtet dafür, dass er bei allen technischen Fragen eine so verlässliche Quelle für Antworten war; insbesondere für seine Unterweisung im Gebrauch von ALCAR und SNAPPY.

I thank all other members of the working groups at MPA and MPP. You made the institutes a place I really enjoyed working at. Also, when it came to discussions and activities not related to work I always felt welcome and valued.

I thank the developers of ALCAR and SNAPPY for providing me with the instruments that I needed to do this research.

I thank *Jakob Hein*, *Robert Glas*, *Sajad Abbar*, *Lea Heckmann*, and *Austin Moore*, the proof readers of this thesis.

I thank my (long-term) office mates *Thomas Ertl*, *Christian Partmann*, and *Sajad Abbar* who dwelt with me behind desks for so many days.

I would also like to thank all other PhD students and post-docs at MPA and MPP.

Ich danke dem nichtwissenschaftlichen Personal der Institute (einschließlich den Mitarbeitenden des MPCDF und der Tagunsstätte Schloss Ringberg) dafür, dass sie ein so gutes Umfeld geschaffen haben. Hervorheben möchte ich *Andi Weiß*, der nicht nur in der IT eine Lösung für (fast) alle Probleme hat, sondern mich auch stets dabei unterstützt hat, wenn ich (leider viel zu selten) meinen Arbeitsweg auf 2 Rädern zurücklegte.

Den richtigen Ausgleich für eine Arbeit am Schreibtisch habe ich unterwasser gefunden. Ich danke allen Unterwasserhockeys, die meine Leidenschaft teilen und mit mir am Beckenboden um den Puck kämpfen. Insbesondere *Christoph Mair* habe ich viel zu verdanken. Darüber hinaus natürlich noch den Nationalmannschaften der WM von 2023. Es war unvergesslich mit euch nach Australien fahren zu dürfen!

Ich danke meiner Familie, die einen unermesslichen Anteil daran hat, dass ich nie aufgehört habe Fragen zu stellen und mich entscheiden konnte den wissenschaftlichen Weg einzuschlagen.

Bei *Christina Bischofberger*. Für deine Liebe in den letzten 13 Jahren.